Bioinspired Nanocomposites for Structural Energy Storage

by

Ahmet Emrehan Emre

A dissertation submitted in partial fulfillment
of the requirements for the degree of
Doctor of Philosophy
(Biomedical Engineering)
in the University of Michigan
2021

Doctoral Committee:

Professor Nicholas Kotov, Chair
Associate Professor James Moon
Associate Professor Jeff Sakamoto
Associate Professor Ariella Shikanov

Ahmet E. Emre

emrehan@umich.edu

ORCID iD: 0000-0002-0126-1494

Dedication

I would like to dedicate this dissertation to my lovely kids who brighten my day.

Acknowledgements

"The nature of reality is this: It is hidden, it is hidden, and it is hidden" Rumi. This is an aphorism engraved on an egg-shaped statue in front of our research complex (NCRC) that I passed by every day during my doctoral studies. I am grateful to complete a significant milestone during my re-search for the hidden with the intelligent, creative, and caring people at the University of Michigan, Ann Arbor.

This thesis would not have been possible without the encouragement, help, and guidance from many individuals. I want to express my deepest appreciation to each and every one of them.

First, I would like to sincerely thank my advisor, Professor Nicholas Kotov, for his endless support and guidance. I admire him as a great scientist, caring family member, and role model. I would like to express my gratitude for the opportunity to pursue my Ph.D. in his prestigious laboratory.

I would like to thank all my committee members. I am grateful to Professor Shikanov and Professor Moon, for sharing their valuable time to discuss my research and provide constructive feedback. I am grateful to Professor Sakamoto and his lab members for helping me at the UM Energy Institute laboratories.

I would like to thank all current and past members of the Kotov Lab for many good memories. Specifically, I would like to thank Dr. Siu on Tung and Dr. Jinchen Fan for their help on electrochemistry and battery research. I would like to thank Dr. Ji-Young Kim, Dr. Naomi Ramesar, Dr. Priyan Weerappuli, and Dr. Yichun Wang for their friendship and collaboration.

I would also like to thank Mr. Bobby Kerns, Dr. Haiping Sun, Dr. Nancy Muyanja, Dr. Kai Sun, Dr. Allen Hunter, Dr. Tao Ma from the Michigan Center for Materials Characterization, Dr. Zhongrui (Jerry) Li from Central Campus EMAL, and Dr. Damon Hoff from the SMART center for their tremendous help on material characterization, visualization, and other measurements. I want to thank Dr. Nadine Wong and Mr. Karl Olsen from the Biointerfaces Institute and Ms. Mary Beth Westin of the Chemical Engineering Department for their kindness and efforts to keep our research running smoothly and safely.

I want to thank all the funding agencies for their support during our research at the University of Michigan. I specifically want to thank the Turkish Government and the Turkish Ministry of Education for the generous graduate research scholarship. I am profoundly grateful.

Last but not least, I would like to thank my family for their unconditional love and support during my graduate studies. I especially want to thank my best friend, my wife, Sumeyra Emre, and my kids, Talha and Taha, for making my life meaningful and joyful. I am lucky to have them.

I have met so many people from various disciplines, backgrounds, countries over the last couple of years. I believe that I learned something from each of them. I want to thank them all for helping me grow, broadening my vision, and ultimately helping me become an insightful researcher.

Thank you, and Go Blue!

Preface

This thesis summarizes research work I have conducted during my doctoral studies and contains the following published article and manuscripts in preparation:

Chapter 2 is reproduced with minor modifications from Wang, M., Emre, A., Tung, S., Gerber, A., Huang, Y., Cecen, V., Kotov, N.A. Biomimetic Solid-State Zn2+ Electrolyte for Corrugated Structural Batteries. *ACS Nano* **13**, 1107–1115 (2019).

Chapter 3 is reproduced with minor modifications from the manuscript that is submitted and under review: Emre, A. †, Wang, M. †, Kim, J.Y., Liu L., Cecen, V., Huang, Y., Kotov, N.A. (†Equally contributed), Multifactorial Engineering of Biomimetic Membranes for Batteries with Multiple High-Performance Parameters, (2021).

Chapter 4 is reproduced with minor modifications from the manuscript that is in the final stages for submission: Emre, A., Turali Emre, E.S., Kim, J.Y., Gerber, A., Cecen, V., Kotov, N.A., Bioinspired Quasi-Solid Electrolyte with Tunable Porosity.

Table of Contents

List of Tables

List of Figures

List of Equations

List of Abbreviations

A	Electrode Area (cm2)
ACN	Acetonitrile
ALPS	Aramid Lithium PVA Separator
ANF	Aramid Nanofiber
CV	Cyclic Voltammetry
DI Water	De-Ionized Water
DME	1,2-Dimethoxyethane
DMSO	Dimethyl Sulfoxide
DOD	U.S. Department of Defense
DOL	1,3-Dioxolane
DSC	Differential Scanning Calorimetry
EIS	Electrochemical Impedance Spectroscopy
EV	Electric Vehicle
F	Faraday's Constant
FTIR	Fourier Transformed Infrared Spectroscopy
GBM	Glomerular Basement Membrane
GT	Graph Theory
ICM	Ion Conducting Membrane
KOH	Potassium Hydroxide

LBL	Layer-by-layer
LIB	Lithium-Ion Battery
LiPF6	Lithium Hexafluorophosphate
LiTFSI	Lithium bis(trifluoromethanesulfonyl)imide
LiNO3	Lithium nitrate
MIP	Mercury Intrusion Porosimetry
NMC	Nickel-Manganese-Cobalt-Oxide
NMP	N-Methyl-2-pyrrolidone
PDDA	Polydiallyldimethylammonium Chloride
PEO	Polyethylene Oxide
PP	Polypropylene
PVA	Polytetrafluoroethylene
PVdF	Polyvinylidene Fluoride
SEM	Scanning Electron Microscopy
SSE	Solid State Electrolyte
TFSI	Bis(trifluoromethane)sulfonimide
TEM	Transmission Electron Microscopy
TGA	Thermal Gravimetric Analysis
VAF	Vacuum-Assisted Filtration
XRD	X-Ray Diffraction
ZnTf	Zinc trifluoromethanesulfonate
Ω	Resistance

Abstract

Energy storage is an integral part of life. Living creatures have developed a distributed and structural energy storage system to survive under various and sometimes extreme conditions. Similarly, energy storage is critical for today's modern life to power from small biomedical instruments to large aircraft. There are still several challenges against efficient and safe energy storage utilization due to the mechanical, chemical, and physical limitations of existing materials. Inspired by biological structures, we present multifunctional nanocomposites from aramid nanofibers (ANF), a Kevlar's nanoscale version, to address the safety and efficiency of various battery chemistries and enable structural energy storage to increase energy density. High mechanical properties of ANF suppress dendrite formation, and tunability with different copolymers and fabrication methods allow ANF-based nanocomposites to meet specific needs of different battery chemistries.

In the first part of this thesis, we engineered biomimetic solid electrolyte from ANF and polyethylene oxide for zinc batteries inspired by the cartilage structure. These strong nanocomposites can block stiff zinc dendrite formation and prevent short circuits over cycles. Resilience to plastic deformation and damage while having no leaking fluids or cracks is essential for the safety of, for instance, electrical vehicles employing such batteries. These load-bearing batteries can be used as a structural component and increase energy density by simply avoiding inactive parts. As a proof of concept, we utilized this battery on a commercial drone as an auxiliary energy storage unit to extend flight endurance by about 20%.

In the second part of the thesis, we address a specific polysulfide shuttle problem in lithium-sulfur batteries utilizing bioinspired ANF nanocomposites. Mimicking ion channels on the cell membrane, we engineered biomimetic nanochannels (1nm diameter) for selectively allowing lithium-ion passage while physically blocking lithium polysulfide species (>2nm) on the cathode side. Selective ion transport through nanochannels is also modeled by finite element analysis, COMSOL. These ion channels allow us to reach >3500 cycles.

In addition to previous solid and liquid electrolyte systems, here in the last part of the thesis, we present a tunable quasi-solid polymer electrolyte to take advantage of both electrolyte features while minimizing their individual risks and drawbacks. Similar to the kidney filtration system, specifically the glomerular basement membrane, this gel electrolyte filters ions depending on their size and charge. Selective permeability and regulated ion transport provide safe and stable charge/discharge cycles. High mechanical properties keep functionality under extreme conditions, including high temperature and nail penetration. To show practical utilization of our structural batteries, we integrated pouch cells in various prototypes, including health monitoring devices, robotic prosthetics, and electric vehicles.

Taken together, mimicking structural and functional properties of multifunctional biological materials, i.e., cartilage, we present a novel multifunctional nanocomposite system that can be tailored to the specific needs of numerous structural energy storage applications.

Chapter 1
Introduction

1.1 Structural Energy Storage

Living organisms broadly use load-bearing organs for more than one function. For instance, bones serve our body not only in their structural capacity but also for blood regeneration. The carapaces of crustaceans serve as their armor against predators and as brood chambers. While the notion of multifunctional biomimetic machines has been around since the drawings of Leonardo Da Vinci, the practical realization of many multifunctional *load-bearing* parts has only recently become feasible. Versatile manufacturing technologies with unprecedented nanoscale accuracy, harnessing nanoparticle self-assembly phenomena for industrial production, and biomimetic materials with previously unknown combinations of properties have emerged over the last two decades to open the possibility of adding new functions to load-bearing parts.

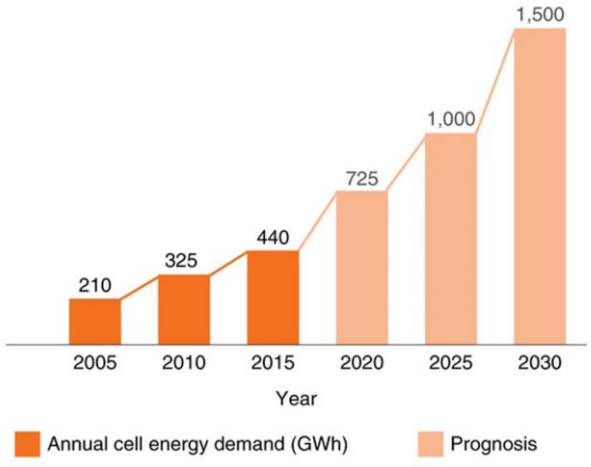

Figure 1.1: *Development of the rechargeable battery market size over time (Retrieved and modified from* [1] *).*

With the increasing demand for rechargeable batteries **(Figure 1.1)**, structural batteries are known to effectively reduce the total system weight [2], [3] regardless of the device size: from wearable electronics [4] to EVs [5] and airplanes [6]–[11]. For example, combining energy storage and load-bearing functions can reduce the total weight of an ideal EV by about 350 kg [6]–[11]. Energy storage integrated with protective and load-bearing parts is also essential for satellites of all dimensions and functions[9]–[11].However, structural batteries are not a part of the current technological landscape because of a fundamental conflict between load bearing and charge transport functions. These functions are contrarian to each other at the basic physicochemical level [3]. The simultaneous attainment of high ionic conductivity and high stiffness [12], [13] lead to opposite structural requirements to materials. The same is true for high mechanical strength and high ion intercalation capacity [14] an equally important pair of properties for structural batteries. This clash can be broadly described as the load-bearing functionality requiring strong chemical bonds and dense, robust materials. In contrast, charge transport and storage require weak chemical bonds and porous, deformable materials.

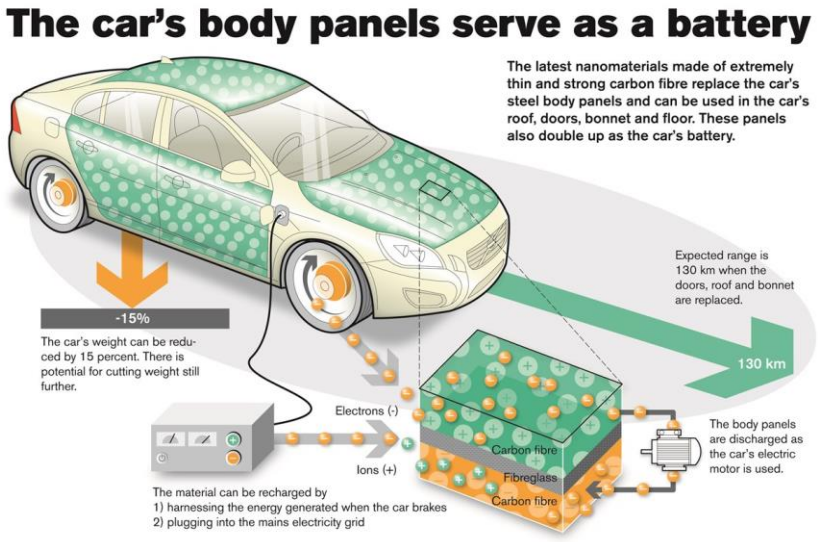

Figure 1.2: *Schematic of a structural battery prototype by Volvo (Modified from* [5]*).*

Out-of-box ideas are required to engineer novel multifunctional nanocomposites with such contrarian material properties (high ionic conductivity and mechanical strength) for the realization of safe and high-capacity structural batteries. Structural components around a battery in UAVs can weigh up to two times more than the battery itself and concomitantly limit the range and efficiency of the UAV [15]. On the other hand, decreasing the weight of a piloted aircraft by 1 kg saves 30 tons of fuel in a year[16]. Hence, a combination of energy storage and load-bearing functions is the critical parameter determining the duration and range of such devices or vehicles **(Figure 1.2)**. Structural batteries have a great potential to address the energy storage challenges of portable devices and electric vehicles [17]–[19].

1.2 Aramid Nanofibers for Ion Conducting Nanocomposites

Aramid nanofiber (ANF) is one of the strocngest flexible polymeric nanofibers with diameters between 3 and 30nm and up to 10μm in length [20], [21]**(Figure 1.3 a-e).** Aramid Nanofibers are made from Kevlar™ threads by controlled dispersion in dimethylsulfoxide (DMSO) and KOH [20]. Kevlar™ is an accepted ultra-strong para-aramid synthetic macroscale fiber with a high tensile strength to weight ratio[22], [23]. Kevlar threads and yarns are made from PPTA (poly(paraphenylene terephthalamide)) **(Figure 1.3 f)** that are exceptionally strong and stiff with a tensile strength of 3.6 GPa and modulus of ~90 GPa [24].

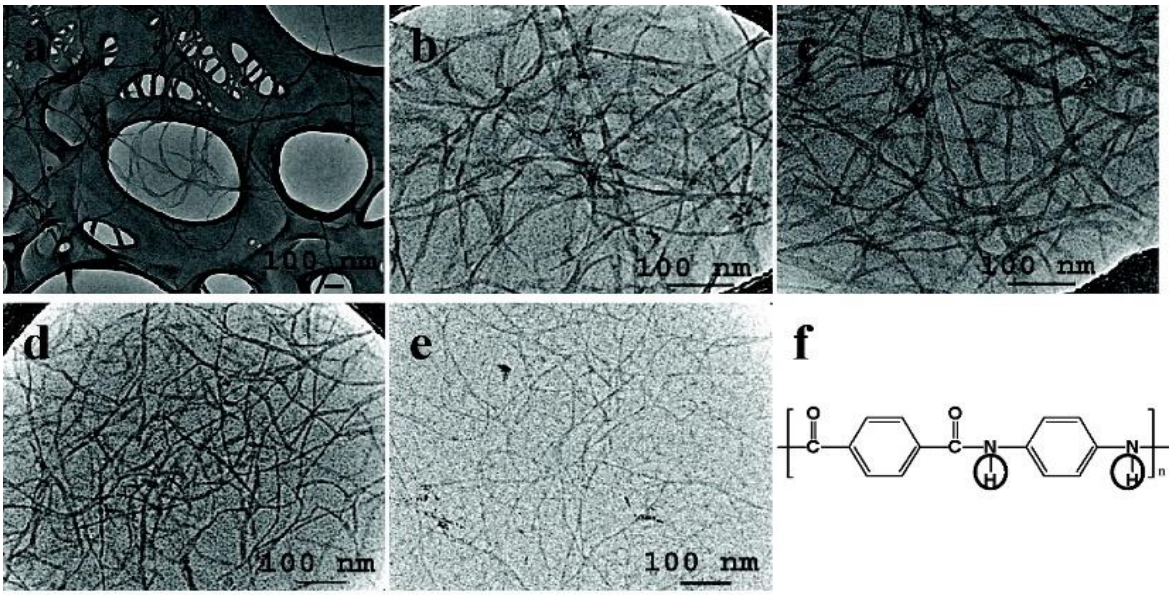

Figure 1.3: *TEM images of ANFs in DMSO solution with various diameters (a,d), one bilayer of PDDA/ANF (e), (f) The molecular structure of aramid. (Modified from* [20]*).*

ANFs can be processed into films using layer-by-layer (LBL) assembly to make composites from ANFs and poly(diallyldimethylammonium chloride) (PDDA) [20] or poly(ethyleneoxide) (PEO)[25]. In order to improve ionic conductive properties of ANF films, PEO was used as a solid ion-conducting media in LBL assembly[26]. Composite films made by LBL assembly have strong mechanical properties [20], [27]. Pure ANF and ANF composite membranes can also be fabricated by utilizing vacuum-assisted filtration (VAF)[28] and spin coating [29] methods. Another example of polymeric nanofiber dispersion is cellulose [30]. These nanofibers also exist in diameters of 3-30nm[31]. However, their rigid structure, low aspect ratio, molecular rigidity, and sensitivity to humidity limit their broader applications [32]–[34]. Mechanical properties of LBL structures from ANF are higher than cellulose nanofibers and carbon nanotubes [35], [36].

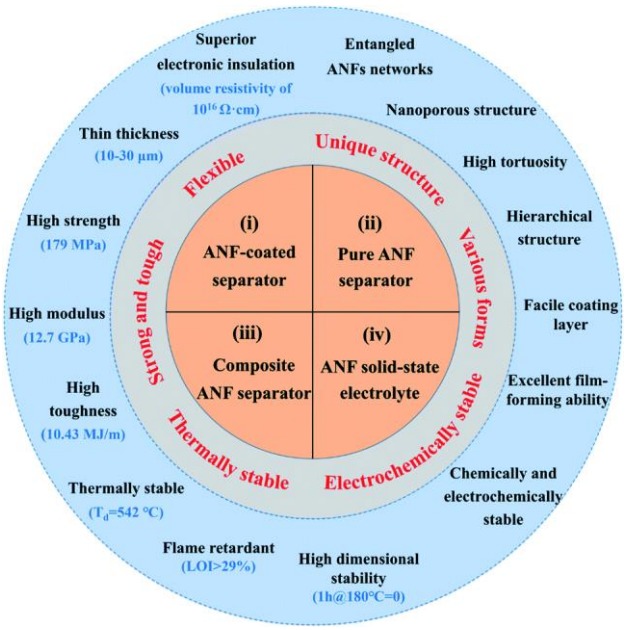

Figure 1.4: *Properties of ANF membranes and the classifications of ANF-based separators for LIBs. (Retrieved from* [37]*).*

Thin-film polymers are also used in battery assemblies as ion transporting separators to increase capacity and suppress dendrite formation between electrodes[25]. These films are required to have high ionic conductivity, high stiffness, and flexibility to produce durable, safe, and highly efficient batteries. They also need to be selectively permeable to ion transportation. Selective permeability of separators plays a crucial role in battery applications, especially for addressing the polysulfide shuttle problem in lithium-sulfur batteries. Also, any possible leakage between electrodes can cause short circuits and fires[38], [39]. Therefore, providing a strong ion conductive separator is vital for increasing the safety and efficiency of the battery. In addition to ANF composites, pure ANF [28], ANF coated [40] separators have also been reported due to ANF's high mechanical and thermal stabilities and substantial electrochemical properties **(Figure 1.4)** [37].

1.3 Bioinspired ANF Nanocomposites for Addressing Structural Energy Storage Challenges

Multifunctional natural nanocomposites inspire researchers to engineer abiotic replicas with similar structures and functions. Similarly, the challenging combination of high mechanical properties and high ion transport properties can be possible by mimicking natural blueprints, supporting tissues. Properties of these issues have been optimized over the years and presented by articular cartilage **(Figure 1.5A)**, basement membrane **(Figure 1.5B)**. These tissues have a fundamental structural motif represented by a porous three-dimensional (3D) network of stiff nanoscale fibers with 20–100 nm pores **(Figure 1.5C)**. Abiotic replicas of such networks **(Figure 1.5D)** have been made from branched aramid nanofibers (BANFs) that retain the outstanding mechanical properties of their precursor - the iconic ultra-strong material Kevlar^{TM}. Similar to their biological prototypes, BANFs can be self-assembled from individual fibers, and their manufacture is scalable.

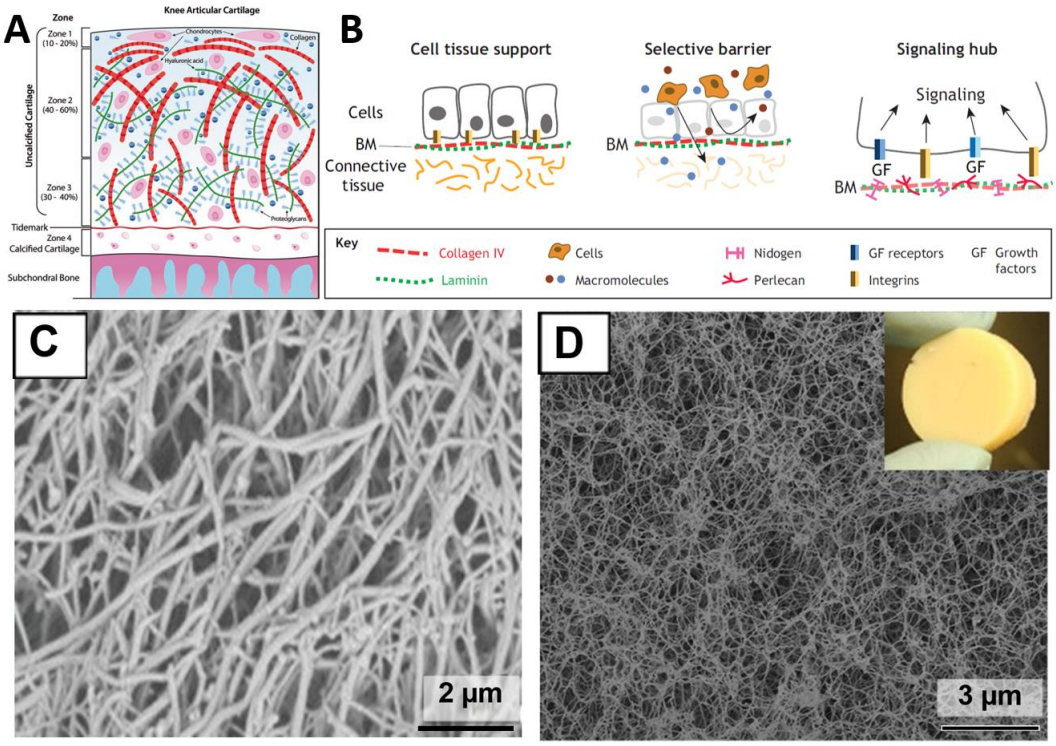

Figure 1.5*: Schematic of Knee Articular Cartilage Structure (Retrieved from* [41]*). (B) Schematic representation of different functions of the BM. The BM provides mechanical support to cells (left), regulates the selective passage of cells and/or macromolecules (center), and acts as a signaling hub by concentrating various proteins (right). (Retrieved from* [42]*. Scanning electron microscopy (SEM) images of (C) cartilage (courtesy of Dr. Nipun Chadha, Department of Biomedical Engineering, U. Rochester) and (D) 3D fibrous network from aramid nanofibers used in (inset) (Modified from* [43]*).*

1.4 Graph Theory Description of Biomimetic ANF Network

The mechanical and ion transport properties of bioinspired nanocomposites can be rationalized by applying a graph theory (GT) description of the ANF network architecture **(Figure 1.6)**. Continuous aramid fibers are denoted as edges, and intersections are represented as nodes in this 2-Dimensional GT representation[44]. GT helped us engineer a new type of ion conductor where ANFs were combined with a soft ion-transporting component: quaternary ammonium functionalized polyvinyl alcohol (QUPA) to selectively conduct hydroxide (OH^-) anions essential to the Zn-air battery[45]. Remarkably, our biomorphic batteries provide 72 times greater capacity and longer operating time than a LIB with the same volume.

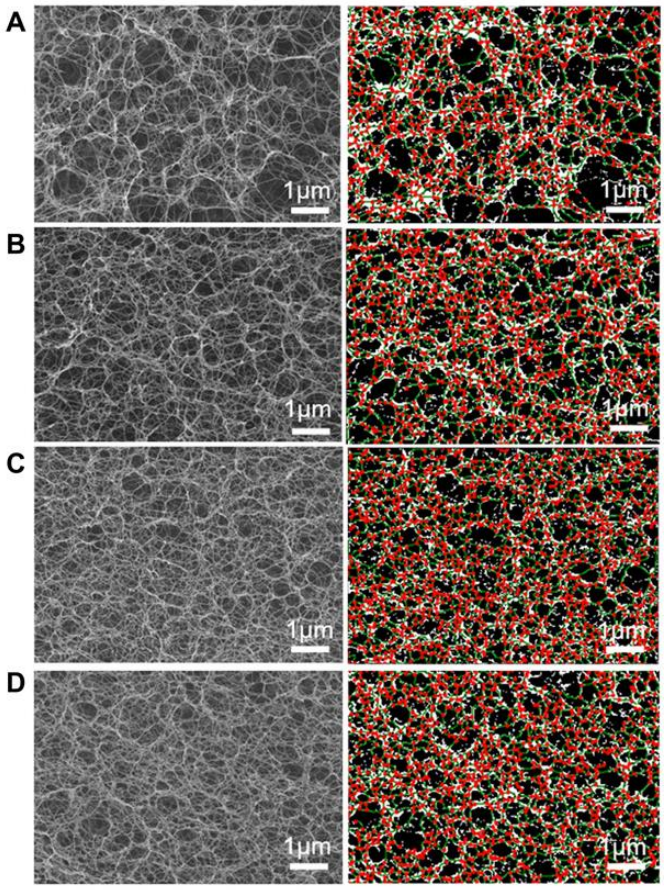

Figure 1.6: *Graph theoretical description of nanofiber composites. The left and right columns display SEM images of the ANF composite surface, its GT representation obtained from StructuralGT. ANF aerogel membrane was prepared with different concentrations of ANF dispersion (A) 0.5, (B) 1.0, (C) 1.5, and (D) 2.0 wt %. (Retrieved from* [45]*)*

1.5 Translational Potential

Similar to other portable electric devices and vehicles; weight, limited energy density and safety are also challenges for the design and operation of mobile biomedical devices. Structural energy storage applications have the potential to increase the energy density of various biomedical devices, including but not limited to small health monitoring devices[46], implantables[47], and robotic legs [48], [49] **(Figure 1.7)**. Therefore, these devices can be potentially smaller for less invasive applications and operate longer with utilization of multifunctional materials.

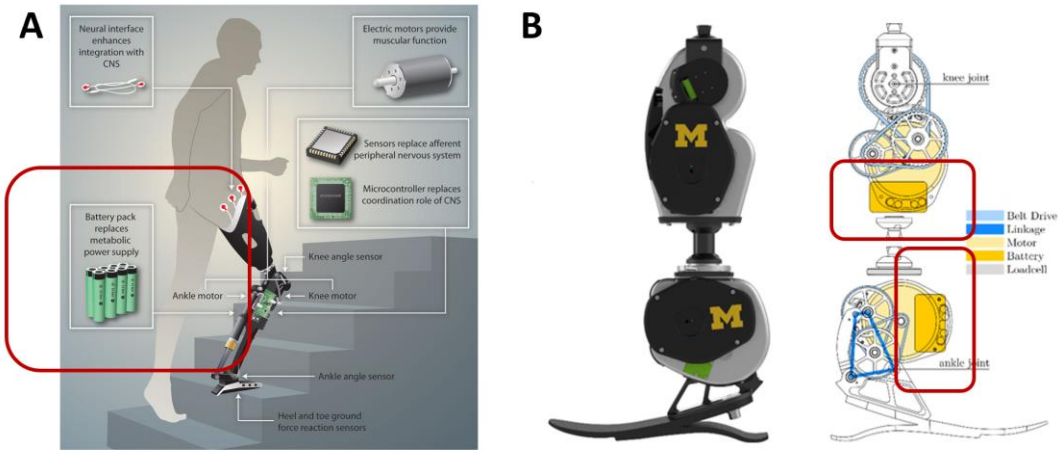

Figure 1.7: *Structural components of battery-operated robotic prosthetic legs (Retrieved and modified from* [48], [49]*)*

In summary, narrow pore size, negative surface charge, unique mechanical and thermal properties collectively lead the bioinspired ANF-based separator to the promising electrochemical performances in various battery chemistries, including but not limited to zinc and lithium-sulfur.

1.6 Research Goals

The overarching goal of the research presented in this dissertation is to survey the potential use of bioinspired aramid nanofiber composites for efficient structural energy storage applications. Within this, our specific goals are:

1- Inspired by a cartilage structure and function, develop a solid-state polymer electrolyte from ANF, PEO and ZnTF to address dendrite and cyclability issues of Zinc batteries to enable plastically deformable structural batteries.

2- Similarly, inspired by ion channels, engineer a nanoporous membrane by ANF, PDDA Layer by Layer assembly to address dendrite formation and lithium polysulfide passage problems in Lithium-Sulfur Batteries.

3- Mimicking structure and function of basal membrane, develop a quasi-solid electrolyte from ANF, PVA, and LiTFSI to address safety and performance issues of Lithium-Sulfur Batteries.

Chapter 2

Biomimetic Solid-State Zn^{2+} Electrolyte for Corrugated Structural Batteries

2.1 Abstract

Batteries based on divalent metals, such as Zn/Zn^{+2} pair, represent attractive alternatives to lithium-ion chemistry due to their high safety, reliability, earth-abundance and energy density. However, archetypal Zn batteries are bulky, inflexible, non-rechargeable, and contain a corrosive electrolyte. Suppression of the anodic growth of Zn dendrites is essential for resolution of these problems. However, materials with mechanical properties allowing them to withstand mechanical deformation from stiff Zn dendrites and transport Zn^{2+} ions, are virtually unknown. Here we show that it is possible to engineer a solid Zn^{2+} electrolyte as a composite of branched aramid nanofibers (BANFs) and poly(ethyleneoxide) by using the nanoscale organization of articular cartilage as a blueprint for its design. The high stiffness of the BANF network combined with the high ionic conductivity of soft poly(ethyleneoxide) enable effective suppression of dendrites and fast Zn^{2+} transport. The cartilage-inspired composite displays the ionic conductance 10x higher than the original polymer. The batteries constructed using the nanocomposite electrolyte are rechargeable and have Coulombic efficiency of 96%-100% after 50-100 charge-discharge cycles. Furthermore, the biomimetic solid-state electrolyte enables the batteries to withstand not only elastic deformation during bending but also plastic deformation. This capability makes them resilient to different type of damage and enables shape modification of assembled battery to improve the ability of the battery stack to carry structural load. The corrugated batteries can be integrated into

body elements of unmanned aerial vehicles (UAVs) as auxiliary charge storage devices. This functionality was demonstrated by replacing the covers of several small drones with pouch-like Zn/BANF/MnO_2 cells, resulting in the extension of the total flight time. These findings open a pathway to design and utilization of corrugated structural batteries in the future transportation industry and other fields of use.

2.2 Introduction

Batteries based on Zn and other divalent metals [50] attract renewed attention because of their greater safety, reliability, and natural availability compared to lithium. Having theoretical energy densities similar to those of lithium-ion batteries, [51], [52] they are attractive as energy storage solutions for many applications. However, the iconic alkaline batteries with Zn anode, a MnO_2 cathode and concentrated KOH (6 mol/L) as electrolyte are bulky and non-rechargeable. These batteries can leak corrosive fluid and have energy densities 7-10 times lower than Li-ion batteries.[4,5] Early studies on rechargeable Zn/MnO_2 [53]–[57] batteries showed severe capacity fade due to the formation of byproducts,[58] irreversible cathode chemistry in alkaline media,[58], [59] and the growth of dendrites. [60], [61] The dendrite growth has the largest impact on energy density and cyclability for all Zn batteries, as Zn dendrites (Young's modulus E = 108 GPa)[62] can easily traverse the inter-electrode space piercing existing plastic separators (**Figure 2.1**, A to B). Liquid organic Zn^{2+} electrolytes make metal deposition on the anode more uniform and improve the reversibility of cathode chemistry, [63]–[68] however, the problem of dendrite growth persists [69], [70] and a new problem of flammability emerges. Recently, rechargeable batteries were constructed using three-dimensional (3D) electrodes [71], [72] in the form of Zn sponges, [73] Zn-on-Ni foams, [68] or carbon cloths [74] in order to alleviate the problem of anode-to-cathode bridging by dendrites. While demonstrating impressive cyclability, the 3D electrodes

increase the bulk of the anode and make them prone to mechanical damage, while increasing the likelihood of leakage of the liquid electrolyte. Solid electrolytes [25], [75], [76] with Young's moduli comparable to those of the Zn dendrites have the potential to eliminate these problems, even if quasi-solid separators based on gels and porous polymers [68], [74], [77]–[80] cannot. However, organic or inorganic solids with efficient ion transport of divalent ions are little-known, especially when compared with the wealth of knowledge regarding polymers, composites, and glasses for transport of lithium ions. [81], [82]

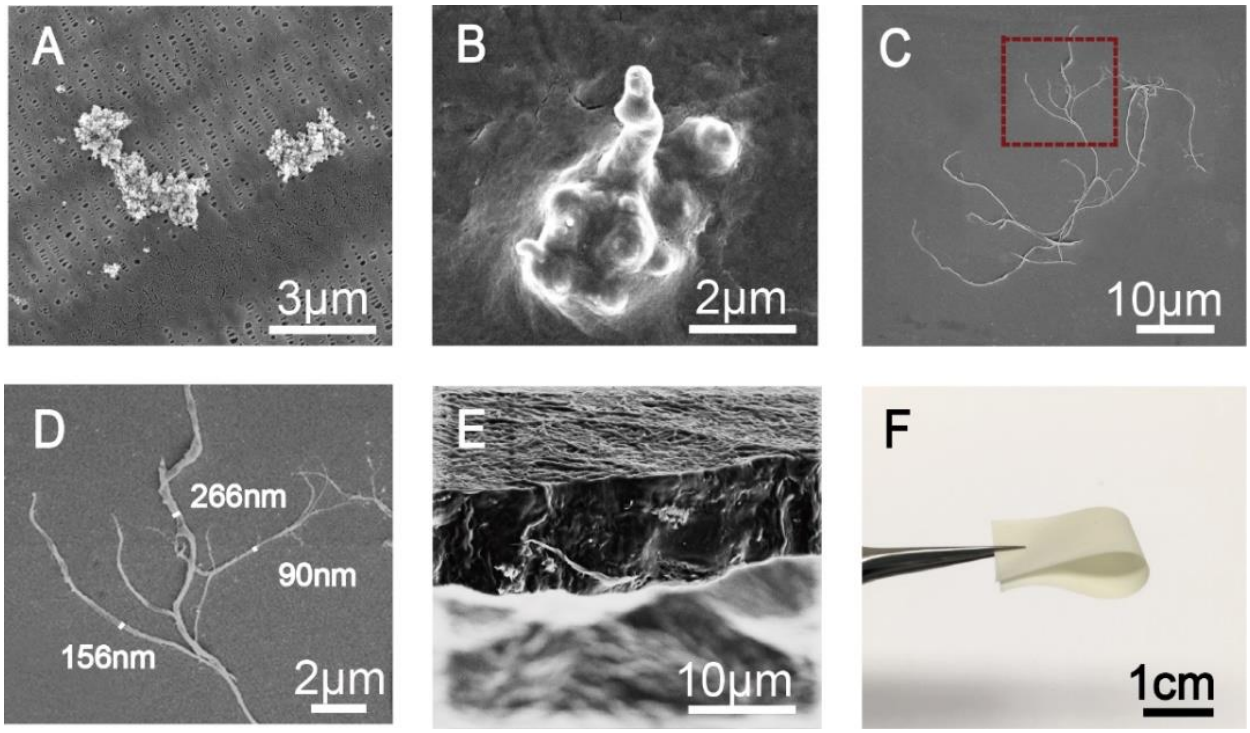

Figure 2.1*: (A) SEM image of zinc dendrites penetrating through a CelgardTM 2400 separator. (B) SEM images of the tip of a zinc dendrite. (C and D) SEM images of BANFs. (E) SEM image of the cross-section, and (F) photograph of the free-standing PZB-931 composite electrolyte.*

Building on the concepts of biology-inspired design of battery components[25], [83]–[89] investigated for Li chemistries, we report herein the development of a solid-state electrolyte for Zn^{2+} based on branched aramid nanofibers (BANFs) that replicates the fibrous structure of articular cartilage, which is known for combining efficient mass transport with high mechanical

properties.[43], [90]–[92] The resulting composite combines excellent ionic conductivity of Zn^{2+} with a high tensile modulus. The replacement of the traditional alkaline electrolyte with a BANF composite drastically changes the mechanism of ion transport, electrode processes including the dendrite growth and results into a flexible, rechargeable battery with cyclability of >100 cycles and >90% charge retention. Importantly, the cartilage-like BANF-based electrolyte imparts these thin film batteries with the ability to withstand not only elastic deformations during extreme bending and other but also plastic deformation during stamping without the loss of capacity or voltage. This unusual combination of properties with the charge storage parameters comparable to those of lithium thin film batteries (**Table 1** and **Table 2**)[93]–[95] opens to path to lightweight high-capacity batteries with higher load-bearing capabilities and better safety profile than structural batteries with lithium ion chemistry.[96]–[98] A large variety of corrugated shapes adaptable to specific load-bearing conditions including unmanned aerial vehicles (UAVs) is anticipated.

2.3 Results and Discussion

Aramid nanofibers used in this study were made from Kevlar^{TM} microfibers by high-energy agitation in DMSO (see Methods). These fibers serve as the high-strength components of the composite electrolyte [20] and mimic the stiff collagen nanofibers of cartilage. The BANFs have a branching geometry with approximately five to six fork-points in each fiber (**Figure 2.1**, C and D). The principle 'stems' has an average diameter of 200-300 nm while the branches have diameters of 50-100 nm. Multi-point bifurcation of these filaments facilitates the formation of a fibrous 3D network with a large volume fraction of nanoscale pores necessary for ion transport. Similarly to the structure of soft tissues, the efficient entanglement of nanoscale branches lends high stiffness to the material on both macro- and nanoscales needed for the prevention of dendrite

growth.[25], [99], [100] Besides branching, the aromaticity and amphiphilicity of BANFs offers a wider range of charge transporting media than hydrophilic 3D networks including solid-state ion-conducting polymers compared to 3D networks observed for nanocellulose, [78], [79], [101], [102] alginate [87] and peptides.[103] High toughness characteristic of all 3D nanofiber networks engenders resilience to extreme deformations.[43]

Poly(ethyleneoxide) (PEO, MW = 300,000 Da) and $Zn(CF_3SO_3)_2$ serve as ion-transport components of the non-corrosive solid electrolyte; these components can be compared to the soft proteoglycan portion of natural cartilage. The composition of the PEO : $Zn(CF_3SO_3)_2$: BANFs (PZB) mixture was optimized with respect to Zn^{2+} conductivity and mechanical properties. High weight ratios of $Zn(CF_3SO_3)_2$ cause both the increase of ionic conductivity, δ, and decrease of tensile moduli, E, vividly illustrating the contrarian nature of materials design requirements for fast transport and high mechanical properties. Based on the experimental $\delta - E$ dependence (**Figure S 1**), the optimal PZB weight ratio was selected to be 9:3:1. This composite is denoted as PZB-931 and this notation will be used throughout this study. PZB-931 combines high ionic conductivity for Zn^{2+} (δ = 2.5 x 10^{-5} S/cm, room temperature 22°C) (**Figure S 1**), high tensile strength (σ = 58±2.9 MPa) and a high Young's modulus (E = 210 ± 11 MPa). Compared to PEO (E = 3.3±0.2 MPa), it shows a 64-fold higher Young's modulus. compared with composite films based on aligned cellulose fibers and CNTs,[35], [104], [105] the tensile modulus of PZB-931 is seven times higher (**Figure S 2** and **Table 3**). Improvements in E are essential for defeating the dendrite growth. [25], [100]

The ionic conductivity for Zn^{2+}, δ, of neat PEO infused with $Zn(CF_3SO_3)_2$ is δ = 2.3 x 10^{-6} S/cm. Addition of BANF *decreases* of the volume fraction of PEO and thus might be expected to reduce the ionic conductivity of the composite. However, the opposite effect is observed. The

ionic conductivity for Zn^{2+} *increases* 10x for BANF-PEO composites made here. Further increase of δ is observed, as expected, at higher temperatures (**Figure S 9** and **Table 4**).

The high ionic conductivity in PZB-931 is ascribed to the amorphous state of the polymer[25], [106], [107] integrated into BANF network of nanofibers. Based on the dependence of δ vs BANF loading (**Figure S 5**), XRD (**Figure S 6**), FT-IR (**Figure S 7**) and DSC measurement (**Figure S 8**), the crystallization of PEO is disrupted due to amphiphilicity of aramid surface and entanglement with BANF network. The typical inter-filament distances in BANF networks is 50-70 nm (**Figure S 4**), which are three orders of magnitude smaller than the size of the typical PEO crystallites that is ~50,000 nm.[108], [109]

Also important that the inter-filament distances in the BANF network are 10-20 and 2-4 times smaller than the average diameters of stems (1-2 μm) and growth points (~200 nm) of the Zn dendrites (**Figure 2.1**B). The small pore size, high Young's moduli of individual fibrils and elimination of liquid electrolyte differentiate this material from previous concepts of ion-transporting media for Zn^{2+}.[63]–[65], [68], [74], [106], [110], [111] PZB-931 composite also made possible preparation of electrolyte sheets with a thickness as thin as 10±0.50 μm (**Figure 2.1** E, **Figure S 3**, which is thinner than a typical separator in Zn or Li batteries (typically ranging from 30 μm to 200 μm) . [74], [79], [102], [112] These robust sheets are also thinner than ion-conducting glasses in thin-film Li batteries (from 30 μm to 1000 μm). [113]–[115] Reduction of the thickness of the ion-transporting media while retaining sufficient overall stiffness, strength, and toughness is highly desirable for all batteries because it increases the volumetric density and reduces weight of the batteries.

MnO_2 was used as a cathode material, in part, because it highlights the transformative effect of the solid electrolyte on the battery functionality and design. The reversibility of γ-MnO_2

with respect to storage of Zn^{2+} ions with PZB-931 as ion-transport media was established by cyclic voltammetry (CV) scans (**Figure 2.2** A, **Equation 2**), XPS (**Figure S 10** and **Figure S 11**) and XRD (**Figure S 12**) spectra obtained for the original, Zn-rich, and Zn-depleted states.

The cycling curves of the full battery cell Zn/PZB-931/γ-MnO_2 (**Figure S 13**) revealed discharge capacities of 146.2, 129.5, 106.7 and 89.2 mAg^{-1} at 0.1, 0.2, 0.5 and 1.0 C (1C = 150 mAg^{-1}), respectively (**Figure 2.2** B and D). The voltage initially drops at the beginning of the discharge step due to the internal cell resistance. Specific capacity and Columbic efficiency of Zn batteries with solid-state PZB electrolytes match those with liquid electrolytes (**Figure S 14**) and substantially better than batteries with solid PEO electrolyte. After 50 cycles (**Figure 2.2** C, E), the battery with PZB-931 retains 96% of its highest achievable capacity that is 123.4 $mAhg^{-1}$. Columbic efficiency exceeded that of 90% after 100 cycles (**Figure 2.2** E). Coulombic efficiency was found to be ~100% for the initial 50 cycles and 96% at the 100^{th} cycle. The charge storage performance of Zn/PZB-931/γ-MnO_2 is competitive with many Zn batteries with liquid and gel electrolytes (**Table 5**) and flexible Li ion batteries (**Table 2**).

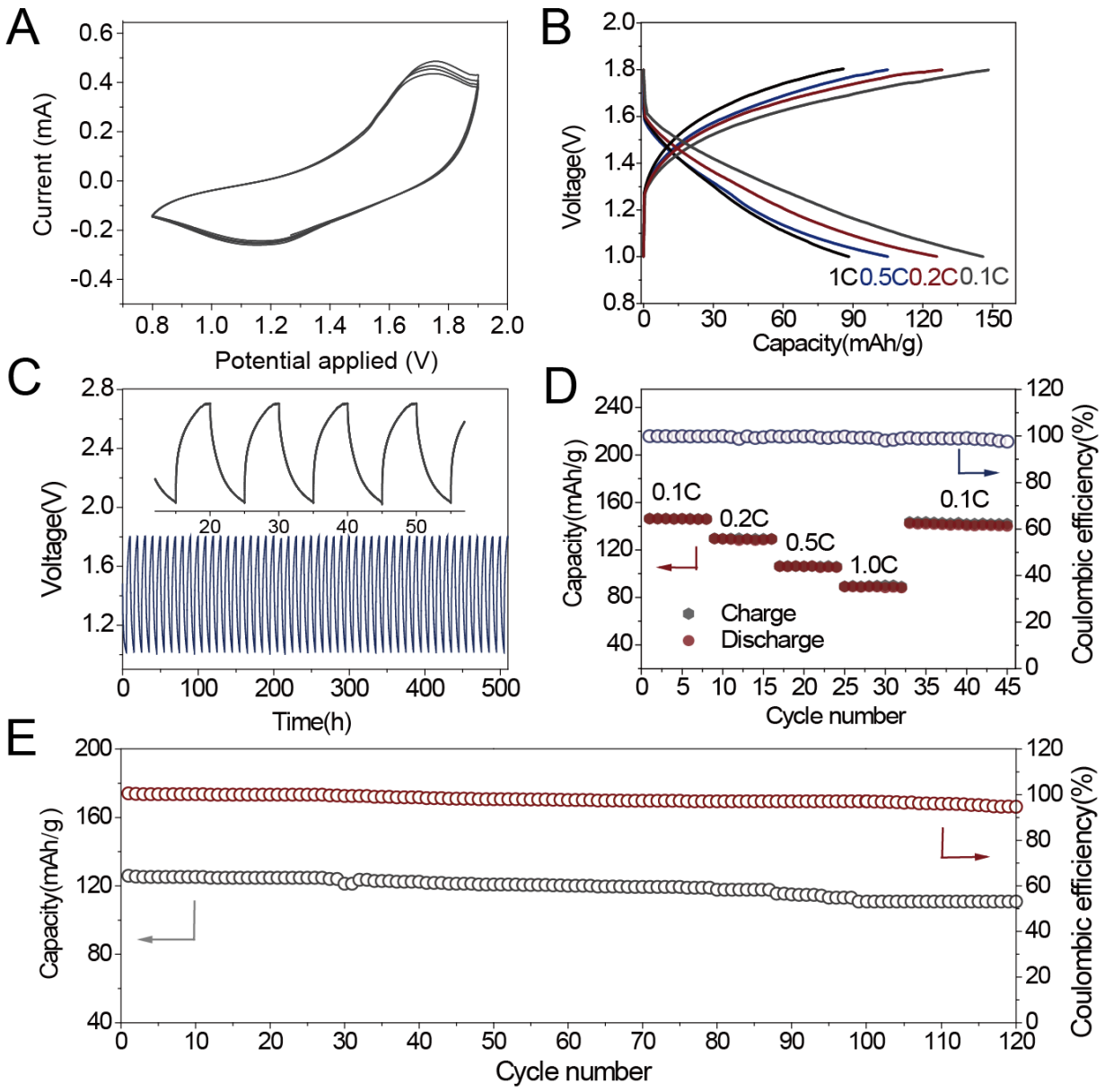

Figure 2.2 *(A) CVs of Zn/PZB-931/γ-MnO2 battery scanned at 0.1 mVs-1. In cathodic scans, a peak at 1.2 V is attributed to the electrochemical intercalation of Zn2+ ions into γ-MnO2. In anodic scans, a peak at 1.65 V is attributed to extraction of Zn2+ ions. CV curves remain unchanged after five cycles, demonstrating nearly ideal reversibility of the cathode material between Zn-rich and Zn-depleted states. (B and D) Galvanistatically charge and discharge curves and rate capability of the Zn/PZB-931/γ-MnO2 battery cycling within the voltage range of 1 V-1.8 V at current density from 0.1 C to 1.0 C (1 C = 150 mAg–1). (C) The voltage-time curve for the Zn/PZB-931/γ-MnO2 battery discharge and charge at 0.2 C. (E) Cycling performance of the Zn/PZB-931/γ-MnO2 battery at 0.2 C.*

The effective dendrite suppression by PZB-931 engenders rechargeability of the battery and long cyclability performance.[69], [70], [116] To experimentally demonstrate dendrite suppression by PZB-931, electrochemical processes in a symmetrical Zn/PZB-931/Zn cell were

evaluated for charge-discharge cycles promoting dendrite growth (**Figure 2.3**A). The cell with a neat PEO film (**Figure 2.3**B) showed voltage oscillations caused by the unstable electrode/electrolyte interface due to mechanical detachment of the PEO film from the Zn under pressure of dendrites. During cycling for 440 h, zinc dendrites pierced the separator, resulting in a short-circuit. An identical cell with Celgard^{TM} 2400 impregnated with an organic liquid electrolyte based on $Zn(CF_3SO_3)_2$ (**Figure 2.3**D) showed a steady decrease in its voltage, indicating the so-called 'soft shorting' when dendrites are slowly penetrating ion-transporting membrane (**Figure 2.1** B). Under the same conditions, the symmetrical cell with PZB-931 exhibited cycling stability with negligible potential loss or fluctuation (**Figure 2.3**C). After cycling for as long as 2500 h, no sign of cell failure was observed, indicating that the growth of Zn dendrites was effectively suppressed. Despite electrochemical conditions promoting the dendrite growth, the scanning electron microscopy (SEM) evaluation of the electrodes after 500 h of cycling showed pristine zinc electrodes (**Figure 2.3**, E to H).

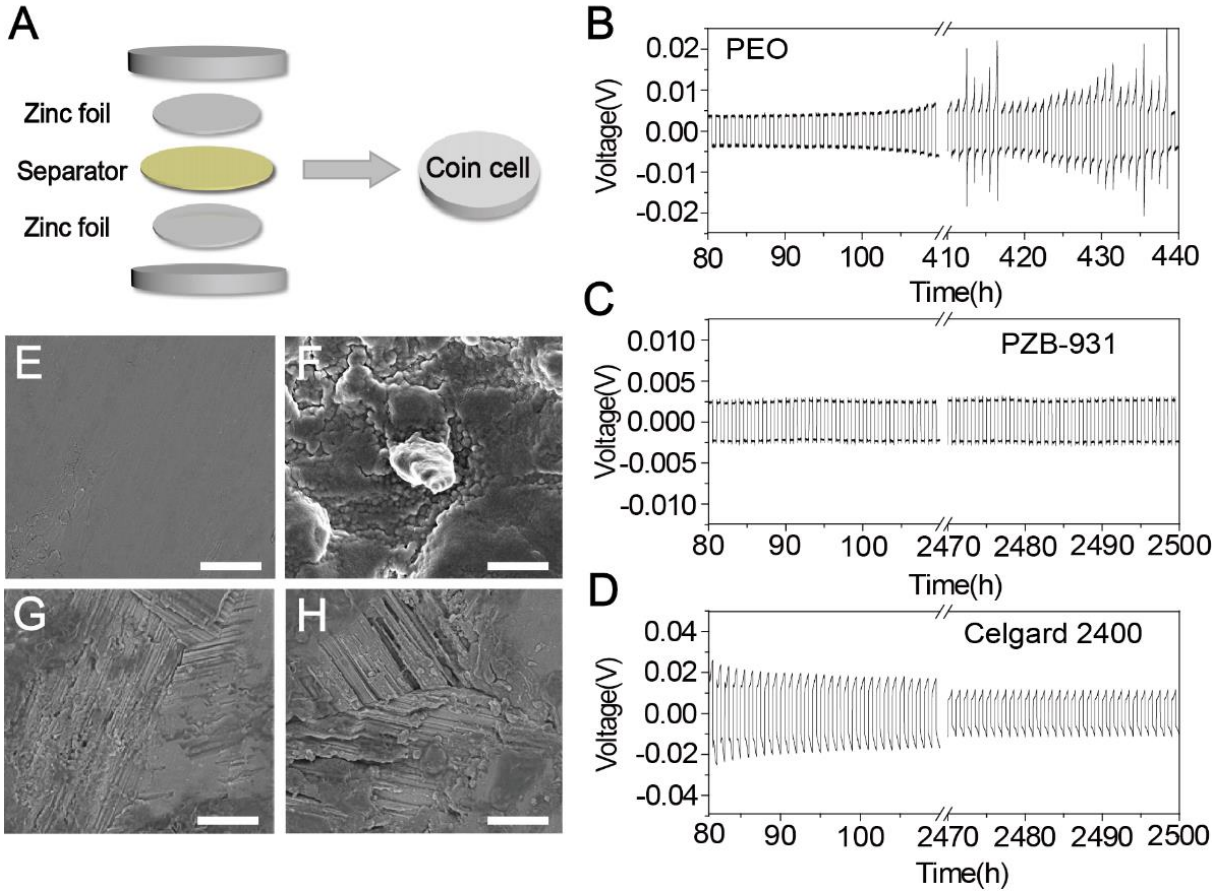

Figure 2.3 *(**A**) Configuration of the symmetrical Zn/electrolyte/Zn cell. (**B** to **D**) galvanostatic cycling curves of the cells with different polymer film separators of (**B**) PEO film (with $Zn(CF_3SO_3)_2$ salt), (**C**) PZB-931 film (with $Zn(CF_3SO_3)_2$ salt), and (**D**) Celgard™ 2400 separator (3 mol L^{-1} $Zn(CF_3SO_3)_2$ N-methyl pyrrolidone (NMP) solution) at current densities of 0.2 mA cm^{-2}. The current direction was changed every 0.5 h. (**E** to **H**) SEM images of the zinc electrode surface before and after 500 h of cycling under different electrochemical conditions, (**E**) original zinc foil surface. (**F**) Zinc foil surface after cycled with PEO separator (neat, no $Zn(CF_3SO_3)_2$), (**G**) Zinc foil surface after cycled with PZB-931 separator (neat, no $Zn(CF_3SO_3)_2$), and (**H**) Zinc foil surface after cycled with Celgard™ 2400 separator with a liquid electrolyte, namely 3 mol L^{-1} $Zn(CF_3SO_3)_2$ NMP solution. Prior to SEM imaging, the zinc electrode surface of Celgard™ 2400 film was thoroughly washed with NMP solution to remove any electrolytes or salt residues. Scale bar 5 µm.*

The biomimetic composite PZB-931 enables the Zn batteries to become not only rechargeable but also deformable. They were found to be capable of withstanding damage that would be impossible for other batteries[75], [81], [114] (**Figure 2.4**A to H, **Figure S 15** and **Figure S 16**). While the elastic deformations have been extensively shown for different types of batteries

before,[68], [74], [77]–[80] the ability to withstand plastic deformations while retaining the charge storage functions was not.

Zn batteries with PZB-931 were corrugated by molds (**Figure 2.4A**) with different 'teeth' shaped as square (**Figure 2.4B**), half-sphere (**Figure 2.4C**), dot (**Figure 2.4D**), square wave (**Figure 2.4**E), or round wave (**Figure 2.4F**). The battery voltage and capacity remained virtually unchanged and its power showed no significant decay under a variety of deformation conditions (**Figure S 17**) and corrugated states (**Figure S 17** to **Figure S 20**). While plastic deformability has obvious limits, the constancy of the EIS (**Figure 2.4J**, **Figure S 20** and **Figure S 21**) and galvanostatic charge and discharge (**Figure 2.4I**) for the studied range of deformations is remarkable. Furthermore, the battery was stabbed and cut in various places multiple times, and it was still holding the voltage. Resilience to this kind of damage while having no leaking fluids or cracks is crucial for safety of, for instance ground and aerial vehicles employing such batteries. The multi-parameter comparison with other flexible batteries indicates that these batteries are comparable or exceeding the corresponding parameters of other batteries based both on Li and Zn chemistries (**Table 1**, **Table 2**, **Table 5**, **Table 6**).

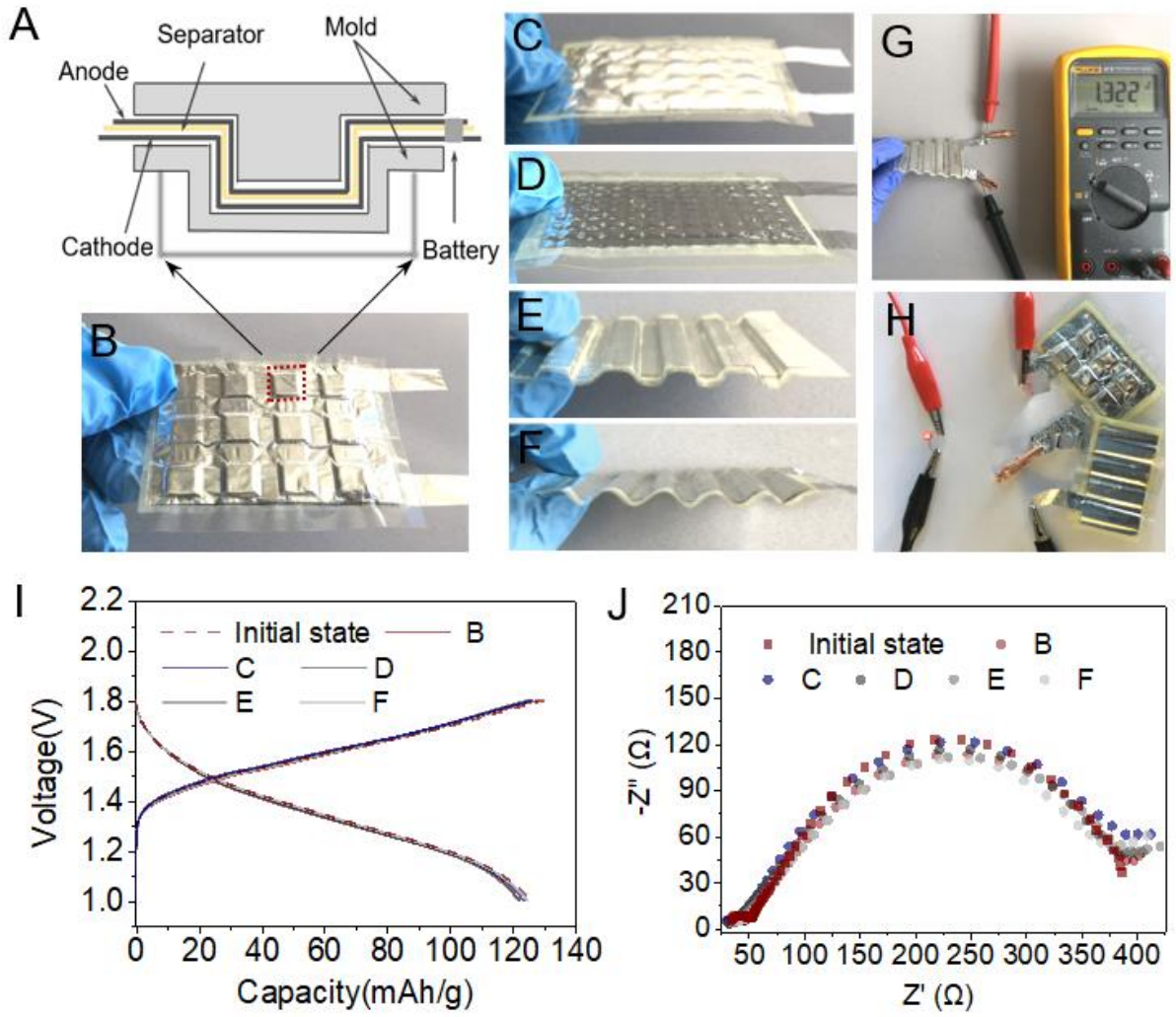

Figure 2.4 *(A) Schematic of the mold used for plastic deformation studies. (B to F) Different plastically deformed shapes of Zn battery with solid state biomimetic electrolyte PZB-931. (G) Open circuit voltage of Zn/PZB-931/γ-MnO2 battery with square wave shape plastic deformation. (H) LED light powered by the two serial structural batteries. (I) Galvanostatic charge and discharge curves of Zn/PZB-931/γ-MnO2 at 0.2 C for the corrugation batteries in B-F. (J) Comparison of EIS curves for original and plastically deformed corrugation batteries in B-F. No change in EIS can be observed even for high degree of plastic deformation as in (B) indicating high damage tolerance.*

We furthermore tested the Zn/PZB-931/γ-MnO2 pouch cells similar those in **Figure 2.4** as structural batteries for UAVs. Taking advantage of the plastic deformability of these devices we shaped them to replace covers of UAVs enabling them to serve as auxiliary charge storage devices supplementing main power source with lithium-ion chemistry. The lightness of the auxiliary battery back afforded by the replacement of the liquid electrolyte with thin layers of dendrite suppressing PZB-931 composite is essential for structural batteries in aerial vehicles. The

versatility of our approach of utilization of structural batteries in UAVs was demonstrated for several commercially available drones of different types and power requirements (**Figure 2.5**). In all cases we observed successful take off with charge-storage covers. The structural Zn batteries were connected to the power circuits of the drones as secondary energy sources enabling the extension of the flight time. Given the battery characteristics from **Figure 2.2**, the flight time extension was calculated to be between 5 and 27% depending on the mass of the drone ambient temperature, flight patterns, and size of the batteries.

Figure 2.5 *(A) Tested UAV without cover. (B, C, D) Three different designs of corrugated Zn/γ-MnO2 battery pack as a replacement for the original device cover to supplement main power source of UAVs. All modified drone models with Zn/PZB-931/MnO2 structural batteries installed were demonstrated to successfully take off even under low ambient temperature.*

2.4 Conclusion

The cartilage-like nanofiber network design of PZB composites results in a unique combination of a fast ion transport and high mechanical properties. Hence, PZB and similar materials can serve as solid electrolytes that support reasonable discharge rate combined with effective dendrite suppression. [99], [100], [117] Their structural design offers a pathway towards the solid-state electrolytes for other multi-valent ions, such as Mg^{2+} or Al^{3+} needed for energy technologies. The ability of the Zn batteries with PZB-931 electrolyte to plastically deform and remain functional differentiates them from other promising charge storage devices, including electrochemical capacitors and supercapacitors[118] that can withstand predominantly elastic deformations in bending. [119] This unusual for charge storage devices property originates from (1) plasticity and inflammability of Zn anodes and (2) re-configurability of the fibrous cartilage-like network. From the practical standpoint, battery plasticity translates into marked increase of the battery safety and impact resistance. Plastic deformability makes possible to stamp the batteries into a variety of shapes including the ones that have complex convex-concave topography for load-bearing applications leading to a large family of structural batteries. The lightness and deformability of Zn/PZB-931/γ-MnO2 cells enabled them to successfully serve as a load-bearing and charge storage element in several commercial UAVs. These finding could guide future research in next generation of distributed energy storage in transport and other applications of structural batteries.

2.5 Experimental Methods

2.5.1 Preparation of Branched Aramid Nanofibers (BANFs)

1 g of bulk Kevlar^{TM} pulp from Dupont Co was dispersed in 500 mL of dimethylsulphoxide (DMSO) (≥99.9%, Sigma Aldrich) by stirring at room temperature in a FILMIX Model 56-L high

speed thin-film mixer. After 2 h, the dispersion was collected and placed in a centrifuge to spin at 10000 rpm for 10 min. BANFs with diameter of about 200-300 nm appeared as a white solid in a sediment. The nanofibers were washed with acetonitrile in a sequence of multiple centrifugation steps to get rid of all DMSO.

2.5.2 Fabrication of Poly(ethylene oxide)-Zinc Trifluoromethanesulfonate [$Zn(CF_3SO_3)_2$]-BANFs (PZB) Composite Ion Conductor

PEO with a molecular weight of Mw = 300000 Da, $Zn(CF_3SO_3)_2$ with 98 wt% purity, and acetonitrile with 99 wt% purity were purchased from Sigma-Aldrich and used as received. 1 g PEO (10 wt%), 0.33 g $Zn(CF_3SO_3)_2$, and 0.1 g BANFs were dissolved into a 8.61 g acetonitrile and 1-methyl-2-pyrrolidinone (NMP) at weight ratio, 9:1. For other PZB dispersions, the loading of BANFs was varied between 1 wt% and 15 wt% in respect to the weight of PEO. The obtained PZB dispersions were vigorously stirred at 50 °C overnight until visible aggregates disappeared. The PZB composite film was prepared by spin-coating followed by the lift off separation of the free-standing composite film.[120], [121] Microscope glass slides for the preparation of PZB film were pre-cleaned by extensive rinsing with deionized (DI) water (18 MΩ cm). 1 mL of PZB solution was dropped onto the glass slide and allowed to spread at 1800 rpm for 2 min. The polymer covers the glass slide smoothly and uniformly. Then composite membrane was dried in vacuum oven at 35^0C overnight. Subsequently, composite membrane was peeled from the glass slide using its own strength. Free-standing PZB membranes were dried between two PTFE plates for one day at room temperature.

2.5.3 Fabrication of Zn/PZB/γ-MnO_2 Cells and Battery Packs

The **γ-**MnO_2 powder (JCPDS # 14-0644) was synthesized by a process reported

before[122]. The cathode material layer consisted of 80 wt% γ-MnO_2, 10 wt% graphite, and 10 wt% PEO polymer binder. Graphite was purchased from Sigma Aldrich. PEO polymer binder was dissolved in acetonitrile to make a 5 wt% solution. The mixture of γ-MnO_2, graphite, and PEO binder was stirred at a speed of 3000 RPM for 1 minute three times using a planetary mixer. The resulting slurry was then cast onto an aluminum foil substrate using a doctor blade. The electrode was then dried in a vacuum oven for about 10 h at 35℃. Active material (γ-MnO_2) loading was 1.3mg-1.5mg /cm^{-2}. Before using the cathode material, the MnO_2 layer pressed at the 1000 MPa at 600 ^{0}C to enhance integrity of the material.

Anode layer was zinc foil, with a thickness of 5 μm, purchased from Sigma Aldrich. Pouch-like Zn/PZB/**γ-**MnO_2 cells were assembled by placing the electrodes face-to-face with the composite PZB film. Assembled cells were connected in series using copper paste as an external connection onto a polyethylene terephthalate (PET) film purchased from Sigma Aldrich serving as a flexible substrate.

Corrugated structural batteries were made from stacked Zn/PZB-931/γ-MnO_2 cells with a size of 5 cm x 7 cm. These cells were then connected in series to provide ~3.7V potential. This battery pack (~5.6g) was subsequently connected to the main power source of UAV via parallel configuration to supplement total current flow. It increased the total weight of UAV by ~10%. Even though contribution of our battery is relatively small, this concept can be improved and applied for next generation of UAVs.

2.5.4 Structural Characterization

The SEM images were taken with a FEI Nova Nanolab dual-beam FIB SEM. The FT-IR spectra were measured using a Nicolet 6700 spectrometer. The XRD patterns were obtained on a Rigaku Rotating Anode X-Ray diffractometer with Cu Kα radiation generated at 40 kV and 100

mA. X-ray photoelectron spectroscopy (XPS) was recorded on Perkin Elmer PHI 1600 ESCA. Quantachrome Autosorb 6B system was used to characterize the pore width of the BANFs film using nitrogen sorption under 77.4 K. The pore size distributions of the BANFs film was calculated by Barrett-Joyner-Halenda (BJH) methods. The mechanical properties of PEO and PZB composite films were conducted using a TA XT Plus Texture Analyzer (Stable Micro Systems Ltd.). The film was cut into rectangular strips of 20 mm × 5 mm, and twenty samples were tested in each case.

2.5.5 Electrochemical Measurements

Electrochemical impedance spectroscopy (EIS) (Autolab Potentiostat and Solartron 1260 frequency response analyzer) was carried out in the range from 100 kHz to 0.05 Hz with potential amplitude of 20 mV. The cell arrangements consisted of two zinc electrodes, which acted as blocking electrodes. The resulting Nyquist plots were fitted to an equivalent circuit where ionic conductivity was then calculated from the

Equation 1 $\sigma = L/R_bA,$

where L is the thickness of the film, R_b is the bulk resistance, and A is the contact area of film. Cyclic voltammetry (CV) curves of the assembled Zn/γ-MnO_2 with PZB were obtained using coin cellswith a scan range from 0.8 V to 1.9 V with a scan rate of 0.1 mV s^{-1}. Galvanostatic charge/discharge data was recorded on a LAND-CT2001A battery-testing instrument.

2.6 Supplementary Information

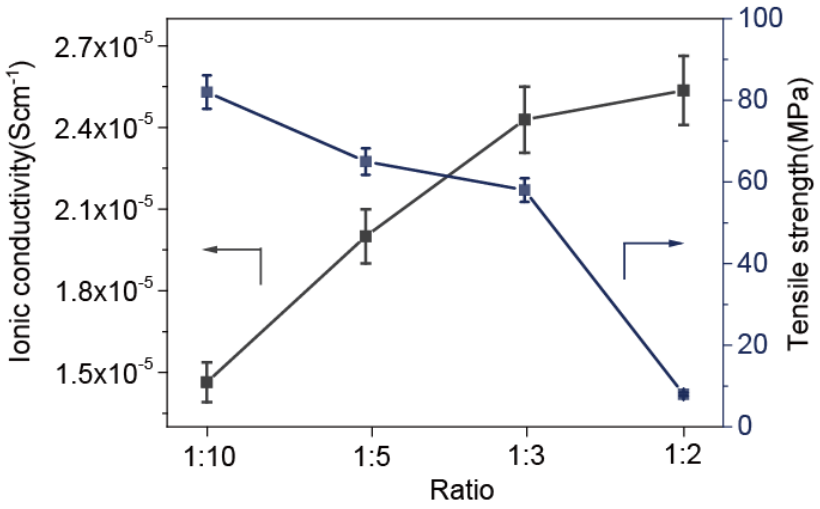

Figure S 1 *Characterization of ionic conductivity and tensile strength of PZB composites with different Zn(CF3SO3)2 loadings based on the PEO weight; the weight ratio of PEO: Zn(CF3SO3)2 is from 10:1 to 3:1. As we know, the Zn(CF3SO3)2 salt concentration has a profound effect on the physicochemical properties for polymer electrolyte*[123], [124]. *The inner resistance of the composite film decreased significantly by increasing the Zn(CF3SO3)2 loading and reached the plateau at 1:3 compared to PEO weight. The tensile strength, however, decreased when the salt loading increased further. Additional amount of Zn(CF3SO3)2 in PZB film changes the tensile strength from around 83±4.2 MPa to 7.8±0.40 MPa as the CF3SO3- ions tend to aggregate at high loading*[125], [126]. *Thereby, most of the studies below are carried out for composite electrolytes with weight ratio of Zn(CF3SO3)2 to PEO of 1:3 and BANFs 10 wt% of the total PEO weight. Henceforth, this composite electrolyte will be referred as PZB-931.*

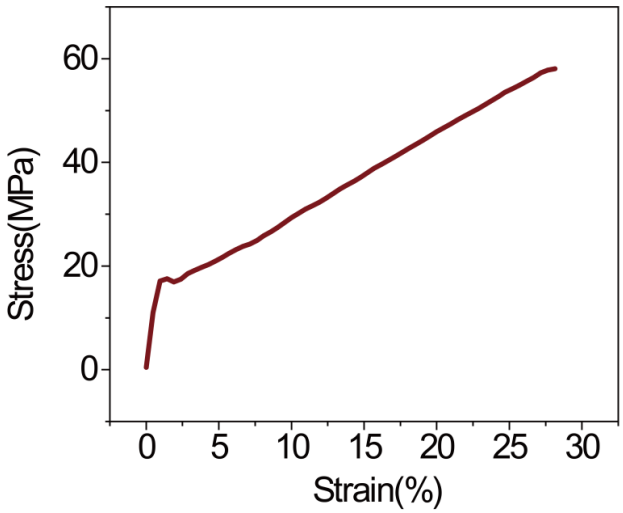

Figure S 2 *Stress/strain cure of the PZB-931 biomimetic composite.*

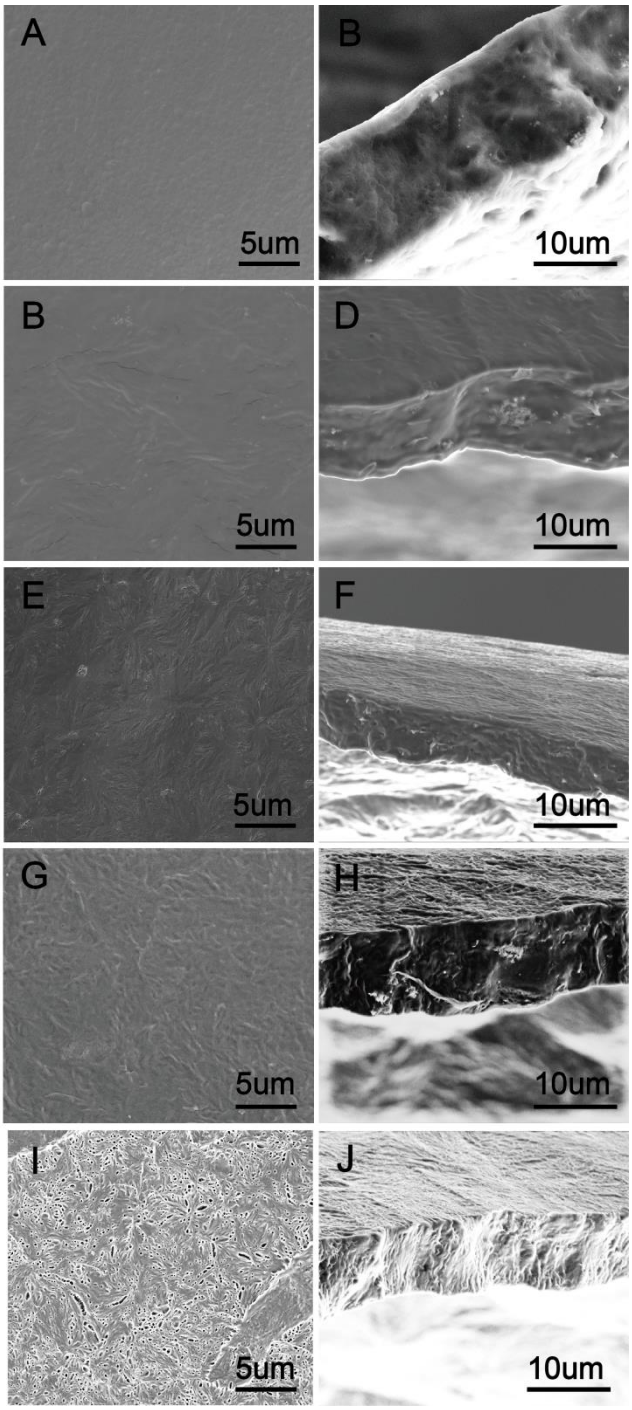

Figure S 3 *(A to J) The SEM images of the surface view and side view of PZB composites with different BANF loading. (A and B) neat PEO, (C and D), PZB composite with 1wt% BANF loading, (E and F), PZB composite with 5wt% BANF loading, (G and H) PZB composite with 10wt% BANF loading, and (I and J) PZB composite with 15wt% BANF loading. Here and elsewhere the nanofiber loading is reported in respect to the weight of PEO.*

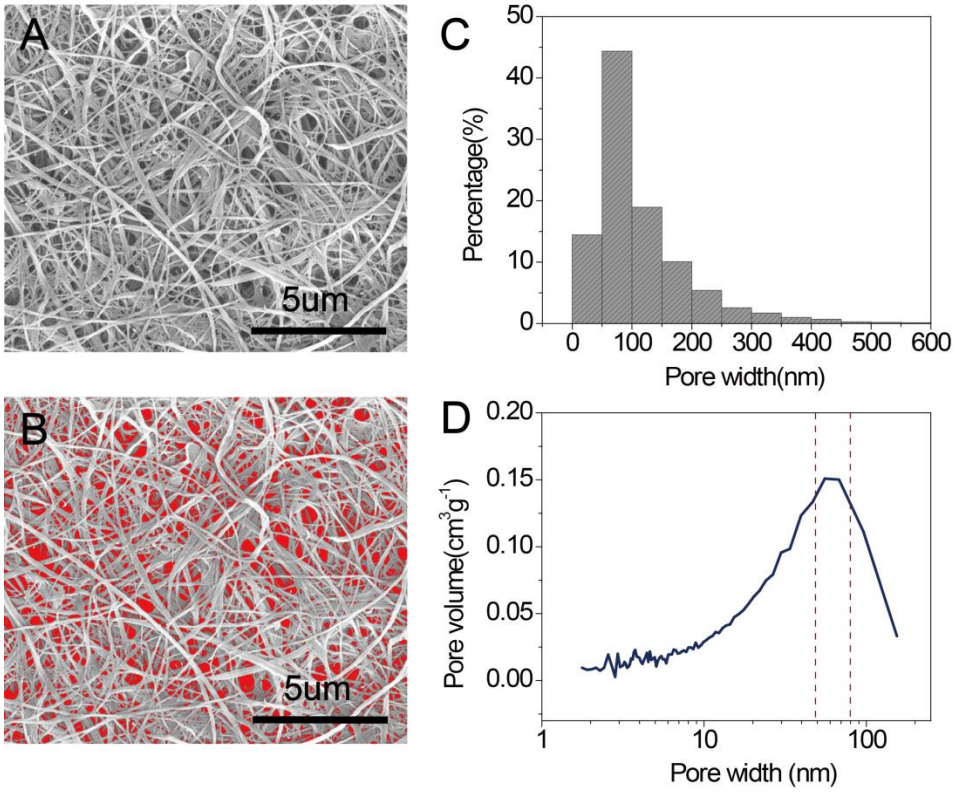

Figure S 4 *(**A** and **B**) SEM surface image of the BANFs and (**C**) Corresponding statistical analysis of the apparent pore sizes on the BANF surface in (B). (**D**) Pore size width distributions of the BANF obtained from Barrett-Joyner-Halenda (BJH) analysis.*

The nanoscale architechture of the BANF-based composites was investigated by SEM (**Figure S 4 A**). The pore size in PZB 931 was found to be from tens of nanometers to hundreds of nanometers (**Figure S 4 B, C**).

The pore size from the BJH analysis was calculated to be 50-70 nm. The apparent difference between the pore sizes calculated from SEM image and BJH data is common; it is associated with the changes occurring with the nanoporous materials under vacuum.

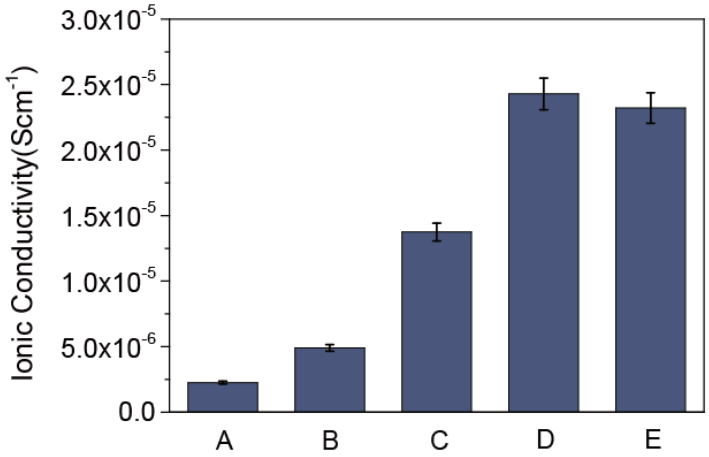

Figure S 5 *Ionic conductivities of PZB composite films with different of BANF loading. (**A**) PEO film, (**B**) PZB composite with 1wt% BANF loading, (**C**) PZB composite with 5wt% BANF loading, (**D**) PZB composite with 10wt% BANF loading, and (**E**) PZB composite with 15wt% BANF loading. Here and elsewhere the nanofiber loading is reported in respect to the weight of PEO.*

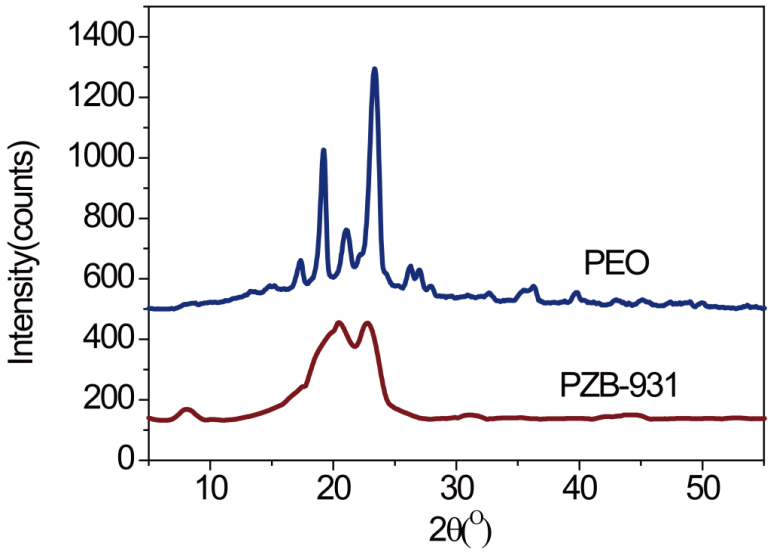

Figure S 6 *The XRD pattern comparison between PEO and PZB-931 composite film. The amorphous nature of PEO polymer was clearly observed in PZB-931 composite film by a diffuse broad band for 2θ between 20º and 30º instead of the sharp peaks at 2θ = 19º and 2θ = 23º for crystalline PEO.*

Comment: The intensity of the characteristic XRD peaks of crystalline PEO at 19 and 23 degrees are markedly decreased and experience strong broadening, indicating dominance of the amorphous PEO phase.

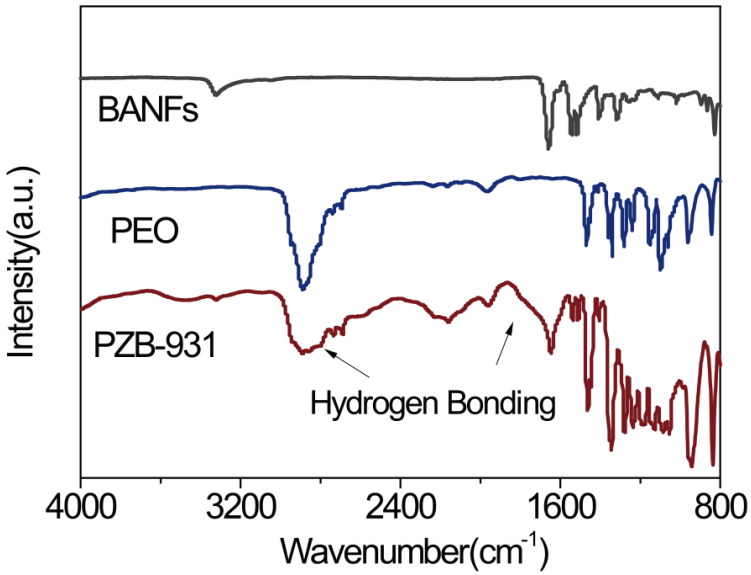

Figure S 7 *The FT-IR spectra of BANFs, PEO and PZB-931 composite. Two new peaks at 2798 cm–1 and 1770 cm–1 are found in PZB-931 composite and represent intermolecular hydrogen bonds between BANFs and PEO chains which hindering the crystallization of the polymer.*

Comment: The FT-IR spectrum of PZB-931 shows two new peaks at 2798 cm^{-1} and 1770 cm^{-1} ascribed to intermolecular hydrogen bonds between the BANFs and PEO chains that hinder the crystallization of the polymer [127].

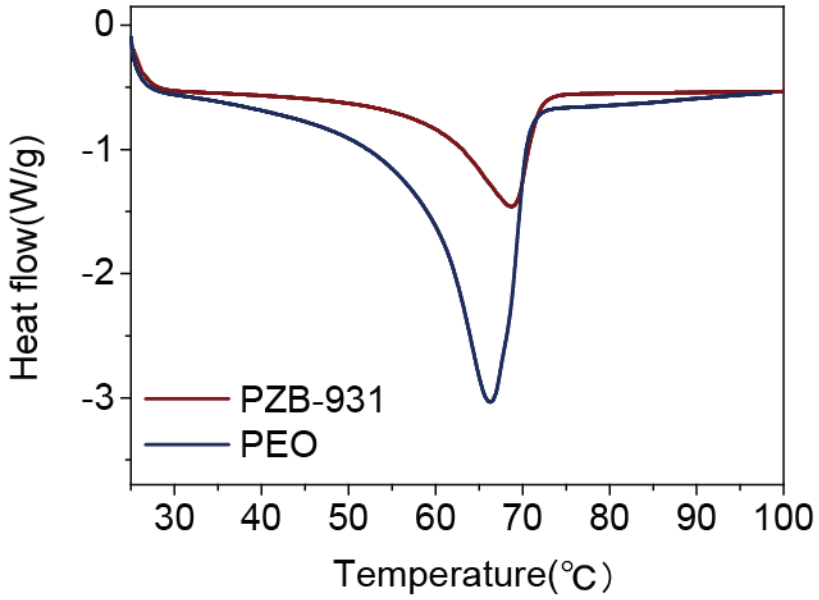

Figure S 8 *DSC curves for PZB-931 composites and ion-conducting membrane from neat PEO.*

Comment: DSC measurements show lack of crystallinity in PZB-931. Intensity of PEO peak decreases and melting temperature shifts as a result of BANF presence.

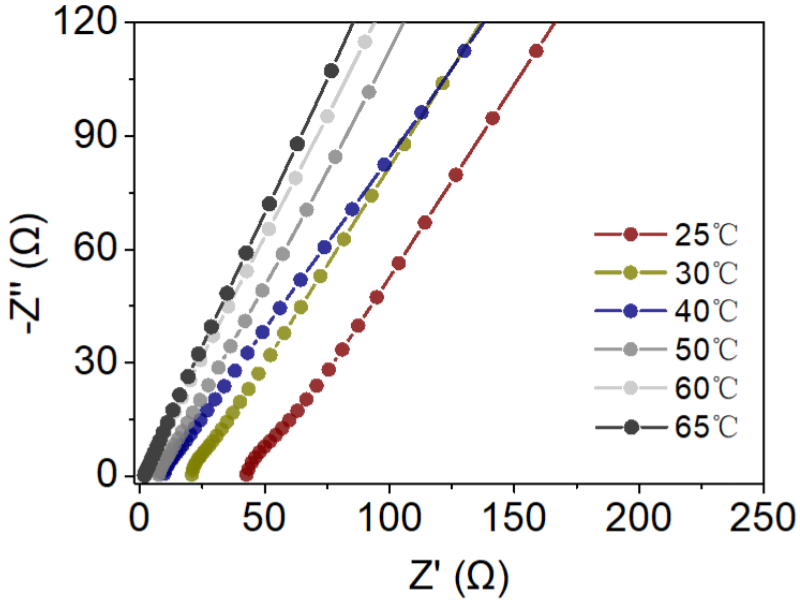

Figure S 9 *Comparison of the EIS curves obtained under different temperatures for PZB-931.*

Equation 2 *:The chemistry of zinc/PZB-931/γ-MnO_2 battery.*

Anode: $$Zn \rightarrow Zn^{2+} + 2e^{-}$$

Cathode: $$Zn^{2+} + 2e^{-} + 2\gamma MnO_2 \rightarrow ZnMn_2O_4$$

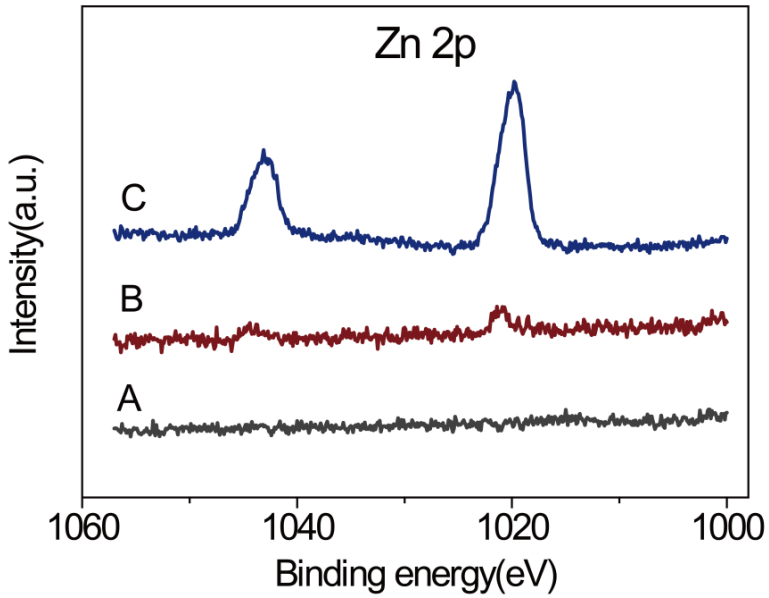

Figure S 10 *Zn 2p core level spectra of cathodic γ-MnO_2 electrodes at (**A**) original, (**B**) Zn-depleted and (**C**) Zn-rich states.*

Comment: An increase of the intensity of the Zn 2*p* signal (**Figure S 10**) from the Zn-rich state different to those of the other two states confirmed the insertion/extraction of Zn^{2+} ions into/from the γ-MnO_2 tunnels which matches the conclusions about reversible intercalation made on the basis of cyclic voltammetry CV scans[128], [129] displayed in **Figure 2.2B**. Large amounts of Zn^{2+} ions were also detected on the surface of the cathode material in the Zn-rich state, which were found to be absent in the Zn-depleted state.

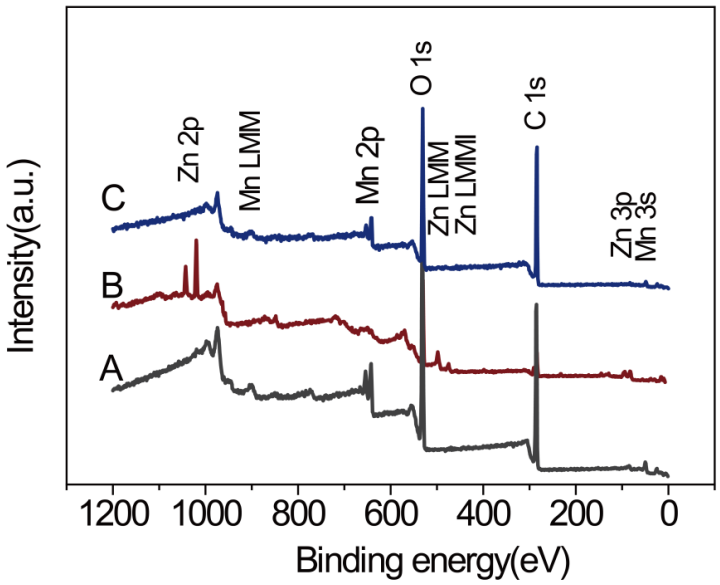

Figure S 11 *The XPS survey of cathodic γ-MnO_2 electrodes at (**A**) original, (**B**) Zn-rich and (**C**) Zn-depleted states.*

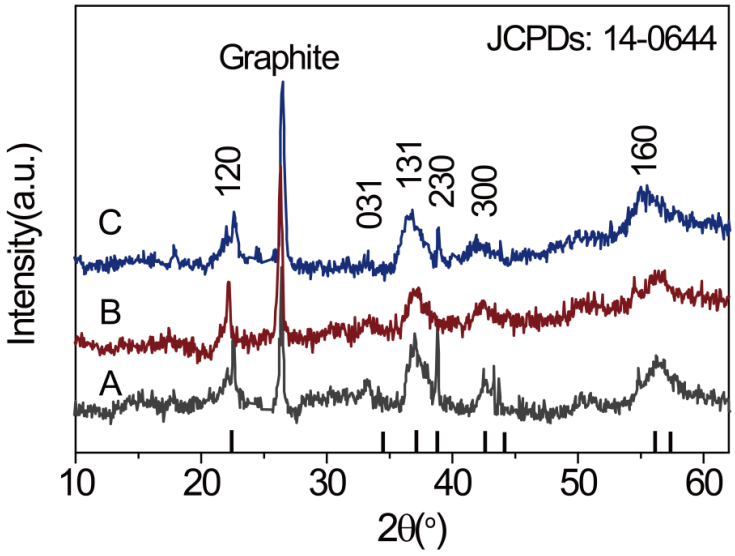

Figure S 12 *XRD patterns of cathodic γ-MnO2 electrodes in the (**A**) original, (**B**) Zn-rich and (**C**) Zn-depleted states.*

Comment: The XRD diffraction patterns of the cathodes in the original, Zn-rich, and Zn-depleted states were virtually identical and showed crystalline γ-MnO_2 exclusively. This finding is consistent with the original state, indicating that the Zn^{2+} ions reversibly intercalate into the framework during the charge and discharge processes.

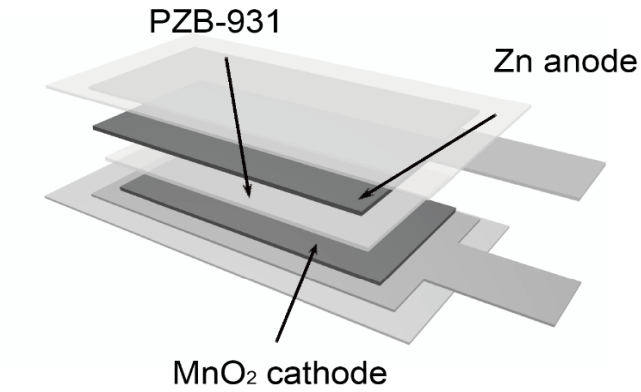

Figure S 13 *Schematic diagram of a flexible Zn/PZB-931/γ-MnO_2 battery.*

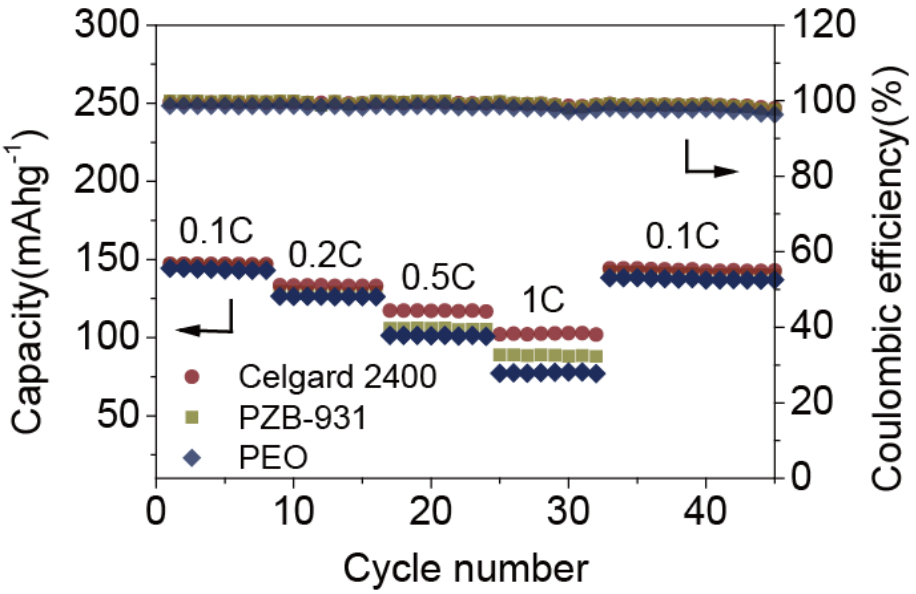

Figure S 14 *Rate performance of Zn/PZB-931/MnO_2 battery cells for charge-discharge rates from 0.1C to 1C . The data for analogous battery cells made with PEO as ion-conductor and Celgard 2400 with liquid electrolyte are provided for comparison.*

Figure S 15 *The voltage generated by Zn/PZB-931/γ-MnO_2 battery with different shapes. No short-circuits are observed after plastic deformation leading to corrugations.*

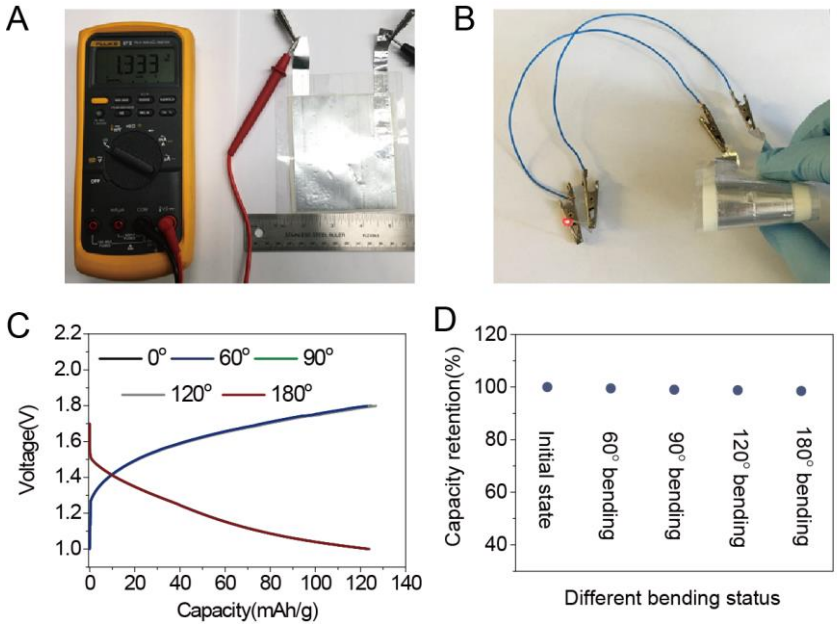

Figure S 16 *(A) The photographs of flexible Zn/PZB-931/γ-MnO_2 battery and (B) an LED lit by the flexible device. (C-D) Galvanostatically charged and discharged curves(C) and Capacity retention (D) of Zn/PZB-931/γ-MnO_2 at 0.2 C under different bending angles.*

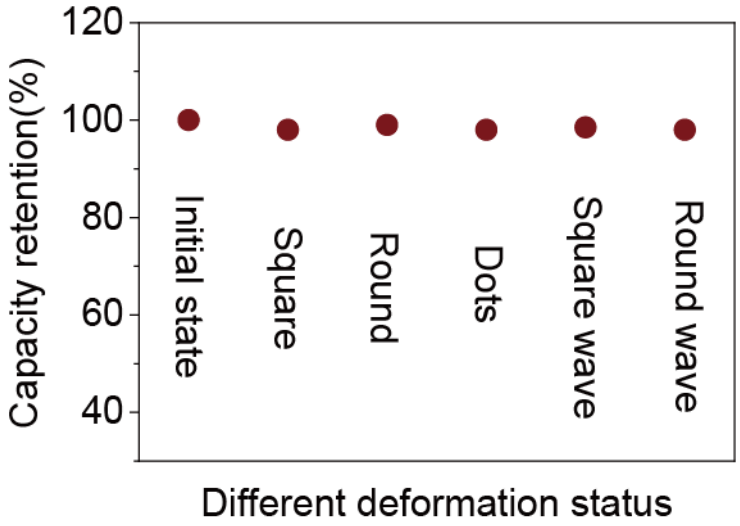

Figure S 17 *Capacity retention of the Zn/PZB-931/γ-MnO_2 battery under various deformation status corresponding to* ***Figure 2.4B-F****.*

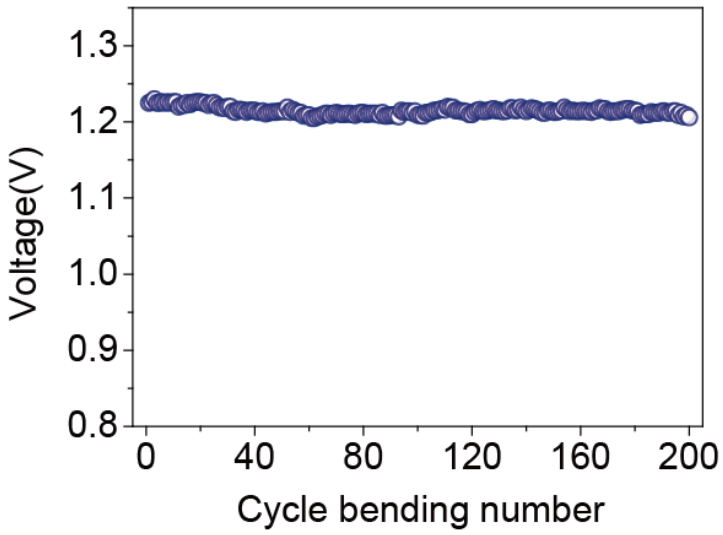

Figure S 18 *The open-circuit voltage of Zn/PZB-931/γ-MnO_2 battery undergoing bending tests at 5 bending cycles per second.*

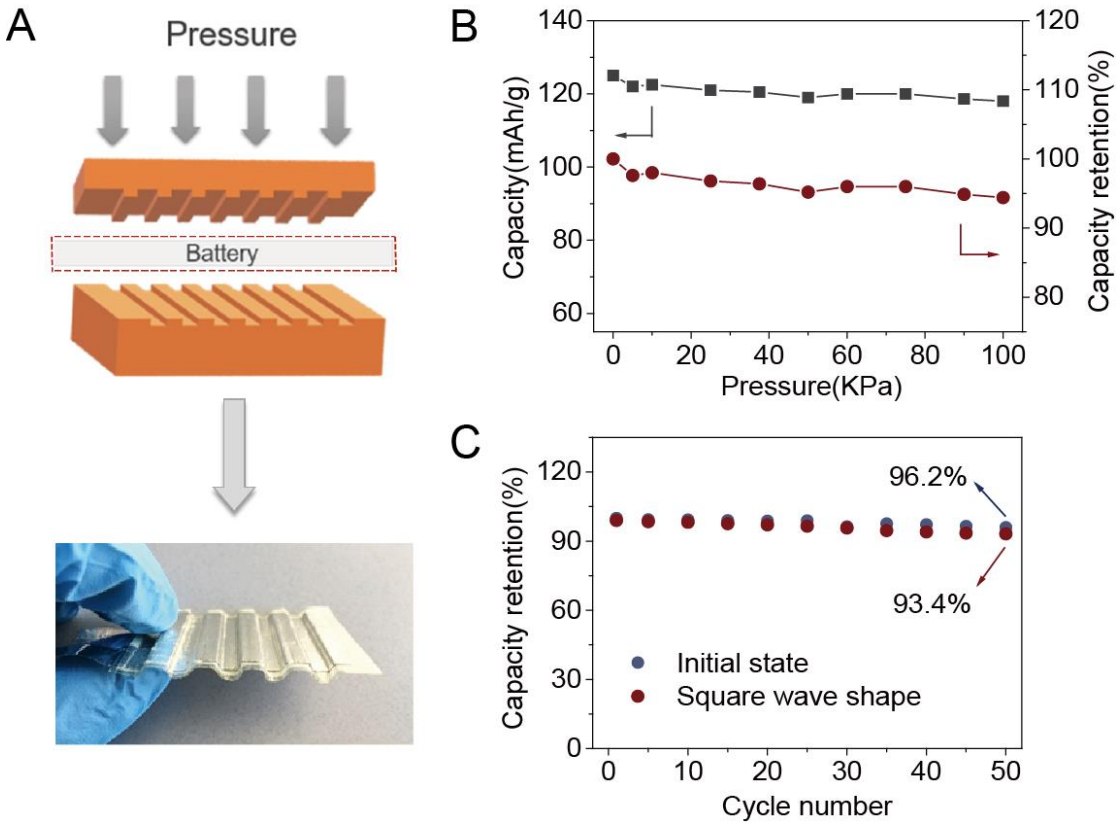

Figure S 19 *(A) Schematic diagram fabrication process of Zn/PZB-931/γ-MnO_2 structural batteries. (B) The capacity performance of Zn/PZB-931/γ-MnO_2 battery under different pressure. (C) Capacity retention of the structural battery on cycle numbers under square wave shape.*

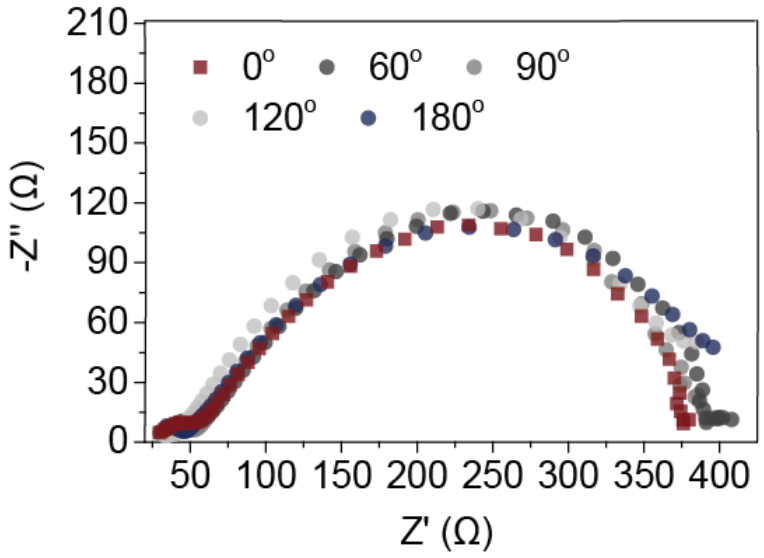

Figure S 20 *Comparison of the EIS of the Zn/PZB-931/γ-MnO_2 battery for different bending angles.*

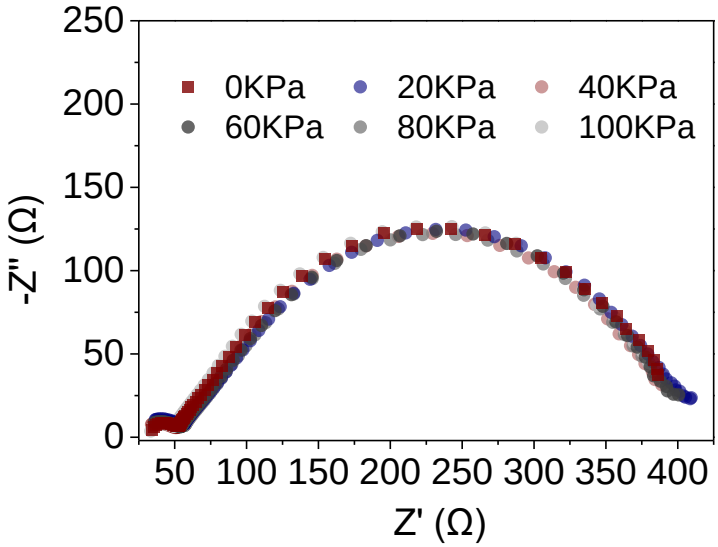

Figure S 21 *Comparison of the EIS of the Zn/PZB-931/γ-MnO_2 battery under different pressure.*

Table 1 *Comparison of electrolyte, capacity, and cyclic stability of flexible rechargeable batteries with zinc chemistries.*

Battery System	**Ion transport media**	**Conductive Ions**	**Capacity(mAhg-1)**	**Cyclic Stability**	**Ref**
Zn/air battery	Cellulose film	1mol/L KOH water solution	125mAhg-1	35 cycles	[79]
Zn/air battery	PVA gel film	KOH water solution	500mAhg-1	30 cylces	[130]
Zn/Co3O4 battery	PVA-PAA copolymer film	1mol/L KOH and 1.0x10-3mol/L Zn(Ac)2 water solution	160mAhg-1	2000 cycles 80% capacity retention	[68]
Zn/Ni battery	PVA gel film	2mol/L KOH water solution	265 mAh g-1	1000 cycles 91.4% capacity retention	[74]

Abbreviations: PVA: Polyvinyl alcohol; PAA: Polyacrylic acid; $Zn(Ac)_2$: Zinc acetate; KOH: Potassium hydroxide.

Table 2 *Comparison of electrolyte, capacity and cyclic stability of flexible lithium rechargeable batteries.*

Battery System	Sepatator Materials	Conductive Ions	Capacity(m Ahg^{-1})	Cyclic Stability	Ref
Li/CNT battery	Glass fiber film	1mol/L $LiPF_6$ in EC/DMC(w/w =1:1) solution	300 $mAhg^{-1}$	40 cycles	[131]
Li/graphene battery	Celgard 2340	1mol/L $LiPF_6$ in EC/DEC(v/v =1:1) solution	156 $mAhg^{-1}$	1000 cycles	[132]
Li/$LiMn_2O_4$ battery	Glass fibers film	1mol/L $LiClO_4$ in PC solution	80 $mAhg^{-1}$	50 cycles	[133]
Li/TiO_2 battery	Celgard 2400	1mol/L $LiPF_6$ in EC/DMC(v/v =1:1) solution	147 $mAhg^{-1}$	100 cycles with less than 2% capacity loss	[134]
Li/MnO_2 battery	Pore size alumina	1mol/L $LiPF_6$ in EC/DMC(w/w =3:7) solution	495 mA h g^{-1}	40 cycles	[135]
Li/Ag Graphene battery	Glass fibers film	1.5mol/L $LiPF_6$ in EC/EMC (w/w =3:7) solution	339 $mAhg^{-1}$	100 cycles	[136]
Li/SnO_2 Graphene battery	Celgard 2400	1mol/L $LiPF_6$ in EC/DMC(v/v =1:1) solution	625 $mAhg^{-1}$	100 cycles	[137]
Li/V_2O_5 battery	Celgard 2400	1mol/L $LiPF_6$ in EC/DEC(v/v =1:1) solution	94.4 $mAhg^{-1}$	100000 cycles	[138]
Li/S battery	Celgard 2500	1mol/L LiTFSI in DOL/DME(v/v =1:1) solution	740 $mAhg^{-1}$	160 cycles	[139]
Li/$LiCoO_2$ battery	Xerox paper	1mol/L $LiPF_6$ in EC/DEC(v/v =1:1) solution	147 $mAhg^{-1}$	300 cycles	[140]
Li/$LiFePO_4$ battery	Cellulose membrane	1mol/L $LiPF_6$ in EC: DEC (v/v =1:1) solution	145 $mAhg^{-1}$	50 cycles	[102], [141]
Li/$LiFePO_4$ battery	Cellulose membrane	1mol/L $LiPF_6$ in EC: DEC (w/w =1:1) solution	146 $mAhg^{-1}$	-	[142]

Abbreviations: $LiPF_6$: Lithium hexafluorophosphate; $LiClO_4$: Lithium perchlorate; LiTFSI: lithium bis(trifluoromethylsulfonyl)imide; EC: ethylene carbonate; DMC: dimethyl carbonate; DEC: diethyl carbonate; PC: propylene carbonate; EMC: ethyl methyl carbonate; DOL: 1,3-dioxolane; DME: 1,2-dimethoxy ethane

Table 3 *Comparison of tensile strength, tensile modulus, and elongation at break of PZB biomimetic composite with different BANF loadings.*

	Thickness (um)	Tensile strength (MPa)	Tensile modulus (MPa)	Elongation at break (%)
PEO	10±0.50	23±1.2	3.3±0.17	690±34
PZB (1wt% BANFs)	10±0.50	25±1.3	5.1±0.26	490±24
PZB (5wt % BANFs)	10±0.50	37±1.9	22±1.1	170±8.5
PZB (10wt % BANFs)	10±0.50	58±2.9	210±11	28±1.4
PZB (15wt % BANFs)	10±0.50	54±2.7	210±11	26±1.3

Table 4 *Comparison of the EIS of the PZB-931 under different temperature.*

Sample with different temperature (°C)	Resistance (Ohms)	Ionic conductivity (δ, Scm^{-1})
25°C	43.2	2.5×10^{-5}
30°C	21.2	5.1×10^{-5}
40°C	10.1	1.1×10^{-4}
50°C	7.8	1.4×10^{-4}
60°C	2.3	4.7×10^{-4}
65°C	1.9	5.7×10^{-4}

Table 5 *Comparison of electrolyte, capacity and cyclic stability of rechargeable batteries with zinc chemistries.*

Battery System	Conductive ion	Capacity($mAhg^{-1}$)	Cyclic Stability	Ref
Zn/α-MnO_2	2mol/L $ZnSO_4$ with mol/L $MnSO_4$ water solution	285$mAhg^{-1}$	5000 cycles 92% capacity retention	[64]
Zn/α-MnO_2	Gelatin and PAM gel separator	306 mAh g^{-1}	1000 cycles 97% capacity retention	[143]
Zn/α-MnO_2	1mol/L $Zn(NO_3)_2$	210 $mAhg^{-1}$,	100 cycles	[63]
Zn/β-MnO_2	3mol/L $Zn(CF_3SO_3)_2$ with/without 0.1 mol/L $Mn(CF_3SO_3)_2$	225 $mAhg^{-1}$	2000 cycles 94% capacity retention	[144]
Zn/$ZnMnO_2$	3mol/L $Zn(TFSI)_2$ water solution	150 $mAhg^{-1}$	500 cycles 94% capacity retention	[66]
Zn/ZnV_2O_5	1mol/L $ZnSO_4$ water solution	300 $mAhg^{-1}$	1000 cycles 80% capacity retention	[65]
Zn/V_2O_5	0.5mol/L $Zn(TFSI)_2$ water solution	170 $mAhg^{-1}$	120 cycles	[145]
Zn/VS_2	1mol/L $ZnSO_4$ water solution	195 $mAhg^{-1}$	200 cycles 98% capacity retention	[146]
Zn/Co_3O_4	KOH $Zn(Ac)_2$ water solution	135 $mAhg^{-1}$	2000 cycles 80% capacity retention	[68]

Table 6 *Summary of performance parameters for different kinds of structural batteries or supercapacitors.*

Category	Cathode material	Anode material	Separator/ electrolyte	Reported Capacity	Capacity retention	Specific power density	Flexibility	Ref
Pouch cell	$LiFePO_4$	Carbon fibers	Vinyl ester resins	--	--	--	N.A.	[147]
Pouch cell	$LiFePO_4$	Carbon fibers	Glass fiber	116.6m Ahg^{-1}	--	268.2 $Whkg^{-1}$	N.A.	[148]
Pouch cell	$LiCoO_4$	Carbon fibers	Poly(ethylene glycol)-methacrylate	90mAhg $^{-1}$	--	35Wh kg^{-1}	N.A.	[149], [150]
Pouch cell	$LiCoO_4$	Graphite	Polyolefin separator	--	--	95.2W hkg^{-1}	N. A	[151]
Pouch cell	$LiMn_2O_4$	Graphite	Celgard 2320	18.9AhL $^{-1}$	84.3% capacity retention after 50 cycles under mechanical test	223W hL^{-1},	Moderate	[152]
Pouch cell	Lithium Nickel-Cobalt-Manganese	Graphite	Polyolefin separator	--	96% capacity retention after 200 cycles under bending test	142W hkg^{-1}	N.A	[4], [153], [154]
Pouch cell	--	Carbon fibers	Poly(ethylene glycol) diglycidyl ether	--	--	10.54 mWhk g^{-1}	N.A	[118]
Cable-shaped cell	--	Nickel	Lead zirconate titanate	--	--	26.5m Jm^{-3}	Good	[155]

Chapter 3

Multifactorial Engineering of Biomimetic Membranes for Batteries with Multiple High-Performance Parameters

3.1 Abstract

Lithium-sulfur (Li-S) batteries have high specific capacity, but lithium polysulfide (LPS) diffusion and lithium dendrite growth drastically reduce their cycle life. Here we show that aramid nanofiber (*np-ANF*) membranes structurally similar to cartilage address both of these challenges due to targeted multifactorial engineering of mechanical, thermal, and ion-selective properties. ANFs with partially hydrolyzed surface support LPS adsorption creating a layer of negative charge on nanoscale pores blocking LPS transport. Numerical computation of ion transport in a nanochannel model with parameters matching experimental ones, demonstrates that ion-selectivity based on electrostatic repulsion effectively suppresses LPS diffusion while allowing Li^+ ions to be transported. High Young's modulus of *np-ANF* enables Li-S batteries with high capacity and sulfur loading because the composite membranes can be as thin as 5.8 μm. The relationship between Young's modulus and lithium dendrite suppression derived from the Newman-Monroe model shows that the high stiffness of the *np-ANF* membranes also leads to dendrite suppression. The *np-ANF* battery cells exhibited capacity of 1268 mAh g^{-1} closely approaching the theoretical high for Li-S batteries, up to 3500+cycle life and up to 3C discharge rates. High thermal stability of ANFs enables operation at temperatures up to 80^{o}C which is essential for Li-S battery safety. Multiparameter assessment using glyph plots and cumulative capability criterion (CCC) shows that across-the-board performance of Li-S batteries employing *np-ANF* exceeds the current state-

of-the-art. Simplicity of ANF synthesis, their self-assembly into composites, and experimentally verified ion-selectivity model open the door for engineering of high-performance nanofiber-based biomimetic materials for numerous energy technologies.

3.2 Introduction

High theoretical specific capacity of 1675 mAh g^{-1}, environmental friendliness, and earth-abundance of elements forming lithium-sulfur (Li-S) batteries make them an attractive platform for energy storage in a variety of technological fields from electric vehicles to robotics and from power grids to aerospace engineering [156]. However, the diffusion of lithium polysulfides (LPS, Li_2S_X, $4 \leq x \leq 8$) [157] from cathode to anode drastically reduces their cycle life, overall capacity, and Coulombic efficiency [158]–[161]. Additionally, LPS layers passivate both the electrodes, leading to a significant increase in impedance and thus to energy losses [162]. The non-uniform surface layer on anode also promotes the growth of dendrites, which represents another severe issue for Li-S batteries that causes similar issues compounded by short-circuiting and overheating.

Extensive research effort in the past was invested into designing materials for sulfur cathode that would minimize LPS release. It was shown that immobilization of LPS is possible by encapsulating sulfur into microporous carriers [163], [164] made from nanocarbons [156], [165], [166], conductive polymers [167], [168], transition metal oxides [169]–[171], and metal-organic frameworks [172], [173]. Indeed, nanoporous barriers in the cathode improved the retention of sulfur within the cathode. However, there is still considerable room for improvement in the cycle life and overall performance of Li-S batteries [174], [175] addressing the structural complexity of cathode material, and improving electron transport through electrode material [176], [177].

The problem of the LPS diffusion can also be approached by optimizing the materials design of ion-conducting membranes that can block the LPS transport from S cathode to Li anode.

Simultaneously, these membranes must allow the facile transport of Li^+ ions [175], [178]–[181]. Significant advances in this area were achieved using coatings from carbonaceous materials [178], [179], [182]–[184], polymers [183], [185], [186], metal foams [187], metal-oxide layers [183], [188], [189], and metal oxides with carbon [190], [191]. The great challenge for all of these structural solutions for LPS membranes is to combine at least two contrarian materials properties – efficient ion transport and mechanical robustness in one material or a coating.[162], [183], [192]–[194] Among the latter, polymers with high shear modulus are necessary to suppress dendrite growth on lithium anodes [195] while high strength, thermal stability, and toughness are essential for the longevity of the batteries in real-world conditions, for instance in electric vehicles. The prior experimental and computational data show this materials engineering task is difficult [162], [183], [192]–[194], [196] and requires a new approach in materials design.

Here, we show that the ion-selective membranes engineered using sequential deposition of nanofibers enable nearly complete prevention of the LPS diffusion from cathode to anode. The structural design for this membrane was inspired by cartilage known for efficient ion transport combined with high ion selectivity [197] as well as unique mechanical properties [198]. The design of these tissues is based on highly interconnected nanofiber networks, which can be replicated in composites made from on nanoporous aramid nanofibers (np-ANFs). The direct analogy between organization of nanofibers in ANF membranes and cartilage was recently demonstrated by evaluation of their connectivity using Graph Theory[47]. Importantly, these composites can be engineered into stratified membranes with nanoscale porosity (*np-ANF*) and charge sieving capabilities due to the spontaneous adsorption of LPS layer on *np-ANF* surface. Numerical simulations by finite element analysis confirm that negatively charged 1nm pore of *np-ANF* found experimentally inhibits LPS shuttling while affording rapid transport of Li^+ ions.

Considering the challenges for battery separators described above, ANFs are known for their mechanical and thermal properties. They display Young's modulus of $E = 9.2 \pm 0.5$GPa (55 times higher than *Celgard*^{TM} 2400) and high thermal resistance (600°C). These properties make possible simultaneous suppression of lithium dendrites extending the life cycle of the Li-S batteries to 3500+ cycles at 3C. The combination of properties found in *np-ANF* resulted in high efficiency of LPS blocking and remarkable stability over long-term cycling even for high-temperature environments.

3.3 Results

3.3.1 Characterization of the np-ANF membrane

A method of spin-assisted layering assembly [199]–[201] modified from the original protocol and conceptually similar layer-by-layer (LBL) deposition [202]–[205] was used to fabricate membranes from ANF dispersions [206], [207] (See Methods). Using this technique, the thickness of membrane can be easily varied by increasing or decreasing the number of deposition cycles (**Figure S 22**), which is required for optimization of flux and selectivity of the ion-transporting membranes. By repeating the spin deposition cycle three times, we obtained ANF composite membranes with a smooth surface (**Figure 3.1 B-C**, **Figure S 22**) and a thickness of 5.8±0.50 µm (**Figure S 22D**), which is much about four times thinner than that of *Celgard*^{TM} 2400 membrane s with a typical thickness of 25µm. Reduction of the membrane thickness represents an important technological target because it enables increasing the thickness of active materials on both cathode and anode, increasing the overall battery capacity. The thickness of the state-of-the-art ion-conducting membranes for Li-S batteries is between 20 and 30 µm. (**Table 11**-**Table 14**). Thermogravimetric analysis (TGA) on *np-ANF* membrane indicates that no significant weight loss occurs below 600 °C in N_2 atmosphere (**Figure 3.1 D**), and the differential scanning calorimetry

(DSC) analysis on *np-ANF* confirms no significant change occurring with *np-ANF* until 500°C (**Figure S 23** and **Figure S 24**). Moreover, the *np-ANF* electrolyte wettable, which reduces internal resistance needed to achieve superior rate charge-discharge rate (**Figure S 25**).

The dense network of nanofibers in the *np-ANF* results in the formation of nanoscale pores 0.9 nm-1.2 nm in diameter (**Figure S 26**) as determined by the Barrett-Joyner-Halenda (BJH) analysis (**Figure S 27**), which is smaller than the hydrodynamic diameter of L_2S_4 of 1.3-1.5 nm [157], [208]–[211]. These pores are at least one order of magnitude smaller than those found in *Celgard*^{TM} 2400 where the BJH pore size exceeds 25 nm (**Figure S 28**).

3.3.2 Synergistic Effects of Negative Charge and Narrow Pore Size of np-ANF

The pore diameter in the range of single nanometers has two essential benefits for battery membranes related to the dendrite suppression and ion transport [211]. First, lithium dendrites have a diameter of around 300 nm in growth point (**Figure 3.1 E-F**). Providing sufficient mechanical properties [195], [212], membranes with single nanometer pore size can suppress the growth dendrites more efficiently than those with wider channels. Notably the Young's modulus of *np-ANF* -based membranes of E = 9.2 ± 0.5 GPa is higher than most of previously reported membranes (**Figure S 29** - **Figure S 30** and **Table 8**). Compared with *Celgard*^{TM} 2400 with E = 0.17 ± 0.02 GPa, it corresponds to *ca* 55x improvement in the Young's modulus (**Figure 3.1 G** and **Table 7**). The simple mathematical derivation relating the shear modulus, $G_{polymer}$, of the polymeric electrolyte and its Young's modulus, $E_{polymer}$, strictly following the Monroe and Newman model [195] shows that the original expression for the mechanical properties of ion-conducting membranes $G_{polymer}/G_{Li}$ = 1.65 can be converted into $E_{polymer}/E_{Li}$ = 1.53 (Supplementary Information). The advantage of the dendrite suppression relationship based on Young's moduli is that it is more practical because the values of Young's moduli are easier to

measure and are available for larger number of composite and other materials. Note that this conversion does not make any additional assumptions besides those made in the Monroe and Newman model or currently used in the field (Supplementary Information).

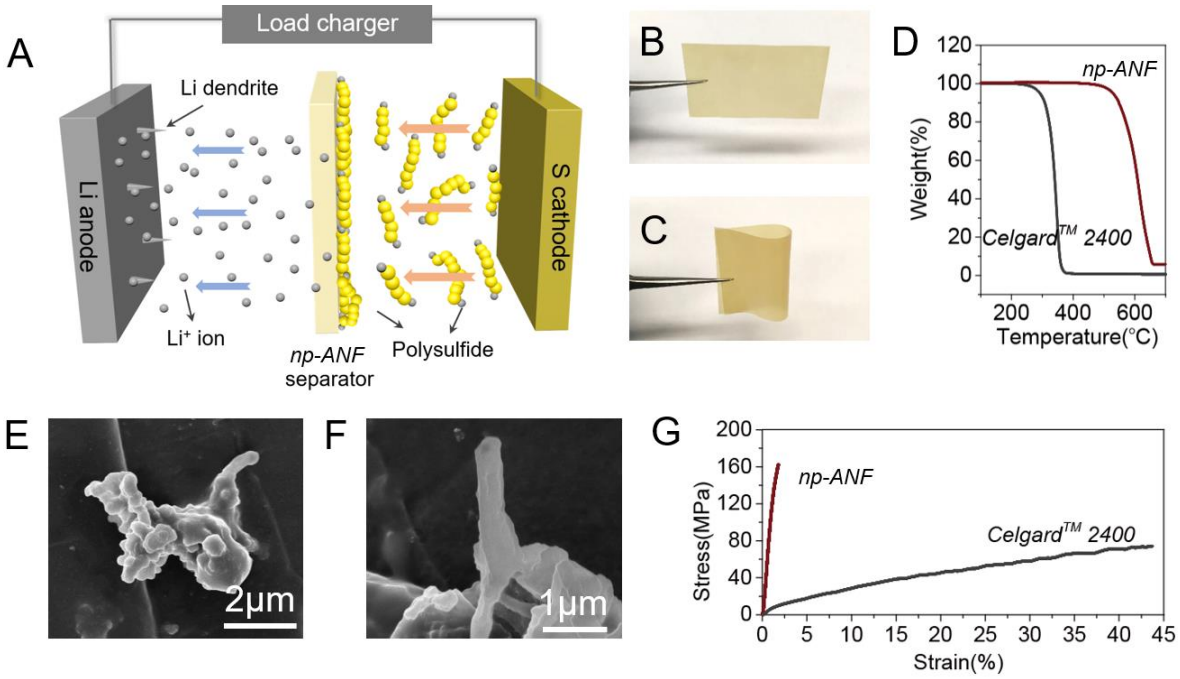

Figure 3.1 *Characterization of the np-ANF membrane (**A**). Schematic configuration of a Li-S cell with a np-ANF membrane between the sulfur cathode and the lithium anode. (**B** and **C**) Photographs of an np-ANF membrane. (**D**) thermogravimetric analysis curves for np-ANF membrane and Celgard™ 2400. (**E** and **F**) SEM images of the tip of lithium dendrite. (**G**) Stress-strain curves for np-ANF and Celgard™ 2400.*

Secondly, the negative surface potential of *np-ANF* [20], [25], [45] and the small diameter of the pores make the double electric layers extending from the pore walls overlap incompletely compensating the surface charge [213]–[215]. Being immersed in electrolytes typical for lithium batteries, such membranes reject negatively charged chains of LPS due to the repulsion from the channel walls. The nanoscale confinement enables, therefore, high degree of selectivity for the transport of ions through them re-creating the functional analogs of ion channels known from biology [216], [217].

We found that LPS can spontaneously bind to *np-ANF* creating the layer of strongly bound negative charge on them, which rejects transport of LPS but facilitates the transport of lithium ions. *np-ANF* membrane was immersed into 0.5 M Li_2S_4 in DOL/DME 10 hours at room temperature (25℃). After repeated 5 times wash in copious amount of DOL/DME solvent a large amount of sulfur was still detected on the surface of the membrane by the XPS analysis (**Figure 3.2 A** and **Figure S 31**), indicating the strong adsorption of polysulfides on *np-ANF*. This LPS adsorption on the *np-ANF* membranes was confirmed by EDAX and the Raman scattering (**Figure 3.2 B-C**). The two characteristic Raman scattering peaks of LPS observed in freely dissolved state at 450 and 520 cm^{-1} are broadened and appear at 400 and 440 cm^{-1} when adsorbed on *np-ANF*. Broadening is expected for adsorbed LPS due to multiplicity of the conformational states of LPS on *np-ANF* composite.

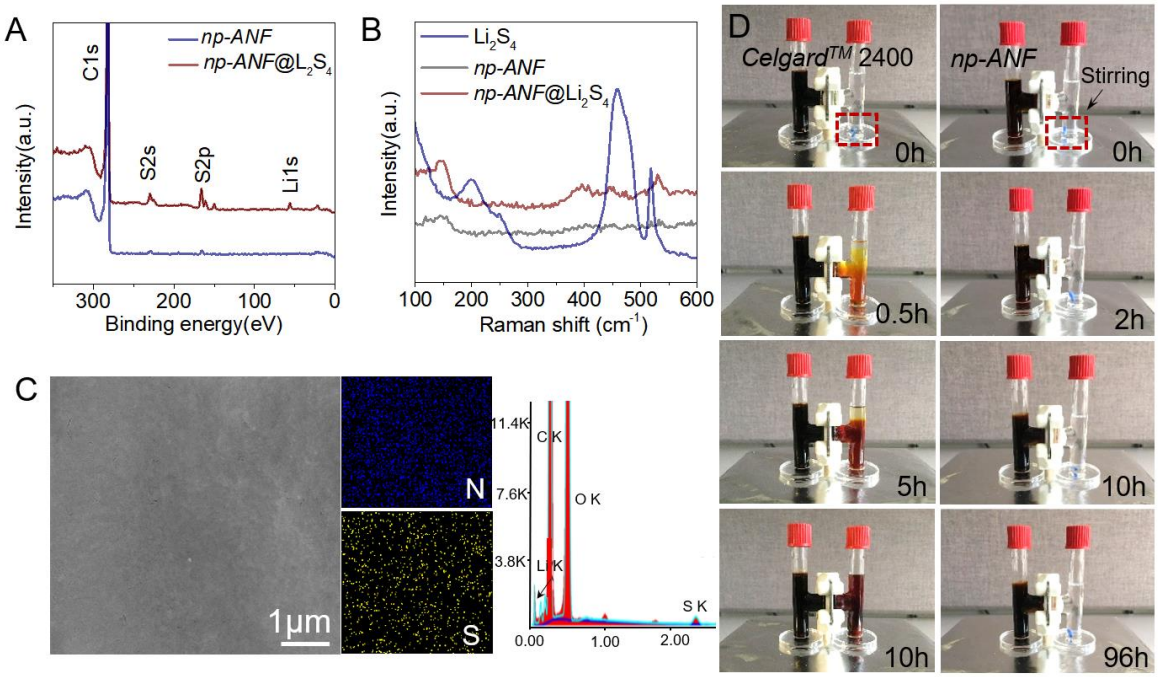

Figure 3.2 *Polysulfide-Blocking Capability of the np-ANF Separator* ***(A-C)****. XPS survey (****A****); Raman scattering spectra (****B****); SEM image, EDAX spectra and the corresponding N and S element mapping images (****C****) for the np-ANF before and after adsorption test* Li_2S_4 *solution followed by rinsing with DOL/DME solution and drying in glovebox.* ***(D).*** *Diffusion of LPS in H-type cell through Celgard™ 2400 and np-ANF membrane.*

np-ANF composites with negative charges on cylindrical pores [20], [25] are expected to be permeable for lithium ions but reject LPS (**Figure 3.2 D**) [218], [219] due to their negative charge, large size, and cooperative binding to the channel walls. Permeation behavior of LPS through the *np-ANF* membrane was investigated in an H-cell (**Figure 3.2 D**) filled with 1,3-dioxolane (DOL) and dimethoxyethane (DME) in 1/1 v/v ratio that is commonly used in the Li-S batteries [220]. DOL/DME solvent without LPS was placed in the right chamber while solvent with 0.5 M Li_2S_4 was in the left chamber. Driven by the concentration gradient, LPS easily diffused across the *Celgard*^{TM} 2400 and the right chamber turned from colorless to dark brown within 10 hours. In contrast, the diffusion of LPS was blocked by *np-ANF* membrane (**Figure 3.2 D**) and right chamber stayed colorless after 96 h even under a strong stirring.

We further investigated LPS blocking mechanism with numerical simulation of ion transport by finite element computations. The structure of the nanopore of ANF separator was modeled as a single 10 nm long channel with 1 nm diameter connecting two reservoirs (inset, **Figure 3.3A**). The diameter of the model channel has been determined by experimental pore size measured by the Barrett-Joyner-Halenda analysis **(Figure. S6)**. Both the reservoirs and nanochannel are represented by dielectric blocks with the electrolyte. The limitation caused by size of reservoirs of model are compensated by inflow boundary setting of anion and cation (**Figure 3.3 B)**. The anode and cathode with potential difference of 2 V had been set at the two ends of reservoirs for common electrostatic boundary condition of the models while surface charged density of -8 mC/m^2 has been selectively applied to the boundary of *np-ANF* separator for comparison. At initial, reservoir on cathode side (reservoir 1, **Figure 3.3 B**) is only filled with LPS anions (concentration of LPS-, c_{LPS} = 1M), whereas the whole system including nanochannel is uniformly filled with lithium cation (concentration of Li+, c_{Li+} = 1M). Two different electrostatic

conditions, with and without surface charge density on the surface of *np-ANF* membrane, were applied to the model and time-dependent studies were performed by solving the coupled Poisson, Nernst-Planck and Navier-Stokes equations. As expected, both LPS anion and Li cation can freely pass through the nanochannel that does not have surface charge (**Figure 3.3 C and D**, **I,** Movie S1- 2). When the model includes, however, the negative surface charge on the channel walls, the transport of LPS including some of the smallest LPS species, such as including Li_2S_4, is blocked (**Figure 3.3 D**, **ii**, Movie S4). Li^+ cations still pass though unimpeded (**Figure 3.3 C, ii**, Movie S3). Note that until 200 ns, some adsorption of Li cation layer on the wall of *np-ANF* has been observed although it does not block the passage of ion transport. Thus, the computational model demonstrates that *np-ANF* can selectively block LPS transport solely due to electrostatic repulsion, even excluding the size selectivity effect, which simplifies the engineering of the membranes for a variety of technologies.

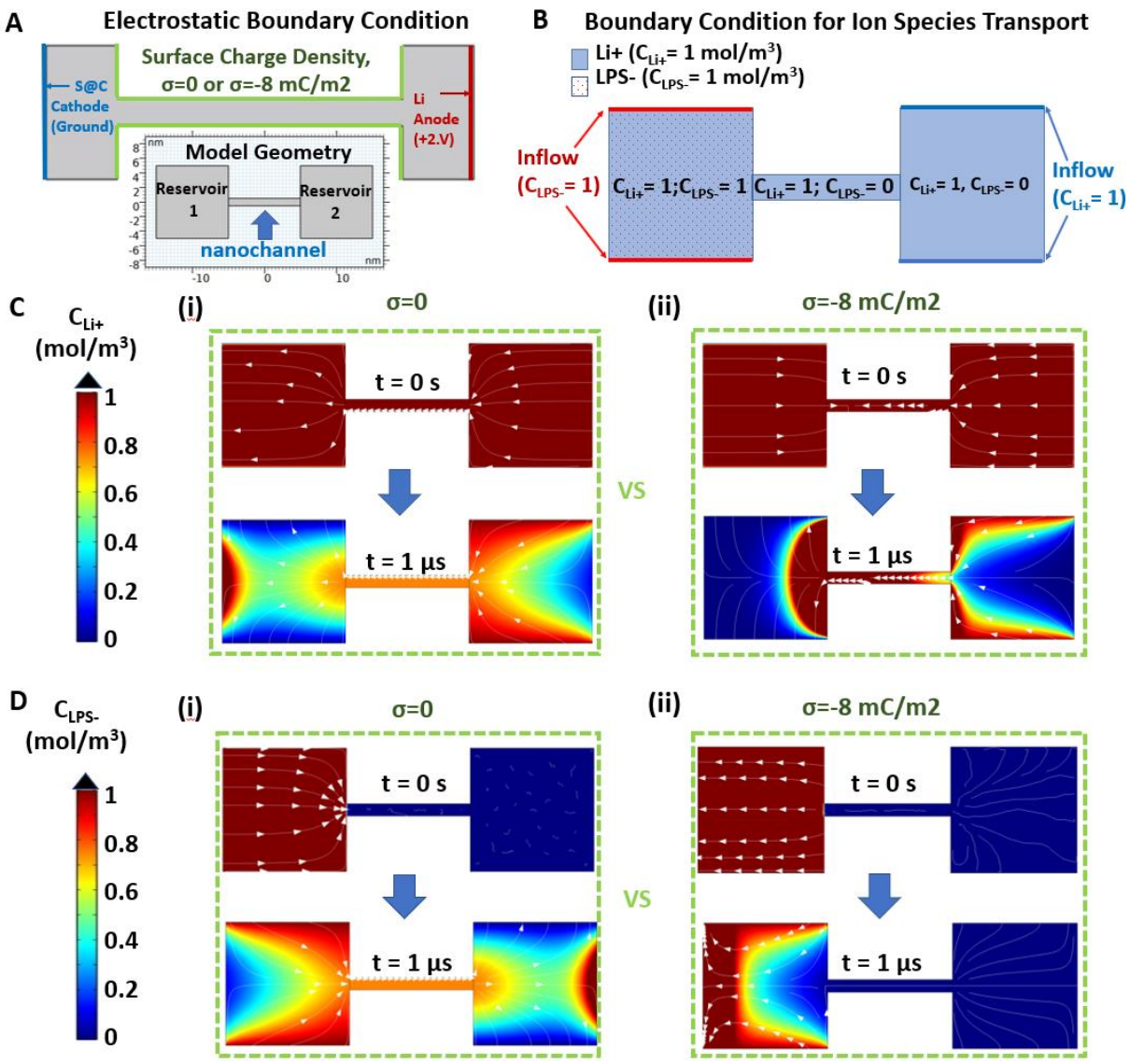

Figure 3.3 *Computational analysis on transport of charged ion species through a single nanochannel.* ***(A)*** *Electrostatic boundary condition including potential set for cathode (2V at S@C, conventional sulfur in carbon) and anode (ground at Li, Lithium metal), and surface charged density (σ) on ANF wall. (**B**) Boundary condition for ion transport module for LPS anion and Li cation. The concentration map and streamline change (from t = 0 to t = 1 µs) of Li cation (**C**) and LPS anion (**D**) with (**i**) and without (**ii**) surface charge density on boundary of np-ANF separator.*

3.3.3 Performance of the as Assembled Li-S Batteries at Room Temperature with High Sulfur Loading

In the cyclic voltammograms (CV) of Li-S battery cell with *np-ANF* membranes, two distinctive reduction peaks and a strong oxidation peak appear at 2.36, 2.02 and 2.31 V, respectively **(Figure 3.4 A**). For simplicity of notations the anodic peak and the two cathodic peaks

will be denoted here as peaks α, β, and γ, respectively. The peak γ at 2.36 V is attributed to the reduction of S_8 to intermediate LPS (Li_2Sx, $4 \leq x \leq 8$), while the second reduction peak β at 2.02V is ascribed to the further reduction of intermediate LPS to insoluble Li_2S and Li_2S_2. The strong oxidation peak α centered at 2.31 V corresponds to the delithiation of Li_2S/Li_2S_2 into Li_2Sx ($4 \leq x \leq 8$) and eventually to S_8 [162]. In the subsequent cycles, the intensities of reduction and oxidation peaks remain almost unchanged.

Using the classical Randles-Sevick equation [158], [221], [222], one can understand further Li^+ ion diffusion properties, acquiring CV curves under different scanning rates ranging from 0.1 to 0.5mVs^{-1} . The diffusion coefficients were determined to be $D_{Li+}(\alpha_1) = 9.263 \cdot 10^{-8}$ cm^2s^{-1}, $D_{Li+}(\beta_1) = 5.310 \cdot 10^{-8}$ cm^2s^{-1}, and $D_{Li+}(\gamma_1) = 0.421 \cdot 10^{-8}$ cm^2s^{-1} for *np-ANF*, which almost equal to the diffusion coefficients for the *Celgard*^{TM} 2400 of $D_{Li+}(\alpha_2) = 9.693 \cdot 10^{-8}$ cm^2s^{-1} , $D_{Li+}(\beta_2) = 5.192 \cdot 10^{-8}$ cm^2 s^{-1} , and $D_{Li+}(\gamma_2) = 0.567 \cdot 10^{-8}$ cm^2 s^{-1}, respectively (**Figure S 32** and **Table 9**). The lithium-ion transference number (t_{Li+}) of *np-ANF* separator (0.63) is almost similar to that pure *Celgard*^{TM} *2400* (0.68) (**Figure S 33** and **Table 9**). These data indicate that *np-ANF* does not affect the diffusion properties of Li^+.

Diffusion of LPS through membranes is detrimental effects for Coulombic efficiency of Li-S batteries even for low charge/discharge rate of 0.1 C. Coulombic efficiency is less than 70-90% for common Li-S batteries. Coulombic efficiency of the cells being cycled at 0.1 C for 300 cycles as 98% and 75% after for *np-ANF* and *Celgard*^{TM} 2400, respectively **(Figure 3.4 B)**. Besides Coulombic efficiency, the discharge capacity also increased accordingly because the *np-ANF* membranes hindered the chemical reactions between metallic lithium and high-order LPS, reducing the loss of active material loss. For example, the initial discharge capacity of 1268 mAh g^{-1} obtained on the cell with an *np-ANF* was higher than that for *Celgard*^{TM} 2400 with 1029 $mAhg^{-}$

[1] (**Figure 3.4 C**). Furthermore, the capacity decay rate was also reduced from 0.20% of *Celgard*^{TM} 2400 membrane to 0.092% per cycle. Comparing to other membranes designed for Li-S batteries, *np-ANF* membranes have an advantage because they improve the cycle life for long term at different charge/discharge rate (**Table 11**). When needed, the cycle life as well as the Coulombic efficiency could be further enhanced by increasing the thickness of *np-ANF*. However, it will increase the diffusion path length and internal resistance (**Figure S 34**) [223], [224] with concomitant reduction of capacity. One can expect that various energy consumption patterns will impose different preferences to Li-S battery operations. The ability of *np-ANF* to address different requirements will be essential for the future multiparameter performance optimization of charge storage devices.

Electrochemical impedance spectroscopy (EIS) of the Li-S cells were interpreted using equivalent circuits in **Figure S 35**. Batteries with *np-ANF* membranes showed a larger resistance compared to *Celgard*^{TM} 2400 prior to cycling (**Figure S 35A**), which is expected considering the reduced pore size in these ion-conductive membranes. However, after 100 cycles (**Figure S 35B**), the R_{ct} value of the cell with *np-ANF* significantly decreases, which may be resulted from infiltrating of the electrolyte and the chemical activation of the active materials [225], [226]. For comparison, the battery with *Celgard*^{TM} 2400 after 100 cycles shows two semicircles (**Figure S 35B**). The semicircle in high frequency (R_{sf}//CPE_{sf}) is related to formation of an insulating layer of solid Li_2S_2/Li_2S on lithium anode [227] and the second semicircle in low frequency (R_{ct}//CPE_{ct}) is assigned to the charge transfer resistance. On the contrary, the batteries with *np-ANF* membrane s possess only one semicircle in the high-frequency region (red curve in **Figure S 35** and **Table 10**). Furthermore, the corresponding R_{ct} value is lower for *np-ANF* than for *Celgard*^{TM} 2400, which

indicates faster reaction kinetics due to the formation of the SEI film on the electrode's surface making the Li ions transport easier [181], [228].

Although the transport of LPS is blocked, Li^+ ion transport through *np-ANF* is not and, in fact, remains fast. Li^+ ion conductivity is as high as 0.24 mS/cm due to the low internal resistance and favorable electrolyte wettability (**Figure S 25**), which translates into excellent rate performance of Li-S cell when ion-selective when *np-ANF* is used as ion conductor **(Figure 3.4 D** and **Figure S 36**). With the current densities varied between 0.1 and 3.0 C, discharge capacities of 1268, 1092, 969, 825, 703 and 521 $mAhg^{-1}$ were observed. When the charge/discharge rate was reduced back to 0.1C, a capacity of 1224 $mAhg^{-1}$ close to the original one was recovered for the cell with *np-ANF* whereas 931 $mAhg^{-1}$ was observed for the cell with *Celgard*^{TM} 2400 membrane. The batteries utilizing np-*ANF* membranes display a cycle life over 3500 cycles at 3C **(Figure 3.4 E)** with a capacity decay as low as 0.01% per cycle **(Figure 3.4 F**). Compared to many other ion-conductive membranes used for Li-S batteries, including carbon interlayers that serve mainly as physical barriers, *np-ANF* is more efficient in long-term inhibition of LPS diffusion (**Figure S 37** and **Table 11**).

Moreover, to evaluate the feasibility of the *np-ANF* separator in electrical vehicles and similarly demanding applications, the sulfur loading was increased to 3.6 and 5.8 mg cm^{-2}. The batteries were still able to deliver a high initial capacities of 1142 mA h g^{-1} (3.6 mg cm^{-2}) and 1018 mA h g^{-1} (5.8 mg cm^{-2}) (**Figure 3.4 G**) with the corresponding areal capacities of 4.1 and 5.9 mAh cm^{-2} . Based on the charge/ discharge curves (**Figure S 38A**), no polarization increase upon higher sulfur loading was observed. We also tested the cells with high sulfur loading for various current rates from 0.1C to 3.0 C (**Figure S 38B**). A high discharge capacity of 558 mA h g^{-1} at 3.0C was attained. Similarly to the case of 1.2 mg cm^{-2} sulfur loading, switching the charge-

discharge current back recovers the capacity of the battery to 940 mAh g^{-1} even when the sulfur loading as high as 5.8 mg cm^{-2} due to effective mitigation of LPS transfer from cathode to anode. Long-term cycling for 500 cycles (initial capacity 945 mAh g^{-1}, 5.5 mAh cm^{-2} at 0.2C) is also possible for high-sulfur cathodes (**Figure 3.4 H**); their capacity is competitive or better than most Li–S cells with sulfur loading ≥3.0 mg cm^{-2} (**Table 12**).

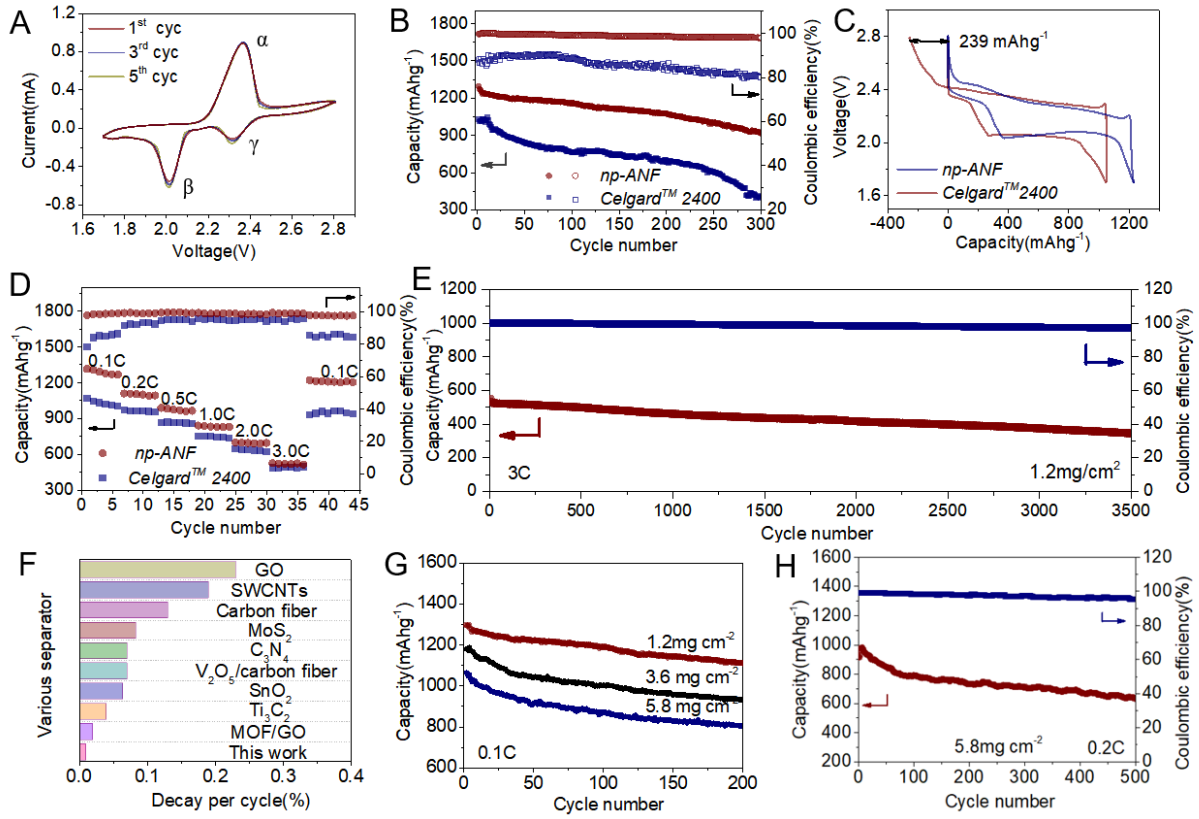

Figure 3.4 *Electrochemical performance of the Li-S batteries with np-ANF and Celgard™ 2400 membrane. (A) CV profiles with np-ANF at a scan rate of 0.1mVs^{-1}; (B) Cycling performance comparison of Li-S batteries with np-ANF and Celgard™ 2400 membrane at a rate of 0.1C;* ***(C)*** *Galvanostatic charge-discharge profiles of np-ANF and Celgard™ 2400 membrane at a rate of 0.1C; .****(D)*** *Rate performance of Li-S batteries ranged 0.1C to 3C with np-ANF and its comparison of Celgard™ 2400;* ***(E)*** *Cycling performance Li-S batteries with np-ANF membrane at a rate of 3 C over a period of 3500 cycles.* ***(F)*** *The decay per cycle of Li-S batteries with various membrane (GO*[218] *SWCNTs*[229] *Carbon fiber*[182] *MoS_2*[223] *C_3N_4*[230] *V_2O_5/ carbon fiber*[231] *SnO_2*[232] *Ti_3C_2*[233] *MOF/GO*[158], ***Table 11****);* ***(G)*** *Cycling performance of Li-S batteries at 0.1C at various sulfur loading.* ***(H)*** *Cycling performance Li-S batteries with np-ANF membrane at a rate of 0.2 C after 500 cycles at sulfur loading of 5.8mg cm^{-2}.*

3.3.4 Excellent High-Temperature Resistance Capability

The tolerance of a Li-S batteries to elevated temperatures is an important indicator in determining their safety, as the high temperature can also aggravate the dissolution of polysulfides, accelerating the consumption of active materials and the attenuation of capacity. Thus, the batteries with *np-ANF* membranes were evaluated at 80℃. The *np-ANF* cells show an *increase* in capacity to 1346 $mAhg^{-1}$ at 0.1C (**Figure 3.5 A**) in comparison with room temperature cycles (1268 $mAhg^{-1}$) [192], [234]. When the current density increased stepwise, the discharge capacities of the *np-ANF* were 1249, 1140, 1032, 916 and 801 $mAhg^{-1}$ at 0.2 C, 0.5 C, 1C, 2C and 3C, respectively, with a capacity retention of around 60%, exhibiting a much better high-temperature rate performance than that of cell with *Celgard™ 2400* membranes. When the charge/discharge rate was reduced back to 0.1C, a discharge capacity of 1302 $mAhg^{-1}$ was observed and almost kept steady for the subsequent 100 charge-discharge cycles whereas the capacity decreased rapidly and fell to below 300 mAh g^{-1} after only 60 cycles for the cell with *Celgard™ 2400* membrane (**Figure 3.5 B**). The capacities of cell employing *np-ANF* increase due to the increased diffusion coefficient of Li^+ in polysulfides **(Figure 3.5 C**), whereas an opposite trend was observed for *Celgard™ 2400* membrane due to the rapid self-discharge caused by crossover of LPS. The battery with *np-ANF* also display long cycle life with a low-capacity decay (0.081% per cycle) over 500 cycles at 3C and the Coulombic efficiency remain 95-99% **(Figure 3.5 D)** at temperatures as high as 80 ºC, which is exceeds the state-of-the art of Li-S batteries (**Table 13**).

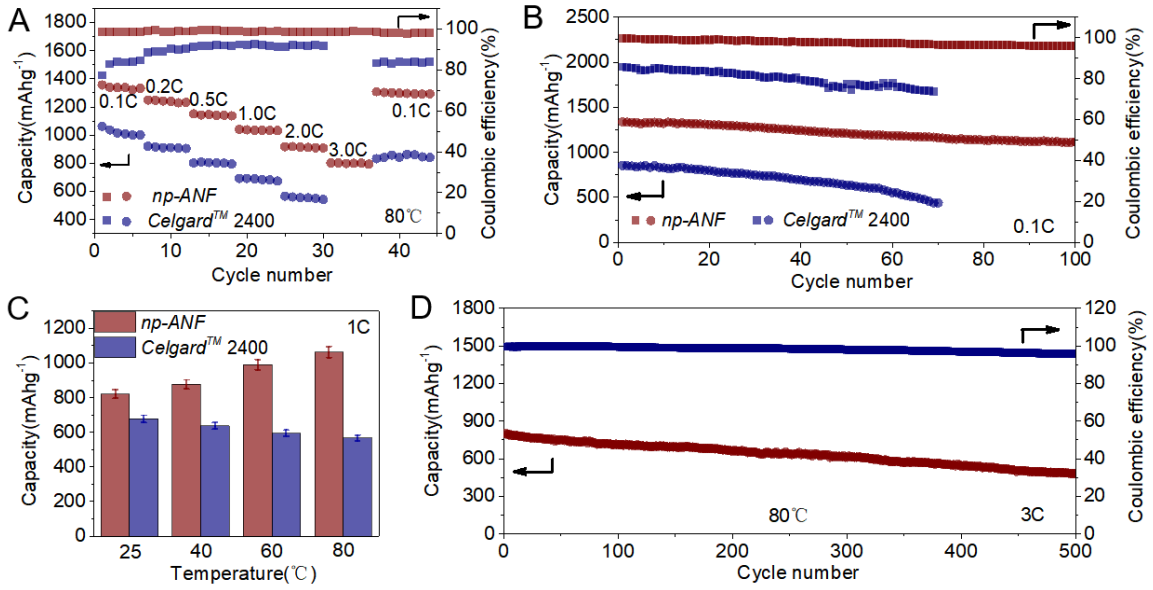

Figure 3.5 *Electrochemical performance of the Li-S batteries with np-ANF and Celgard™ 2400 membrane at elevated temperature of 80 °C. (A) Rate performance of Li-S batteries ranged 0.1C to 3C with np-ANF and its comparison of Celgard™ 2400 (B) Cycling performance of Li–S batteries at 0.1C at 80 °C. (C). The capacity comparison of np-ANF and Celgard™ 2400 membrane at different temperatures. (D). Cycling performance Li-S batteries with np-ANF membrane at a rate of 3 C after 500 cycles at 80°C.*

3.3.5 Excellent Dendrite Suppression Capability

Li metal anodes also suffer from dendrite growth upon charging. To demonstrate dendrite suppression by *np-ANF* membrane, cyclic charge/discharge in a symmetrical Li/membrane /Li with 1mol/L $LiCF_3SO_3$ DOL : DME (v/v=1/1) cell were evaluated over 250 hours **(Figure 3.6A)**. The cell with *np-ANF* exhibited negligible loss or fluctuation of voltage, whereas the voltage of cells from *Celgard*^{TM} 2400 increased over cycles, by almost 100% after 250 hours due to dendrite induced soft short circuit. To study the evolution of the voltage profiles in detail, the 10h 100h and sudden increase cycling of the cells with *np-ANF* and *Celgard*^{TM} 2400 membrane were further enlarged as the insets in **Figure 3.6 A**. Flat voltage profiles at both the charging and discharging states can be retained throughout the whole cycle without obvious increases in hysteresis for cells with *np-ANF* membranes, whereas batteries with *Celgard*^{TM} 2400 showed fluctuating voltage profiles with consistently higher overpotential at both the initial and final stages of each stripping/plating promoting the growth of dendrites. Greatly improved cycling stability were also observed with *np-ANF* as we increased the current density to 2mAcm^{-2} and 3mAcm^{-2} process (**Figure 3.6 B-C**), whereas the cells with *Celgard*^{TM} 2400 exhibited gradual increase of the hysteresis. Although high rate charge/discharge cycling stimulates the dendrite growth, the surface image of lithium electrode remained consistently flat even at a high current density of 3mAcm^{-2} after 250 hours cycling (**Figure 3.6 E**). Lithium cells with *Celgard*^{TM} 2400 displayed rough surface and massive formation of dendrites after 250 hours cycling under the same conditions or even at a lower current density 1 mAcm^{-2} (**Figure 3.6 F-G**). At a high current density of 2 mAcm^{-2} and 3 mAcm^{-2}, extensive growth of dendrites was observed on lithium electrode surface (**Figure 3.6 H-I** and **Figure S 39**). Such drastically different results further demonstrate the advantages of *np-ANF* membranes.

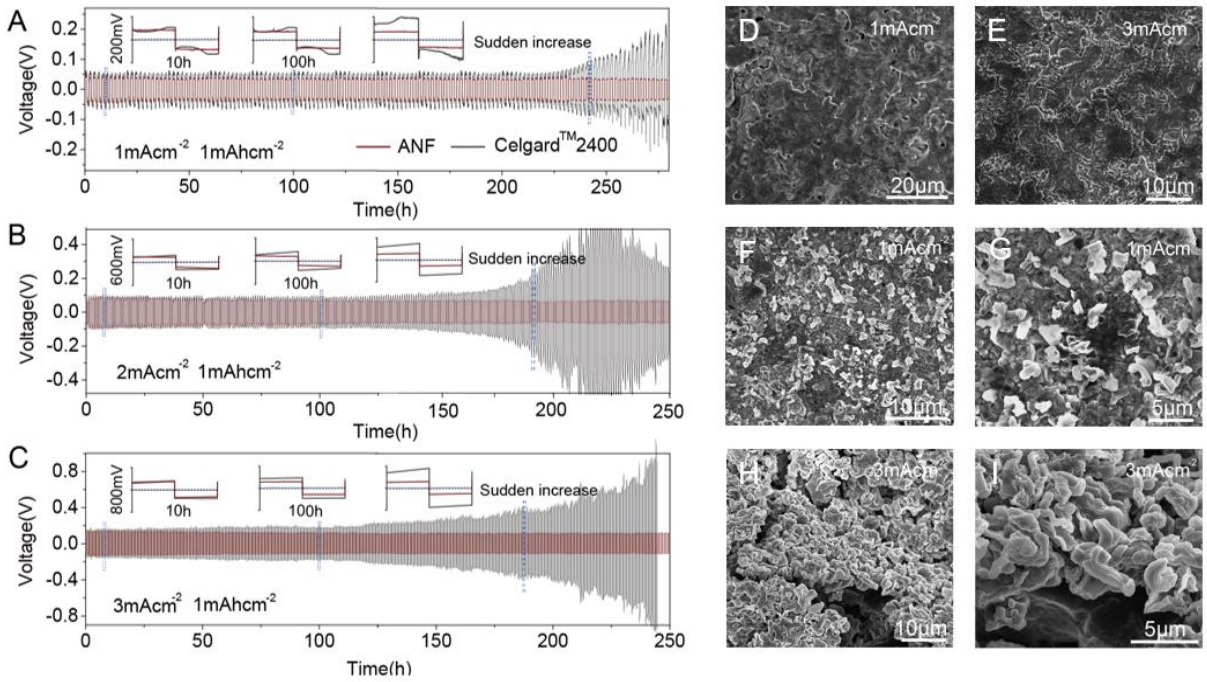

Figure 3.6 *Comparison of the cycling stability of the np-ANF and the Celgard™ 2400 membrane at a current density of* ***(A)*** *1mAcm^{-2},* ***(B)*** *2mAcm^{-2} and* ***(C)*** *3mAcm^{-2} with a stripping/plating capacity of 1 mAhcm^{-2}. SEM images of the lithium electrode with np-ANF membrane after 250 hours cycles of stripping/plating in 1 mol/L $LiCF_3SO_3$ DOL: DME v/v = 1/1) at a current density* ***(D)*** *1 mAcm^{-2} and* ***(E)*** *3 mAcm^{-2}.* ***(F-I)*** *SEM images of the lithium electrode with Celgard™ 2400 membrane after 250 hours cycles of stripping/plating in 1mol/L $LiCF_3SO_3$ DOL: DME v/v = 1/1 at a current density (F), magnified image(G) 1mAcm^{-2} and (H), magnified image (I) 3 mAcm^{-2}.*

3.3.6 Excellent Overall Performance for Li-S Batteries

As an example of a complex task to engineer a battery satisfying several often contrarian parameters such as high discharge rate and long cycle life, we carried out multiparameter performance assessment of Li-S cells with *np-ANF* separators using glyph plots (**Figure 3.7**). The following parameters were chosen to evaluate the state-of the-art Li-S batteries due to their significance to multiple technologies: initial discharge capacity at 0.1C (mAhg^{-1}); initial discharge capacity at 1.0 C (mAhg^{-1}); cycle life at 1.0C; capacity retention at 1.0 C (%); Coulombic efficiency (%); maximum sulfur loading (mg/cm^2); maximum operational temperature (°C). Since battery capabilities increase with the increase of all of these metrics, the total area encircled by the glyph plot can be used as a cumulative capability criterion (CCC, %) to compare and optimize the batteries. CCC is enumerated as percentage of area encircled by the glyph plot from the maximum

possible for the capability-relevant range of properties (**Figure 3.7**). The assessment shows that cells with *np-ANF* membranes have across-the-board performance exceeding the current state-of-the art in Li-S batteries. When needed other longer list of the parameters can be selected, albeit methodology may remain the same.

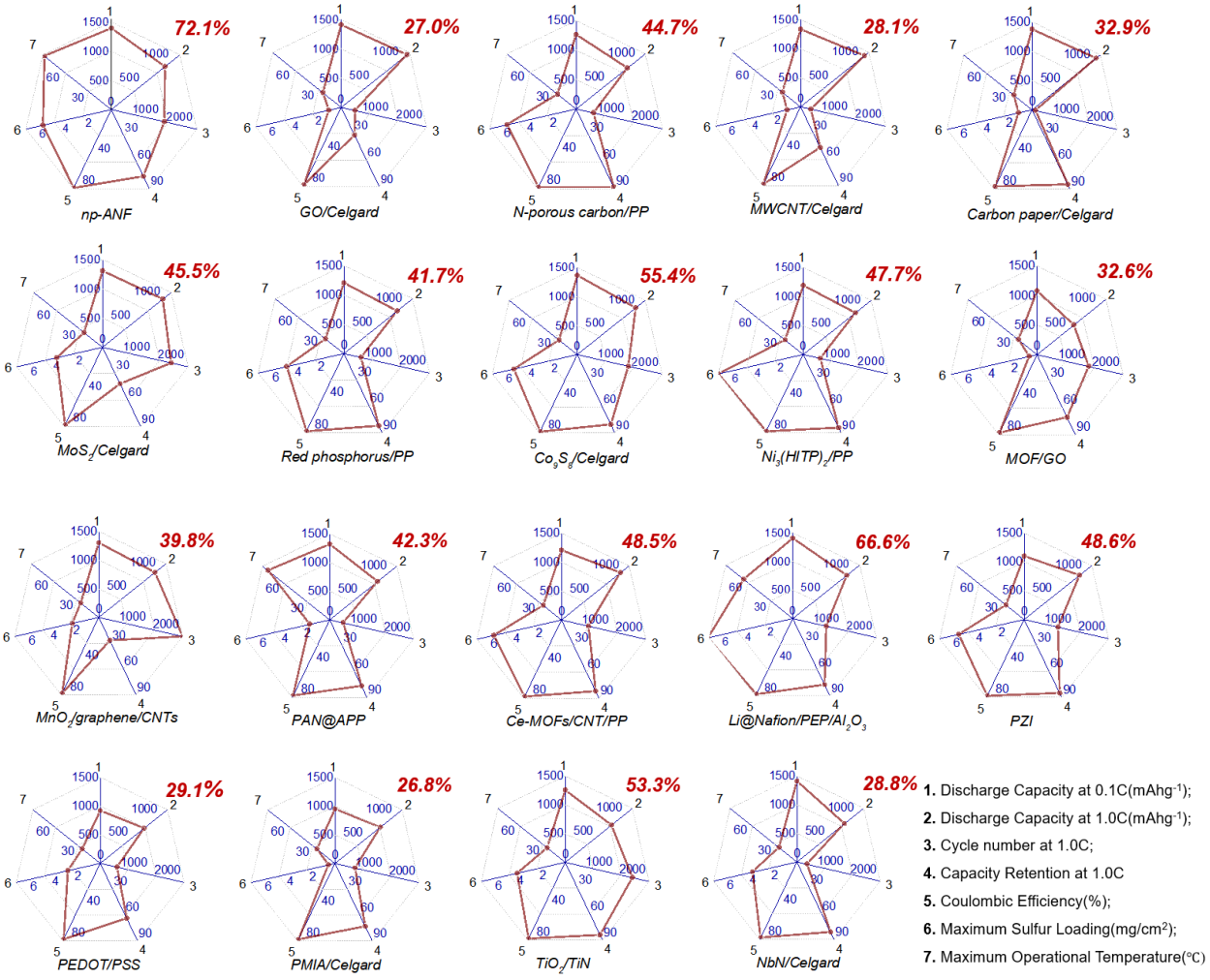

Figure 3.7 *Multiparameter comparison of various for Li-S batteries based on glyph plots. And cumulative capability criterion (CCC). The value of CCC is given in the top red corner of each glyph plot. The detailed data set for the plots is given in Supplementary Information in* ***Table 14.***

3.4 Discussion

In summary, *np-ANF* with layer of LPS bound to the surface of the layered composite serves as effective ion-selective membranes facilitating the transport of Li^+ and blocking the transport of LPS as shown in experiments and computations. In addition to size filtration by small pore size of *ANF*, its surface charge density plays a crucial role for selectivity of ion transport. While negatively charged *np-ANF* membrane nanochannel ensure steady Li ion flux, it repels negatively charged LPS and collaboratively blocks LPS shuttle. Their multifactorial engineering encompassing narrow pore size, negative charges, high mechanical and thermal properties collectively lead to the promising electrochemical performance in Li-S batteries exceeding the current state of the art comparing several singular parameters and across-the-board performance. Simplicity of *np-ANF* fabrication and availability of parent material Kevlar as a recyclable polymer enables their broad utilization in different energy-storage technologies.

3.5 Experimental Method

3.5.1 Preparation of the aramid nanofibers (ANFs) and ion-selective membranes from them.

To prepare the ANF dispersion, the fabrication method is report previously [20]. 1 g of bulk Kevlar 69 (from Thread Exchange) and 1.5 g KOH were added into 500 mL of dimethyl sulfoxide (DMSO) which was magnetically stirred for two weeks at room temperature forming a dark red solution of ANF. For layer-by-layer (LBL) assembly of nanoporous ANF-based membranes abbreviated here as *np-ANF*, microscope glass slides were cleaned in piranha solution (3:1 H_2SO_4/H_2O_2) for 24 h, followed by thorough rinsing with deionized water before use. After that, setting a clean piece of the glass slide on the disk of the spin coater, 2 mL of ANF (2wt%) solution was dropped and spin-coated at 1500 rpm for 30 s. After spin coating, the membrane was

immediately put into DI water to remove the DMSO and then dried at 70 ℃ at oven 10min. Then the glass slide was dipped into 0.1wt% poly(diallyldimethylammonium chloride) (PDDA) solution to change the charge for 1 min and rinsed with water for 2 min before air drying. This sequence of steps was repeated 3 times and the last layer is ANF. It should be noted that the thickness of membrane can be ranged by increase or decrease the membrane's layer. The membrane is peeled from the substrate by immersing in 0.1% (hydrofluoric acid) HF solution. The remaining chemicals were purchased from Sigma Aldrich without further purification.

3.5.2 Structural Characterization:

The morphology of the Li dendrite, *Celgard*^{TM} 2400 and *np-ANF* membrane were inspected with a scanning electron microscope (SEM, FEI Nova Nanolab dual-beam FIB).

The *np-ANF* before and after Li_2S_4 adsorption were measured by Raman spectra (LabRAM HR 800 spectrometer at 785 nm) and X-ray photoelectron spectra (XPS, Thermo Fisher Scientific, USA. The data were obtained in an XPS system, via monochromatic Al Kα radiation with a pass energy of 50eV.) Note: *The np-ANF* membrane was immersed into 0.5 M Li_2S_4 in DOL/DME 10 hours at room temperature (25℃) followed by repeated pure DOL/DME solution washing to remove any residual LPS and then dried in glovebox.

Quantachrome Autosorb 6B system was used to characterize the pore width of the *np-ANF* membrane using nitrogen sorption under 77.4 K. The pore size distributions of the *np-ANF* membrane was calculated by Barrett-Joyner-Halenda (BJH) methods. Contact angle was measured by Cam-plus Micro meter with the sessile drop technique. The mechanical tests of the membranes were performed on a TA XT Plus Texture Analyzer (Stable Micro Systems Ltd.) instrument at room temperature, with the test of longitudinal direction carried out at a rate of 2mm min^{-1}. The film was cut into rectangular strips of 20 mm × 5 mm, and twenty samples were tested in each case. The thermal stability of membrane was analyzed by TA Instruments Discovery thermogravimetric analyzer (TGA) with a temperature ramp to 700 at 10 °C min^{-1} in nitrogen at a flow rate of 30 mL min^{-1} and differential scanning calorimetry (DSC) with a temperature ramp to 500 at 10 °C min^{-1} in nitrogen at a flow rate of 30 mL min^{-1}.

3.5.3 Visualization of ion-selectivity

The electrochemical cell test that cab visualizes LPS blocking was carried out in an H-type glass cell to examine the properties of the membrane. *Celgard*^{TM} 2400 and *np-ANF* membranes were set in the middle of glass cell. The left chamber was filled with 0.5 M Li_2S_4 solution with DOL /DME (v/v = 1:1) as the solvent, while the right chamber was only filled with DOL/DME solvent (v/v = 1:1). The Li_2S_4 was prepared by a synproportionation reaction [235] between Li_2S and S with a mole ratio of 1:2.

3.5.4 Computation for the transport of charged ion species.

To elucidate the mechanism of selective ion transport through the *np-ANF* membrane, we have simplified the system as a single nanopore channel of the np-ANF membrane connecting two reservoirs. The 2D nanochannel model was implemented in the commercial finite element solver, COMSOL Multiphysics.

3.5.5 Model Geometry

The system consists of electrolyte reservoirs connecting through the 10 nm long nanochannel. The diameter of the channel was set to 1 nm based on the experimental pore size determined by the Barrett-Joyner-Halenda analysis (**Figure S 26**, **Figure S 27**). Both the reservoirs and nanochannel are represented by dielectric blocks with the electrolyte.

Governing Equation

The dynamics of our system can be solved by the coupled Poisson, Nernst-Planck and Navier-Stokes equations, a well-known set of partial differential equations that represents the electrostatic field, the ionic flux and the fluid flow, respectively.[236]–[239]

3.5.6 Electrostatic field

The electrostatic potential of the system has evaluated using Poisson's equation, solved using the electrostatic interface in COMSOL. For the potential, Poisson's equation states:

Equation 3 $\nabla \cdot (\varepsilon_0 \varepsilon_r \nabla \phi) = -\rho,$

where ϕ is the electric potential, ε_0 the vacuum permittivity (8.854 19×10−12 F · m^{-1}), ε_r relative permittivity of the material, and ρ total charge density which was derived from zeta potential measurements.

3.5.7 Ionic flux

The total ionic flux J_i of each ion, *i*, is governed by the Nernst-Planck equation which can be expressed as the sum of diffusive, electrophoretic, and convective fluxes:

Equation 4 $J_i = -[D_i \nabla c_i + z_i \mu_i c_i \nabla \phi - \boldsymbol{u} c_i],$

with D_i being the ion diffusion coefficient, c_i the ion concentration, z_i the ion charge number, μ_i the electrophoretic mobility of ion *i*, and ***u*** the fluid velocity.

And assuming no homogeneous reaction in the electrolyte, at steady state, the governing equations for the species become:

Equation 5 $\frac{\delta c_i}{\delta t} = -\nabla \cdot J_i = 0,$

3.5.8 Fluid flow

The fluid flow model is set as an incompressible flow regulated by the Navier-Stokes equations:

Equation 6 $£\frac{\delta \boldsymbol{u}}{\delta t} + (\boldsymbol{u} \cdot \nabla)(£\boldsymbol{u}) = \nabla \cdot [-p\boldsymbol{I} + \boldsymbol{K}] + \boldsymbol{F}$,

with the hydrodynamic stress tensor, $\mathbf{K} = \eta [\nabla \boldsymbol{u} + (\nabla \boldsymbol{u})^{T}]$ and the continuity equations, $£ \nabla \cdot \boldsymbol{u} = 0$.

where £ is the fluid density, η the dynamic viscosity, p the pressure F is the volume force vector.

3.5.9 Multiphysics Coupling

Other than potential coupling from electrostatic to the transport of diluted species interface, space charge density coupling has been added by defining dependence of the space charge density (SI unit: C/m^3), ρ, on the ion concentrations:

Equation 7 $\rho = F \sum_i z_i c_i$

with F Faraday's constant (96 485.33 $C \cdot mol^{-1}$), and ci the ion concentration and z_i ion charge number of ion *i*.

3.5.10 Electrochemical Performance Tests

Standard 2032-coin cells (MTI) were used to evaluate the electrochemical performance of the *np-ANF* membrane-incorporated lithium sulfur batteries. The C/S cathode materials were fabricated with a typical melt-diffusion strategy. The nanocarbon were firstly mixed with sulfur powder with a mass ratio of 3:6 by milling. The mixture was subsequently placed in a sealed flask at 155 °C for 10.0h to incorporate S into the carbonaceous matrix. The cathode slurry was then prepared by mixing 90wt% sulfur/carbon composite and 10% poly(vinylidene fluoride) binder in N-methylpyrrolidone (NMP) solvent dispersant. The cathode was constructed by coating the slurry on aluminum foil and drying at 60 ℃ at vacuum oven for 24.0 h. The sulfur loading was 1.2 mg cm^{-2} for the regular tests and around 3.6 mg cm^{-2} and 5.8 mg cm^{-2} for the high sulfur loading test.

The metallic lithium foil purchased from MTI Corporation was directly used as the anode. Then 1M LiTFSI solution in DOL/DME (v/v = 1/1) was used for the cells and the electrolyte/sulfur ratio was controlled at 10:1 (μL mg^{-1}). The separator used in the cell were routine *Celgard*^{TM} 2400 or *np-ANF*. The coin cells were tested in galvanostatic mode at various currents within a voltage range of 1.5-2.8 V using LAND-CT2001A battery-testing instrument. Both CV and EIS were performed on an Autolab (Autolab Potentiastat and Solartron 1260 frequency response analyzer). The EIS carried out in the range from 100 kHz to 0.05 Hz with potential amplitude of 20 mV. The resulting Nyquist plots were fitted to an equivalent circuit where ionic conductivity was then calculated from the **Equation 1** where *L* is the thickness of the film, R_b is the bulk resistance, and A is the contact area of film. The CV was scanned at a rate range of 0.10 -0.50 mV s^{-1}. The capacities were calculated based on the mass of sulfur in the cathode.

The lithium-ion diffusion coefficient D_{Li+} (cm^2 s^{-1}) was evaluated by cyclic voltammetry and calculated according to the Randles-Sevick equation [158], [221], [222]:

Equation 8 $I_p = 2.69 \times 10^5 n^{1.5} A D_{Li^+}^{0.5} C v^{0.5}$

in which *Ip* (A) is the peak current, n represents the number of electrons of in the reaction (for Li-S batteries, $n = 2$), A(cm^2) indicates the electrode area (1.54 cm^2 here), C_{Li+} (mol/mL) means the lithium-ion concentration(0.1mol/L) in the electrolyte, and *v* is the scanning rate (Vs^{-1}).

The Li^+ transference number (t_{Li+}) for different separators was evaluated by a potentiostatic polarization method of a constant potential at 10 mV was applied for 10000s to record the current at initial and steady-state. Each membrane was separately sandwiched between two lithium metal electrodes in a coin type cell (CR2023) and saturated with 1 M LiTFSI in DOL/DME (v/v=1:1) electrolyte. The Li^+ transference number was calculated from the ratio of steady state current to initial state current according to the following equation:

Equation 9 $t_{Li+} = I_s/I_0$

where t_{Li+} is transference number, while I_s and I_0 represent the current at the steady state and initial state, respectively.

3.5.11 The relationship between Young's Modulus and dendrite suppression

The model developed by Monroe and Newman show that that dendrites become unstable when the interfacial stability parameter $\Delta\mu$ changes from positive to negative.[195] For the interface between lithium and polyethylene oxide (PEO), this transition occurs when

Equation 10 $G_{PEO}/G_{Li} = 1.65$

where G_{PEO} and G_{Li} are shear moduli of the polymeric electrolyte and lithium metal, respectively. While the shear modulus G is related to Young's modulus, E, as

Equation 11 $G = 0.5\ E/(1+\nu)$

where ν is the Poisson's ratio of the material. In case of metallic Li and PEO, ν_{Li} = ~0.4 and ν_{PEO} = 0.33, respectively, leading to $G_{Li} = 0.5\ E_{Li}/(1+0.4)$ and $G_{PEO} = 0.5E_{PEO}/(1+0.33)$. Then, the threshold condition G_{PEO}/G_{Li} = 1.65 for Li/PEO interphase transforms into $1.4E_{PEO}/1.33E_{Li}$ = 1.65 or

Equation 12 $E_{PEO}/E_{Li} = 1.53$

Note that the threshold condition in **Equation 10** is dependent on Poisson's ratios of materials on both sides of the interface as can be seen by examining **Figure 3.3**, **Figure 3.4** and **Figure 3.6** in the original paper by Monroe and Newman.[195] However, the current battery literature is conceptualizing **Equation 10** as condition for dendrite suppression not just for PEO but for any material disregarding the dependence of the $\Delta\mu$ threshold and respect $G_{polymer}/G_{Li}$ on Poisson's ratio of the polymer. Examples of such approach in the current electrochemical literature are multiple.[240]–[245]

While being a deviation from the original expression for displacement functions (Eq. 16 from 2005 Monroe-Newman study) [195], such simplification driven by materials properties used in practice is justified because the Poisson's ratio of solid semi-crystalline and amorphous polymers vary in a narrow range of values.[246]–[248] The same logical path can be taken considering **Equation 12** leading to a modification of the original expression **Equation 10** as $E_{polymer}/E_{Li}$ = 1.53. Note that this expression is consistent with the Monroe-Newman framework of continuum mechanics and the assumption of small deformations and Hookean-elastic regime as well as subsequent elaborations on the theory of dendrite growth.[100], [195] Some of these points were also discussed in our prior publication [25].

3.6 Supplemental Information

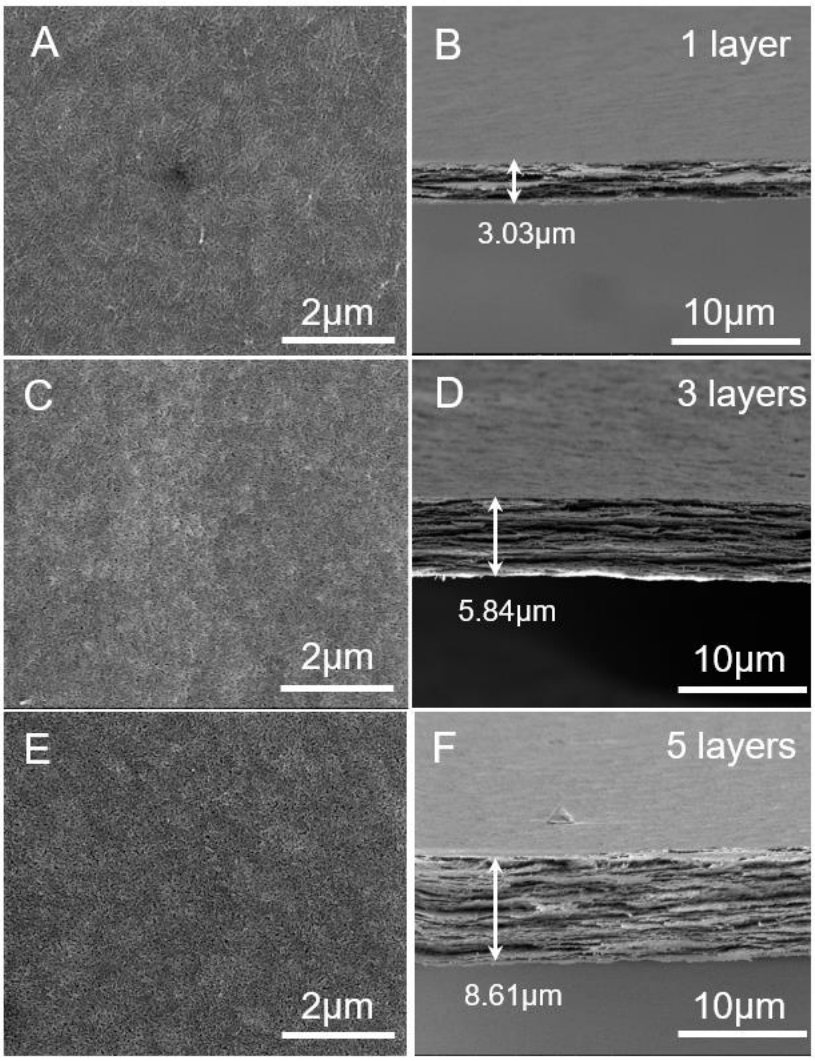

Figure S 22 *(A to F) The SEM images of the surface view and side view of np-ANF membrane with different thickness made by sequential deposition of nanofiber strata. (A and B) np-ANF membrane with one layer, (C and D), np-ANF membrane with three layers, (E and F), np-ANF membrane with five layers.*

Comment: While we used Layer-by-Layer (LBL/LbL) assembly to engineer the *np-ANP* composite, the single bilayers (i.e. ANF+PDDA) are thicker than the typical nanometer-scale bilayers from polyelectrolytes observed in LBL-made materials in the past. There is a distinct possibility that ANFs are depositing in the non-linear (exponential) fashion, which can lead to

the gradual increase in layer thickness over multiple consecutive cycles due to diffusion-in/diffusion-out mechanism.[249]–[251]

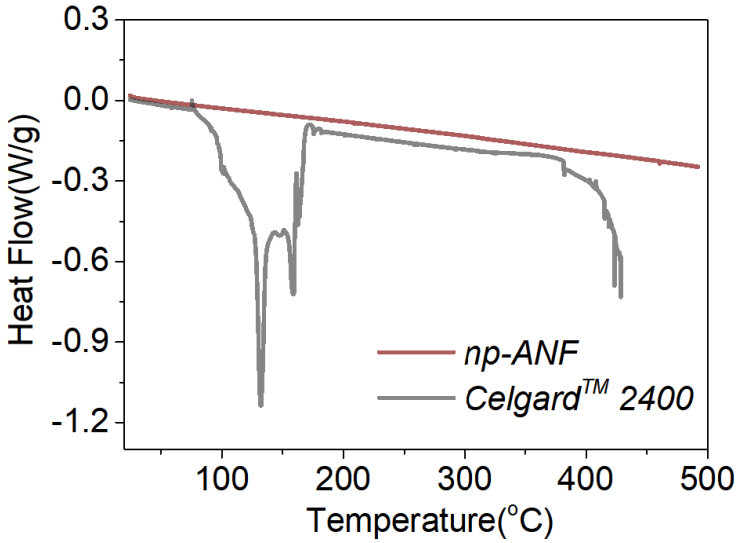

Figure S 23 *DSC curves comparison of np-ANF and CelgardTM 2400 membrane. The np-ANF membrane shows excellent thermal stability with no obvious phase change until 500°C. The superior thermal tolerance could effectively prevent internal short-circuit at elevated temperature. In comparison, CelgardTM 2400 decomposes sharply at 300 °C and exhibits an endothermic peak at 122 °C.*

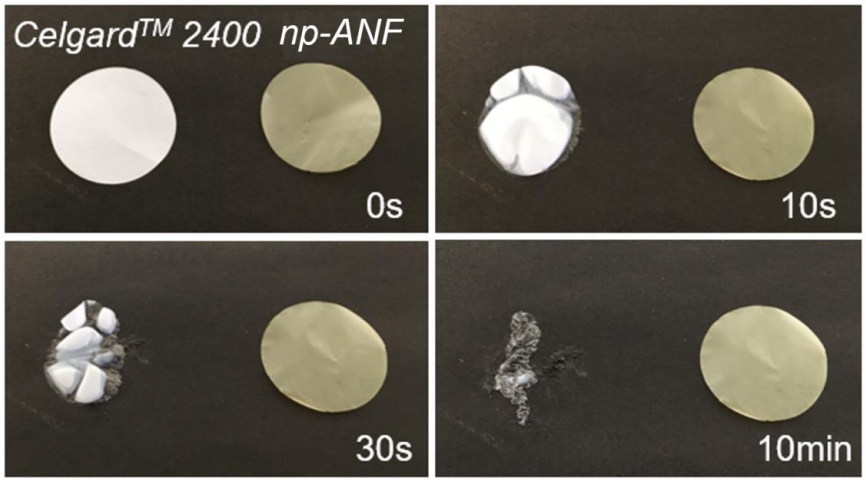

Figure S 24 *Hot solder iron test on np-ANF and CelgardTM 2400 membrane at 150℃ with increase time. The time-lapse photography demonstrates a clear difference between two membranes of np-ANF and CelgardTM 2400 on a 150 °C hot plate. The np-ANF remained unchanged, showing good thermal stability, while CelgardTM 2400 membrane shrank strongly.*

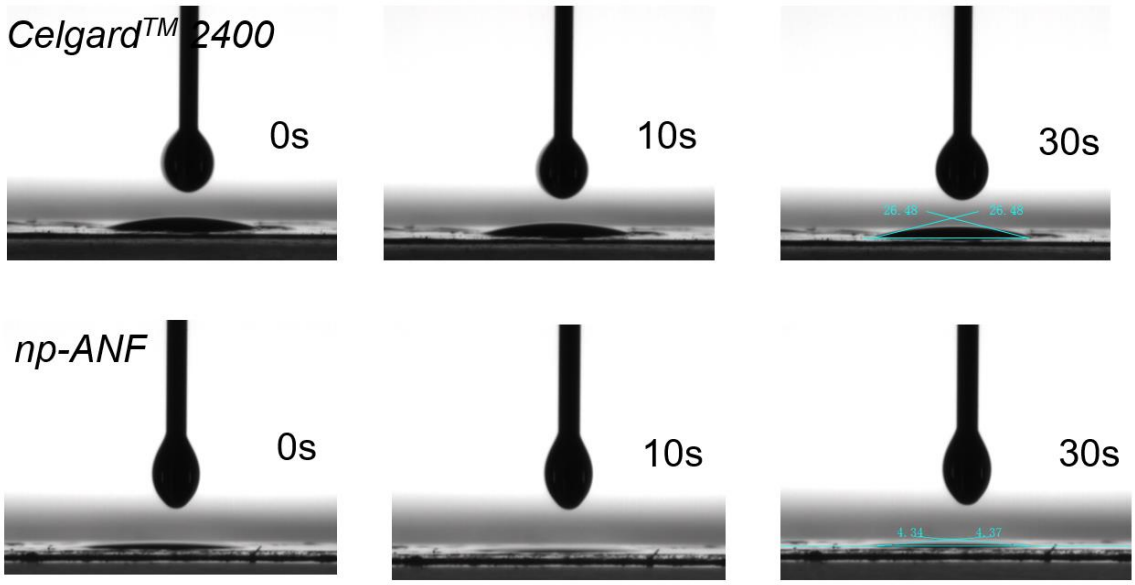

Figure S 25 *Photographs of static liquid electrolyte contact angles of different separators at different rest time. 1 M LiTFSI with 2 wt% LiNO3 in DOL/DME (v/v=1:1) was used as a liquid electrolyte.*

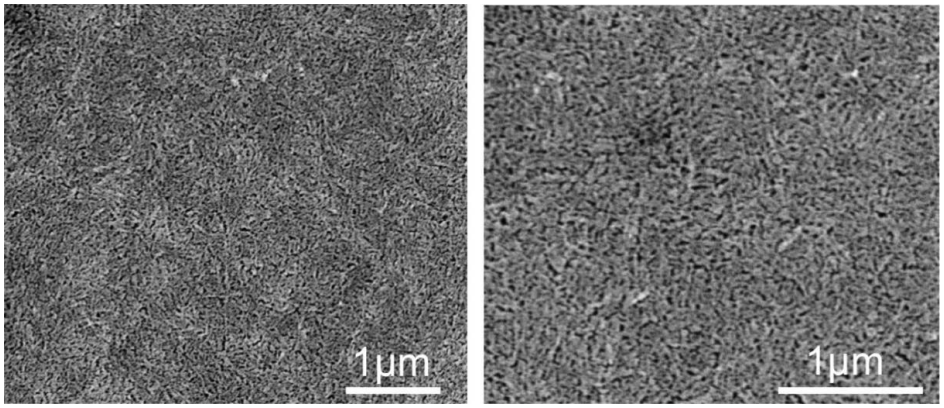

Figure S 26 *The magnified SEM images of the surface view np-ANF membrane made after three deposition cycles.*

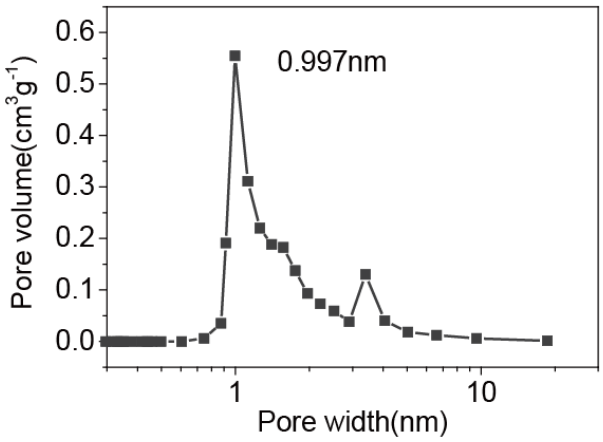

Figure S 27 *Pore size width distributions of the np-ANF membrane obtained from Barrett-Joyner-Halenda (BJH) analysis.*

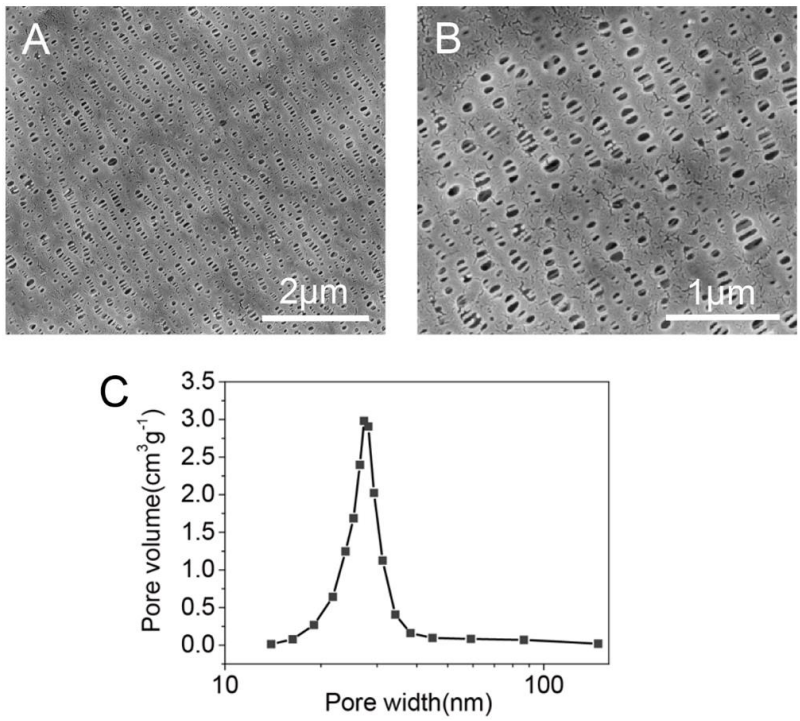

Figure S 28 *(A-B) SEM image of surface of CelgardTM 2400. (C) The pore size width distributions of the CelgardTM 2400 obtained from Barrett-Joyner-Halenda (BJH) analysis.*

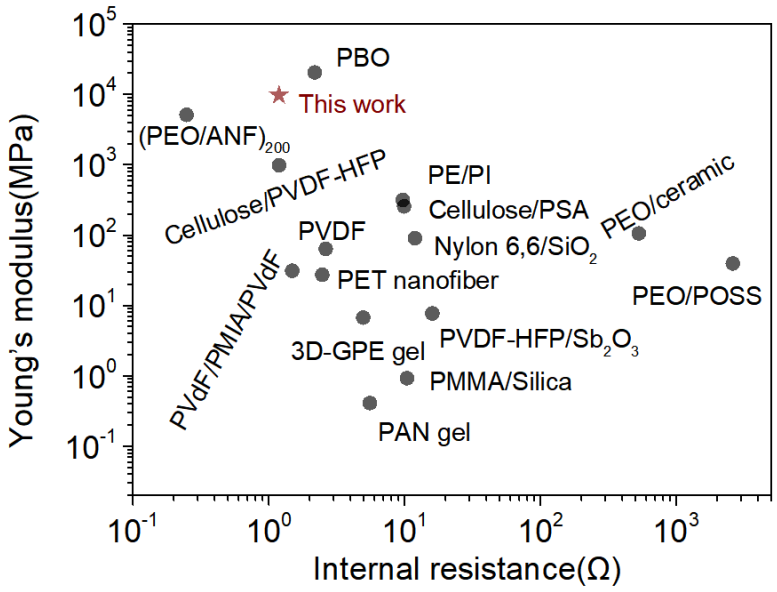

Figure S 29 *Comparative evaluation of Young's modulus and internal resistance normalized to a standard CR2032 coin cell for np-ANF and other membranes. The internal resistance of np-ANF membrane is obtained by electrochemical impedance spectroscopy (EIS) curve of Li/ np-ANF /Li in DOL/DME solution with a standard CR2032 coin as shown in* ***Figure S 30****. The corresponding references and the list of abbreviations are given in* ***Table 8****.*

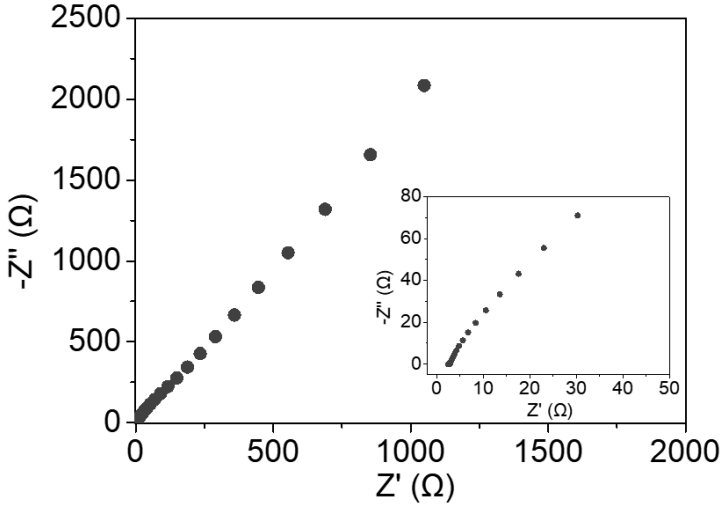

Figure S 30 *The impedance spectra of Li/ np-ANF /Li using standard CR2032 coin cell.*

Table 7 *Tensile strength, tensile modulus and elongation at break of np-ANF and Celgard™ 2400 membrane*

	Thickness (µm)	**Tensile strength (MPa)**	**Tensile modulus (GPa)**	**Elongation at break (%)**
np-ANF	5.8±0.5	167.4±8.4	9.2±0.5	1.82±0.09
Celgard™ 2400	25±1.3	74.5±3.7	0.17±0.02	43.8±2.2

Table 8 *Young's moduli and internal resistances data for different materials for batteries.*

Membrane	**Description**	**Young's modulus (MPa)**	**REF**
PBO	PBO stands for Poly-p-Phenylene Benzobisoxazole memberane	$2x10^4$	[252]
Cellulose/PVDF-HFP	It stands for Cellulose/ Poly(vinylidene fluoride-hexafluoropropylene composite nonwoven	960	[253]
Cellulose/PSA	It stands for Cellulose/Polysulfonamide composite membrane	250	[254]
PE/PI	It stands for Polyethylene co-polyimide copolymer composite membrane	308	[255]
PVdF/PMIA/PVdF	PVdF/PMIA/PVdF stands for PVdF/ Poly(m-phenylene isophthalamide) /PVdF nanofiber composite membrane	30.3	[256]
PVDF-HFP/Sb_2O_3	It stands for PVDF-HFP/Sb_2O_3 composite membrane	7.52	[257]
PVDF	It stands for PVDF porous membrane	62.08	[258]
PEO/ceramic	It stands for Poly(ethylene oxide)/ceramic composite membrane	103	[259]

PEO/POSS	It stands for PEO/polyhedral oligomeric silsesquioxane composite membrane	38.5	[260]
$(PEO/ANF)_{200}$	It stands for $(PEO/Aramid\ nanofibers)_{200}$ composite membrane	$5x10^3$	[25]
PMMA/Silica	It stands for Poly(methylmethacrylate) /Silica composite membrane	0.9	[261]
PAN gel	It stands for Polyacrylonitrile gel membrane	0.4	[262]
3D-GPE	It stands for Diglycidyl ether of bisphenol-A, Poly(ethylene glycol) diglycidyl ether, Diamino-poly(propylene oxide) composite gel	6.56	[263]
PET	It stands Polyethyleneterephthalate nanofiber membrane	26.6	[264]
Nylon 6,6/SiO_2	It stands Nylon 6,6/SiO_2 composite membrane	88	[265]

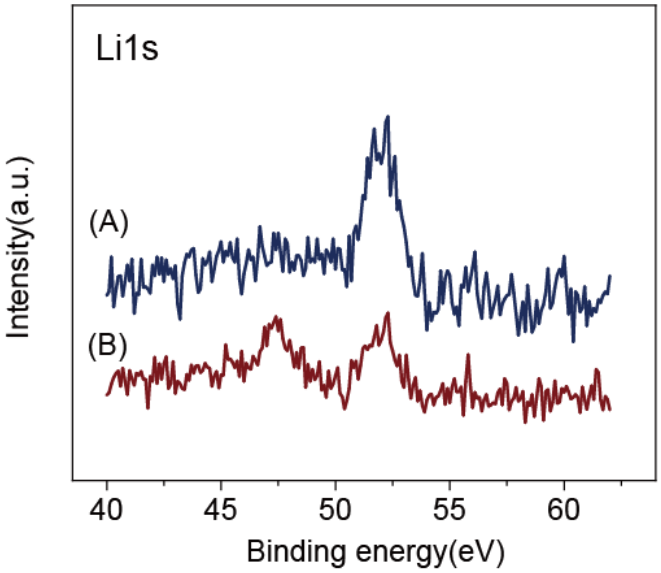

Figure S 31 *High-resolution XPS spectra of retrieved np-ANF sample (A) from $LiNO_3$ solution (B) from Li_2S_4 solution.*

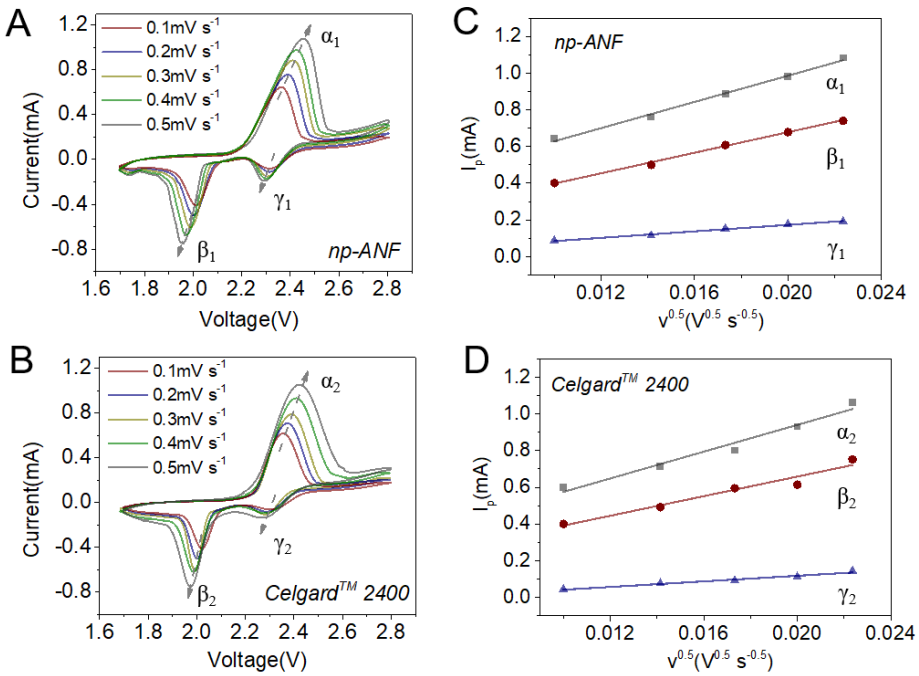

Figure S 32 *Cyclic voltammograms at different voltage scan rates of Li-S cells: (A) with np-ANF membrane and (B) with Celgard™ 2400 membrane; (C-D) the linear fits of the peak currents for cells with np-ANF (C) and Celgard™ 2400 (D) membranes.*

Table 9 Ion-transport parameters for *np-ANF* membranes and *Celgard™ 2400*

Parameters	***np-ANF***	***Celgard™ 2400***
Li^+ transfer number	0.63	0.68
D_{Li+} (cm^2 s^{-1}) A (anodic peak)	$9.263 \cdot 10^{-8}$	$9.693 \cdot 10^{-8}$
D_{Li+} (cm^2 s^{-1}) B (cathodic peak)	$5.310 \cdot 10^{-8}$	$5.129 \cdot 10^{-8}$
D_{Li+} (cm^2 s^{-1}) C (cathodic peak)	$0.421 \cdot 10^{-8}$	$0.567 \cdot 10^{-8}$

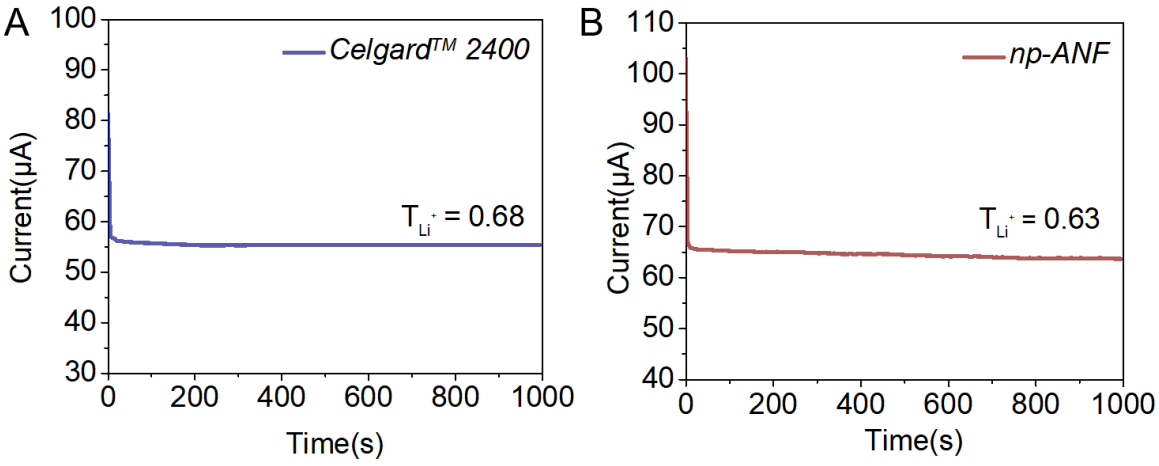

Figure S 33 *Lithium ions transference number for Celgard™ 2400 (A); np-ANF (B)*

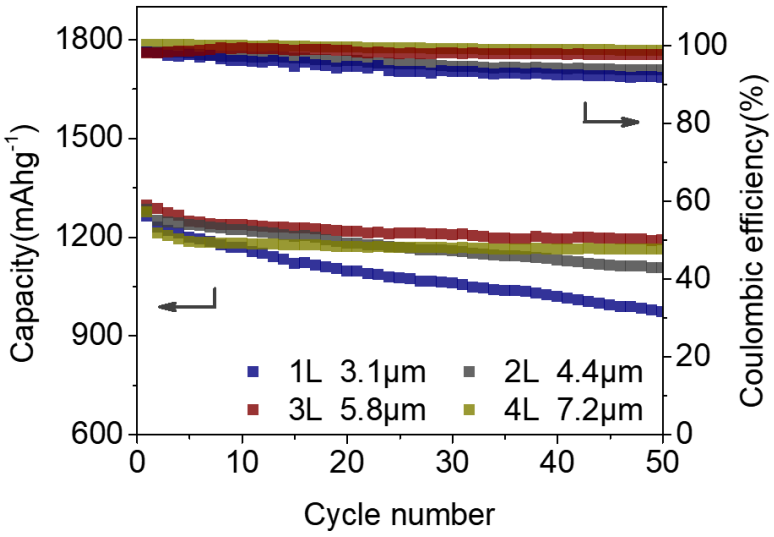

Figure S 34 *Cycling performance of Li-S batteries with np-ANF membranes with from one layer to four layers at 0.1C rate.*

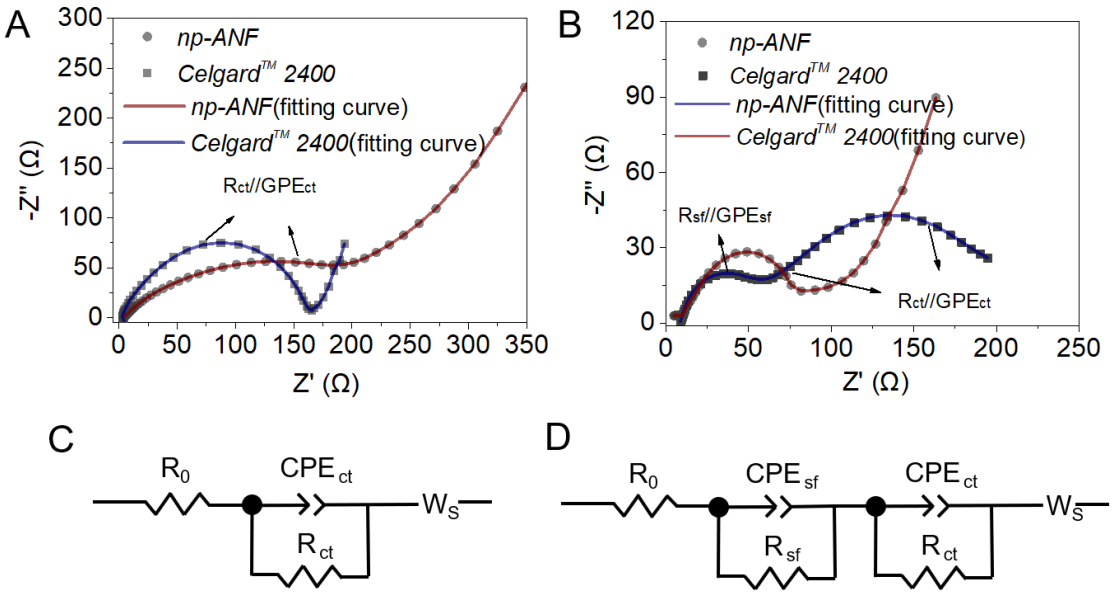

Figure S 35 *Electrochemical impedance spectra of Li–S batteries (**A**) before and (**B**) after cycling using Celgard™ 2400 and np-ANF membranes, and corresponding equivalent circuits before (**C**) and after (**D**) cycling; notations: R_0 is interphase-contact resistance of the electrolyte and battery; R_{ct} is the charge transfer resistance; R_{sf} is the surface film resistances; W_s is the Warburg impedance, CPE is a constant-phase element (CPE) attributed describing the double layer capacitance* [223], [227]

Table 10 *Fitting results of EIS plots in* ***Figure S 35****.*

Parameters	***np-ANF***		***Celgard^{TM} 2400***	
	Before cycling	*After 100 cycles*	*Before cycling*	*After 100 cycles*
R_0 (Ω)	*5.6*	*7.2*	*3.9*	*11.2*
R_{ct}//CPE_{ct} (Ω)	*255.4*	*93.6*	*166.1*	*162.8*
R_{sf}//CPE_{sf} (Ω)	--	--	--	*56*

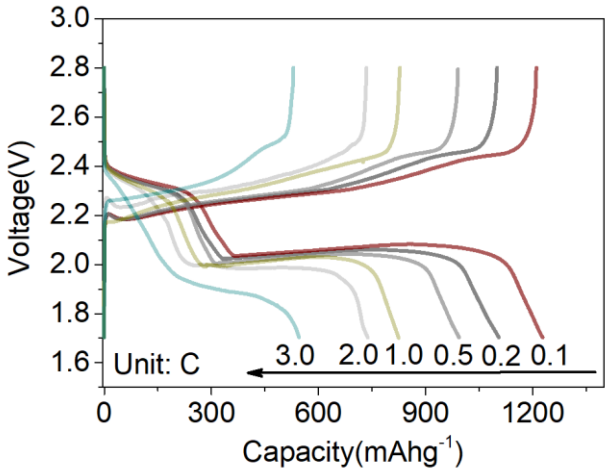

Figure S 36 *Rate performance of Li-S cell with np-ANF membrane at a sulfur loading of 1.2mg/cm^{-2}.*

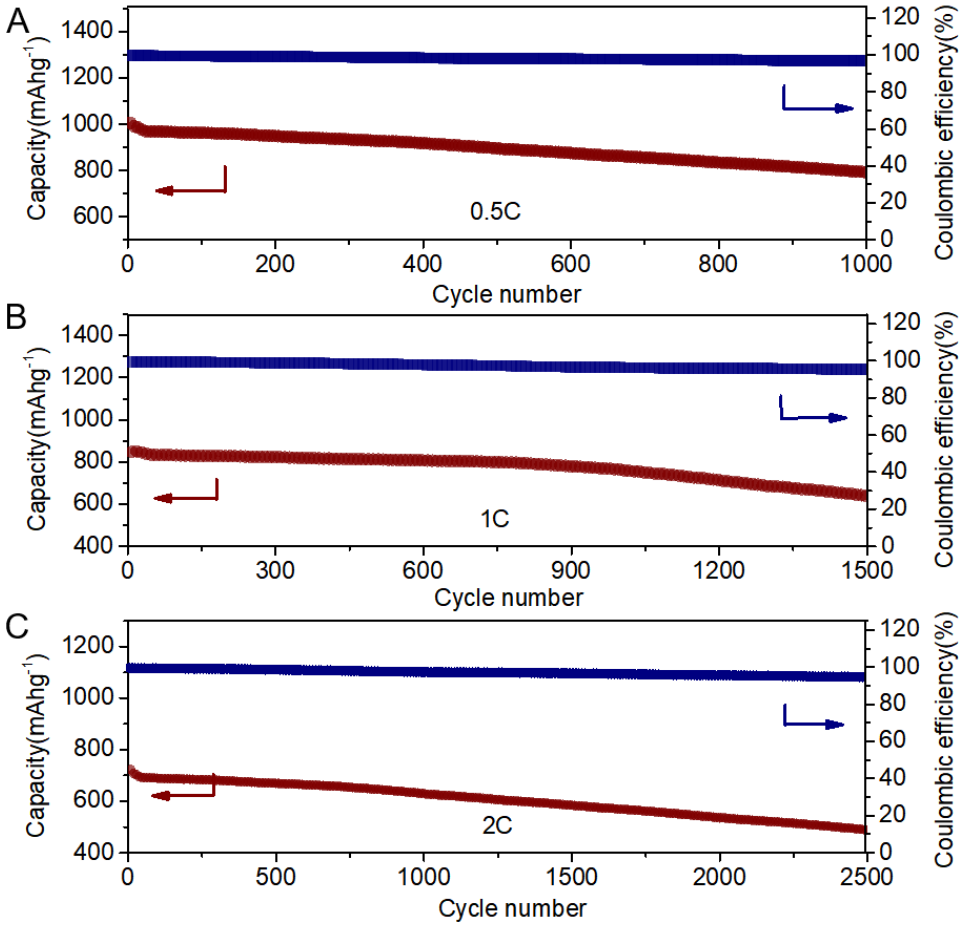

Figure S 37 *Cycling performance Li-S batteries with np-ANF membrane (A) at a rate of 0.5 C over 1000 cycles; (B) at a rate of 1C over 1500 cycles; (C) at a rate of 2C over 2500 cycles at a sulfur loading of 1.2mg/cm^{-2}*

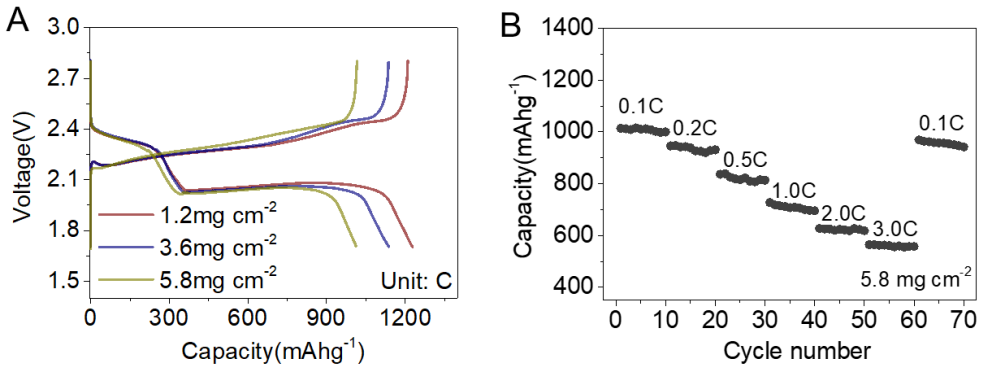

Figure S 38 *Electrochemical performance of the Li-S batteries with np-ANF with various sulfur loadings. (A) Charge and discharge curve of Li-S batteries with np-ANF membrane at various sulfur loadings. (B). Rate performance of Li-S batteries ranged 0.1C to 3C with np-ANF at a sulfur loading of 5.8mg cm^{-2}.*

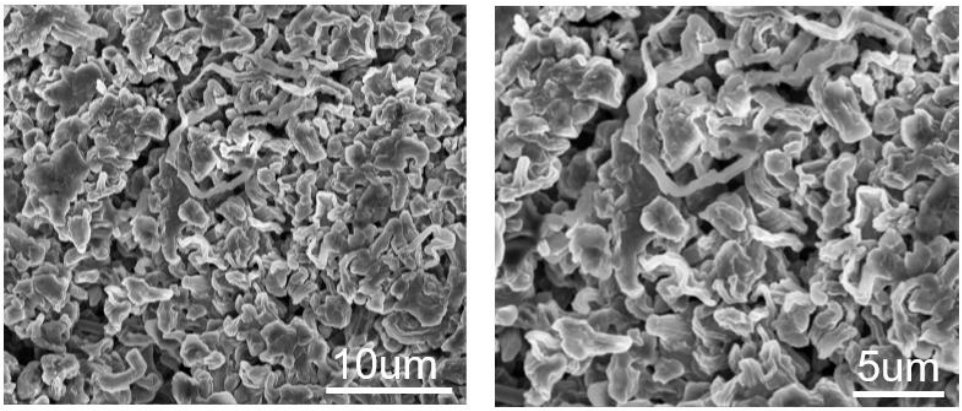

Figure S 39 *SEM images of the lithium electrode with Celgard™ 2400 membrane after 250 hours cycles of stripping/plating in 1mol/L $LiCF_3SO_3$ DOL: DME v/v = 1/1) at a current density of 2mAcm^{-2}.*

Table 11 *The summary of comparative performance for Li-S batteries with different structural designs of membranes*

Functional Membrane coating on to PP/PE	Electrochemical Performance					REF
	Initial discharge capacity ($mAhg^{-1}$)	Capacity retention (%)	Capacity fade per cycle(%)	Current density(1C = 1675 mA g^{-1})	Number of cycle	
np-ANF	*1268*	*85%*	*0.092%*	*0.1C*	*300*	
np-ANF	*969*	*79.2%*	*0.02%*	*0.5C*	*1000*	
np-ANF	*825*	*76.0%*	*0.016%*	*1.0C*	*1500*	
np-ANF	*703*	*69.6%*	*0.012%*	*2.0C*	*2500*	
np-ANF	*521*	*64.7%*	*0.01%*	*3.0C*	*3500*	
Graphene oxide	1170	32%	0.93%	1.0C	400	[219]
Graphene oxide	920	77%	0.23%	0.1C	100	[218]
Graphene	1052	70%	0.1%	0.91C	300	[266]
SWCNT	1132	44.2%	0.19%	0.2C	300	[229]
MWCNT	1073	47%	0.14%	1.0C	300	[267]
MWCNT/PEG	1206	52%	0.16%	0.2C	300	[268]
Microporous carbon/PEG	1307	45%	0.11%	0.2C	500	[269]
Carbon nanofiber	1270	74%	0.13%	0.5C	200	[182]
Carbon	1386	60%	0.20%	0.2C	200	[178]
Carbon paper	1176	85%	0.15%	1.0C	100	[270]
Carbon black	1350	55%	0.09%	0.2C	500	[271]
N-porous carbon/PP	882	88%	0.024%	1.0C	500	[272]
N-doped-carbon nanowire	1123	60%	0.08%	0.2C	500	[273]
Cobalt/nitrogen co-doped carbon nanofibers	865	71.2%	0.06%	0.2C	500	[274]
C_3N_4	1100	66%	0.07%	1.0C	500	[230]
TiO_2/graphene	700	80%	0.01%	2.0C	1000	[275]
TiO_2/CNTs	627	57.5%	0.17%	0.5C	250	[276]

TiO_2/C_{65}	1206	50.3%	0.1%	0.5C	500	[277]
TiO_2/TiN	927	67%	0.017%	1.0C	2000	[278]
TiN	880	63.6%	0.091%	1.0C	400	[279]
NbN	815	75.8%	0.061%	1.0C	300	[280]
V_2O_5	880	91.2%	0.035%	0.0667C	250	[189]
V_2O_5/carbon nanofiber	1400	28.5%	0.07%	3.0C	1000	[231]
Al_2O_3	967	61.5%	0.77%	0.2C	50	[188]
Al_2O_3/graphene	1067.7	75%	0.25%	0.2C	100	[225]
Al_2O_3/CNT	1287	63%	0.37%	0.2C	100	[190]
Li@Nafion/PEP/Al_2O_3	924	77.2%	0.022%	1.0C	1000	[281]
SnO_2	622	68%	0.064%	0.2C	500	[232]
Co_9S_8	986	83.1%	0.011%	1.0C	1500	[282]
$Li_4Ti_5O_{12}$/graphene	813.3	85.7%	0.03%	1.0C	500	[283]
PEDOT:PSS	748	64.3%	0.0714%	1.0C	500	[284]
MoS_2	808	50%	0.083%	0.5C	600	[223]
MoS_2/CNTs	1237	52.4%	0.061	0.5C	500	[285]
MOF/CNTs	1101	50%	0.165%	0.25C	300	[286]
MOF/GO	612	71%	0.019%	1.0C	1500	[158]
MOF/SiO_2	1400	42.9%	0.57%	0.1C	100	[287]
Ce-MOFs/CNT/PP	1021	82%	0.022%	1.0C	800	[288]
$Ni_3(HITP)_2$/PP	851	84.1%	0.032%	1.0C	500	[289]
Ti_3C_2/CNTs	1240	51.6%	0.043%	0.5C	1200	[233]
MnO_2/graphene/CNTs	829	27.5%	0.029%	1.0C	2500	[290]
NiFe/N-doped graphene	812	40%	0.06%	2.0C	1000	[187]
Glass fiber	630	80%	0.04%	0.5C	500	[291]
Red phosphorus/PP	889	82%	0.036%	1.0C	500	[292]

Nafion	781	60%	0.08%	1.0C	500	[293]
Nafion/GO	1057	46%	0.18%	1.0C	300	[294]
PMIA	773.6	73%	0.045%	1.0C	600	[295]
PMIA	1121.5	63.5%	0.06%	0.5C	600	[296]
PD/PI	1404	63.4%	0.366%	0.5C	100	[297]
PAA	600	56%	0.074%	0.5C	600	[298]
PAH/PAA	1418	30%	1.4%	--	50	[186]
PAN/PMMA	1000	65%	0.175%	2.0C	200	[299]
PZI	940	88%	0.012%	1.0C	1000	[300]
Zn_2(benzimidazolate)$_2$ $(OH)_2$	1272	58%	0.2%	0.25C	200	[301]

Table 12 Comparison of electrochemical performance of the *np-ANF* membranes with that of recent publications in Li–S batteries with various separators in the case of high sulfur loadings more than 3 mg cm^{-2}

Separator Membrane	Cathode	Sulfur loading (mg cm^{-2})	Electrochemical Performance					REF
			Initial discharge capacity ($mAhg^{-1}$)	Initial areal capacity ($mAhcm^{-2}$)	Capacity fade per cycle (%)	Current density (1C = 1675 mA g^{-1})	Number of cycle	
np-ANF	*C/S*	*5.8*	*1018*	*5.9*	*0.085%*	*0.1 C*	*200*	
np-ANF	*C/S*	*5.8*	*945*	*5.5*	*0.066%*	*0.2 C*	*500*	
MoS_2-Polymer /Celgard	C/S	4.0	~800	~3.2	0.2%	1.0 C	400	[302]
Co_9S_8/Celgard	C/S	5.6	985	5.5	0.079%	0.1C	200	[303]
V_2O_5/graphene/ Celgard	C/S	5.5	~780	4.3	~0.102 %	0.1C	100	[304]
Red phosphorus/PP	C/S	5.0	620	3.1	0.194%	0.3C	100	[292]
Co/NCNS/CNT/ Celgard	C/S	5.0	1134	5.67	0.108%	1.0 C	500	[305]
C_3N_4/Celgard	C/S	5.0	1134	5.11	0.51%	0.1C	40	[306]
NbN/PP	C/S	4.0	815	3.3	0.08%	1.0C	300	[280]
MOF/PAN	rGO/S	7.7	1102	8.5	0.17%	0.2C	50	[307]
Li@Nafion/PEP/Al_2O_3	rGO/S	7.6	1087	8.26	0.114%	0.2C	300	[281]
TiO_2/TiN/Celgard	Graphene /S	4.3	493	2.1	0.033%	1.0C	2000	[278]
N-porous carbon/PP	CNT/S	6.0	977	5.8	0.047%	0.5C	400	[272]
Cellulose nanofiber paper	CNT/S	3.0	~830	~2.5	0.05%	0.1C	200	[308]
$Ni_3(HITP)_2$/PP	CNT/S	8.0	1055	8.4	0.071%	0.5C	200	[289]
D-HVS/PP	Carbon nanofiber/ S	9.2	905	8.3	0.237%	0.2C	120	[309]
Ce-MOFs/CNT/PP	Carbon nanofiber/ S	6.0	993.5	5.9	0.054%	0.1C	200	[288]

MOF/PVDF	Carbon cloth/S	5.8	1269	7.46	0.13%	0.1C	200	[310]

Table 13 *The summary of comparative performance for Li-S batteries at high temperature*

Membrane	Cathode material	Operation temperature (℃)	Electrochemical Performance				Electrolyte (LiTFSI)	REF
			Initial discharge capacity ($mAhg^{-1}$)	Capacity fade per cycle (%)	Current density (1C = 1675 mA g^{-1})	Number of cycle		
np-ANF	*C/S*	*80*	*1346*	*0.15%*	*0.1C*	*100*	*(DOL+DME)*	
np-ANF	*C/S*	*80*	*801*	*0.081%*	*3C*	*500*	*(DOL+DME)*	
C@PI@LLZO	C/S	80	897.1	0.2%	5C	200	(DOL+DME)	[311]
CuNWs-GN/PI/LLZO	C/S	80	817.8	0.24%	$0.5Ag^{-1}$	50	(DOL+DME)	[234]
PAN@APP	C/S	75	~700	0.220%	1.0C	100	(DOL+DME)	[192]
Celgard^{TM} 2325	Carbon nanotube/S	70	~750	~0.444 %	2.0C	150	(DOL+DME)	[312]
Celgard^{TM} 2400	Graphene /BN-S	70	1032	0.047%	2.0C	300	(DOL+DME)	[313]
PE	S@pPAN	60	820.3	--	0.2C	200	(TEP+TTE)	[314]
Li@Nafion/PE/Al_2O_3	RGO@S	60	1172	0.059%	0.2C	500	(DOL+DME)	[281]
Celgard^{TM} 2400	Porous graphene/S	60	~590	0.297%	1.0C	80	(DOL+DME)	[315]
Celgard^{TM} 2400	Alucone coated C/S	55	1065	0.152%	0.1C	300	$LiPF_6$ (EC:DEC:EMC)	[316]
Celgard^{TM} 2400	S@CNTs/$Co_3S_4NB_s$	50	953	0.082%	0.2C	300	(DOL+DME)	[317]
CNT-COF	C/S	50	450	0.16%	$2.0Ag^{-1}$	300	(DOL+DME)	[318]
Celgard^{TM} 2400	Mesoporous C/S	45	~1180	~4.067 %	0.1C	10	(DOL:DME:BTFE)	[319]
Tonen polyolefin	C/S	45	-	0.770%	0.1C	50	(DOL+DME)	[320]

Table 14 *Multiparameter comparison with various modified separator for Li-S batteries in the form of glyph plots.*

	Discharge Capacity 0.1C ($mAhg^{-1}$)	**Discharge Capacity 1C ($mAhg^{-1}$)**	**Cycle number**	**Capacity Retention 1C (%)**	**CE (%)**	**Sulfur loading (mg/cm^2)**	**Operational Temperature (℃)**	**REF**
This work	*1268*	*889*	*1500*	*76*	*98*	*5.8*	*80*	
GO/Celgard	1403	1100	400	32	98	1.1	22	[219]
N-porous carbon/PP	1257	851	500	88	98	6.0	22	[272]
MWCNT/Celgard	1324	1073	300	47	99	1.2	22	[267]
Carbon paper/Celgard	1367	1176	100	85	96	1.2	22	[270]
MoS_2/Celgard	1300	1007	2000	42	98	4.0	22	[302]
Red phosphorus/PP	1200	889	500	82	99	5.0	22	[292]
Co_9S_8/Celgard	1360	986	1500	83	98	5.6	22	[282]
$Ni_3(HITP)_2$/PP	1186	879	500	84	99	8.0	22	[289]
MOF@GO	1072	612	1500	71	98	0.7	22	[158]
MnO_2/graphene/CNTs	1259	960	2500	27.5	99	2.37	22	[290]
PAN@APP	1310	815	400	77.8	99	1.8	75	[192]
Ce-MOFs/CNT/PP	1200	1021	800	82	99	6.0	22	[288]
Li@Nafion/PEP/Al_2O_3	1398	924	1000	77.2	99	7.6	60	[281]
PZI	1095	940	1000	85	99	5.8	25	[300]
$Li_4Ti_5O_{12}$/graphene/Celgard	1408	813	500	85	98	1.1	22	[283]
PEDOT:PSS	914	748	500	64.3	99	2.9	22	[284]
PMIA/Celgard	944	773	600	73	98	0.6	22	[295]
TiO_2/TiN/Celgard	1250	790	2000	85	99	4.3	22	[278]
NbN/Celgard	1400	815	300	81.7	99	4.0	22	[280]
Nafion/Celgard	960	718	500	60	98	0.53	22	[293]
C_3N_4/Celgard	1200	1100	500	66	99	5.0	22	[230]

Chapter 4

Bioinspired Quasi-Solid Electrolyte with Tunable Porosity

4.1 **Abstract**

Among beyond Li-ion chemistries, Li-S batteries have been widely investigated because of their high theoretical energy density, low cost, and environment-friendliness. However, polysulfide shuttle and dendrite formation limit practical applications of Li-S batteries. We present a selectively permeable quasi solid electrolyte from ANF, Lithium bis(trifluoromethanesulphonyl)imide (LiTFSI), and PVA (ALPS) composites inspired by biological filtration mechanisms, namely glomerular basement membrane (GBM). The 3D network and related properties of ALPS are designed with the help of 3D graph theory, where the filaments are denoted as edges and junctions are represented as nodes. With tunable pore size and selective permeability, ALPS suppress dendrite formation and polysulfide shuttle while providing a passage for Li-ion with high tortuosity. Polysulfide blocking and dendrite suppression cooperatively provided a high initial capacity of 1482 mAh g^{-1} at 0.1C. This bioinspired model can be modified and extended for various high energy density applications, including but not limited to portable medical electronics, electric vehicles (EVs), and unmanned air vehicles (UAVs).

4.2 Introduction

The high theoretical specific energy density (2600Wh/kg) and high specific capacity (1675mA/g), along with the natural abundance and low toxicity of sulfur, have been attracting significant attention for the development of an alternative battery system to replace traditional Li-ion batteries which suffer from safety and capacity/energy density limitations in various applications. There are at least two significant hurdles on the way to the realization of the potential of Li-S batteries. The first problem is that lithium-polysulfides (LiPS, Li_2S_x, $2<x<8$) are soluble in liquid electrolytes and migrate to the anode, where they form a passivating layer obstructing cell performance. The second problem is the growth of Li dendrites, which will penetrate through the ion-conducting membranes separating anodes and cathodes (aka separators). Both issues lead to the irreversible loss of active material, low Coulombic Efficiency, and short cycle life. Despite many significant achievements over the last ten years of intense research on Li-S batteries, the practical resolution of these problems remains vague.

Physical confinement of LiPS using carbonaceous materials has been extensively used to resolve this problem by retaining them in the nanostructured pores in the cathodes[165], [184], [329], [330], [321]–[328]. Graphene nanosheets[331], [332], or conductive polymers[333] were also used to envelope sulfur particles. Along with suppressing the LiPS leakage from cathodes, these carbonaceous materials function as additional electron conduction and pathways, partially enhancing the cycling performance of Li-S batteries. However, Li-S cell cathodes made from non-polar carbonaceous hosts still generally suffer from rapid capacity fading over long-term cycling (>300 cycles) because the relatively weak intermolecular interaction between the non-polar hydrophobic carbon and the more polar hydrophobic LiPS species is not sufficient to prevent diffusion of LiPS[321], [334]. Another approach to LiPS management is to block their transfer

from cathode to anode using structural design and coating of separators. This is accomplished by blocking interlayers between the cathode and anode containing LiPS absorbers such as metal oxides/sulfides/carbides/nitrides,[335]–[337] and functional polymers[338]. These layers are deposited on conventional separators (e.g., Celgard^{TM}) and restrain LiPS diffusion by physical adsorption between the barrier layers and polysulfides[339], [340]. The molecular design of pores in the separators enables their ion-selectivity in ion-transport. For example, ion-selective Nafion-based membrane rejects the passage of negative ions of LiPS due to the electrostatic repulsion[341], [342]. The Li-S cell with the Nafion-based separator showed a cycling decay of 0.08% per cycle within 500 cycles at a current density of 1C. Similar strategies have been proposed for LiPS trapping by separators with Al_2O_3[188] and metal-organic framework (MOF)[172], [343], [344] coatings. When a typical 70 wt% sulfur-containing mesoporous carbon composite was used as the cathode material, the Li–S cell with a MOF-based separator achieved a low capacity decay rate of 0.019% per cycle over 1500 cycles at a rate of 1C, and there is almost no capacity fading after the initial 100 cycles[343].

Several approaches have been taken to reduce the dendrite growth of lithium and other dendrites. These methods include the utilization of a variety of dendrite suppressing additives and electrolytes. Considering the stringent weight and safety requirements of batteries, these measures are unlikely to be sufficient for EVs. The utilization of separators with high stiffness effectively suppresses the growth of dendrites. This strategy, again, encounters the fundamental materials bottleneck with combining transport and mechanical properties. For example, polyacrylonitrile (PAN) separators can suppress the formation of lithium dendrites due to their high modulus of 3–4 GPa[345]. However, it was not possible to realize a EV-suitable Li-S battery with such separators due to slow ion transport. Design approaches for preparing materials with high ion conductivity,

and high stiffness have also included nanocomposites that provided diverse opportunities to manipulate the pore structure and mechanics of the separators. The nanoscale composites based on Al_2O_3/UV-cured ethoxylated trimethylolpropane triacrylate (ETPTA),[346] POSS/PEG,[260] and SiO2/diglycidyl ether of bisphenol A (DGEBA)/polyetheramine,[347] have been made, but none of them were eventually suitable for Li-S batteries.

Out-of-box approaches to engineering materials are needed to address this fundamental challenge. Here, we design and implement a new generation of aramid nanofiber (ANF) composite separators that effectively suppress LiPS poisoning and dendrite growth on anodes in Li-S batteries, enabling Li-S batteries combining high energy density and long cycle life – a concept inspired by the glomerular basement membrane which consists of laminin, type IV collagen, nidogen, and heparan sulfate proteoglycan[348]. We present a facile technique to produce ANF-separator with tunable ANF/PVA ratios for the structural reorganization of composite separators to optimize tortuosity and the pore structures. Notably, ANF-PVA composites replicate the composition of cartilage[349] but using inexpensive abiotic compounds. ANF mimics the stiff collagen nanofibers of cartilage, while PVA mimics the soft polymeric component of cartilage represented by proteoglycans. Likewise, natural filters such as the glomerular basal membrane (GBM), a specialized extracellular matrix between podocytes and endothelial cells, have a role in selective ion passage[348], [350], [351]. Like GBM, A 3D reconstruction of ANF, Lithium bis(trifluoromethanesulphonyl)imide (LiTFSI) and polyvinyl alcohol (PVA) (ALPS) offers the tunable pore size structure which confines the intermediate soluble polysulfides by electrochemical apertures rather than allowing them to diffuse to the lithium anode, while acted as ion-transfer sites for positively charged (Li^+) as well as negatively charged species ($TFSI^-$).

4.3 Results

We engineer structures that mimic biological pores and filtration mechanisms in ANF mesh, filled with PVA and lithium bis(trifluoromethanesulfonyl)imide (LiTFSI) **(Figure 4.1)**, which is a hydrophilic lithium salt. Our choice for selecting PVA as the soft component of ion conductive membrane includes its excellent miscibility in a variety of solvents and high ionic conductivity. We focus on the surroundings of the Li^+ ion, for which stable sites are expected to be located along the PVA chains. Hence the exact geometry of the ANF scaffold is of secondary importance, the most significant characteristic being the pore size and structure. In particular, pore size in ANF network decreases with the increased ratio of PVA, which might be due to the nanoporosity within the porous ANF and its tunable pore size that can be suitable for the PVA chains to entangle into the pores. Adding LiTFSI into the ANF/PVA dispersion further change average pore size by altering the 3D nanoarchitecture and introducing directionality to pores **(Figure S 40)**. 3D reconstructed ANF, LiTFSI, PVA separator, the so-called "ALPS", consists various sized pores and the pore size can be optimized by changing the PVA ratio to obtain ALPS with excellent textural parameters. The excellent structural integrity well retains the high ionic conductivity and large specific surface area as well as high flexibility and strength of ANF **(Figure S 41, Figure S 42)**, together with tunable pore sizes and surface properties. The narrow size of nanopores in ANF-PVA composites combined with temperature resilience and strength of ANFs largely suppresses dendrite growth and block polysulfide species for lithium metal anodes.

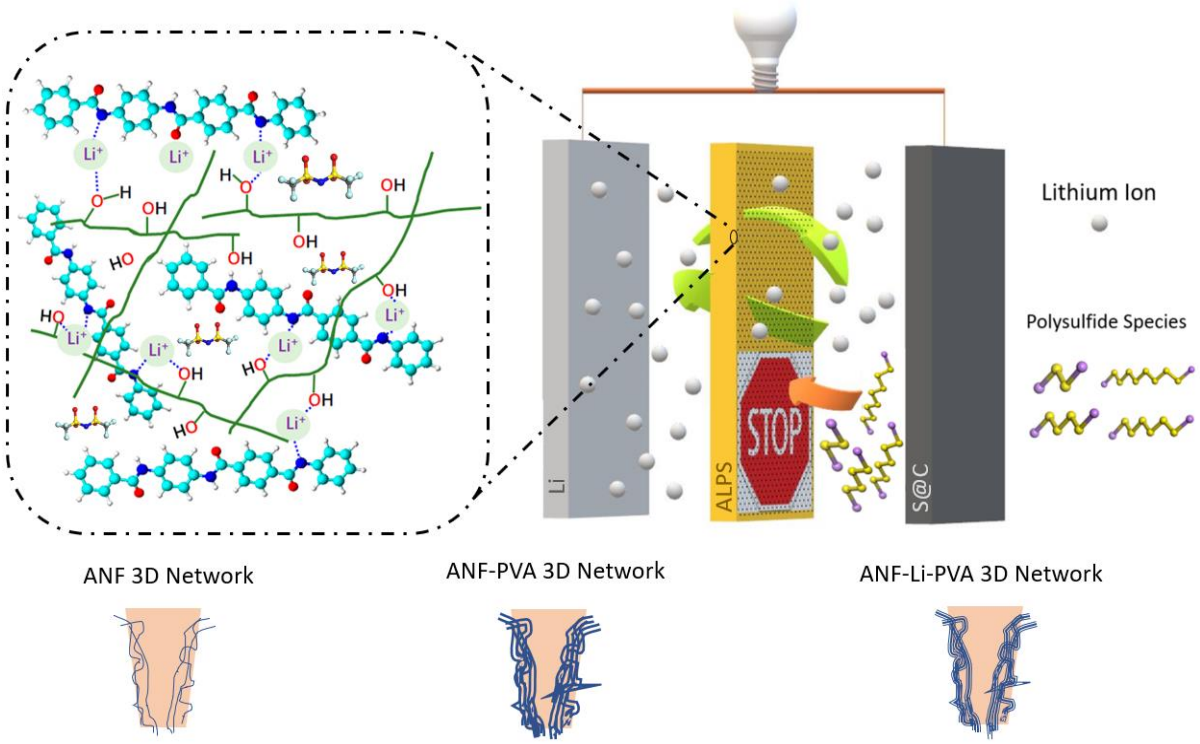

Figure 4.1: *Schematic illustration of interactions of ANF, PVA, and LiTSI with a simple vacuum-assisted filtration (VAF) fabrication method.*

The size of the pores will be significant structural parameters to be evaluated and controlled in these separator prototypes. Highly structural 3D network of load-bearing nanofibers can suppress the growth of the dendrites and provide sufficient space for the passage of lithium ions **(Figure 4.2 G-H)**. The tip of dendrites has a typical dimension of 20–80 nm **(Figure S 48)**.[25]

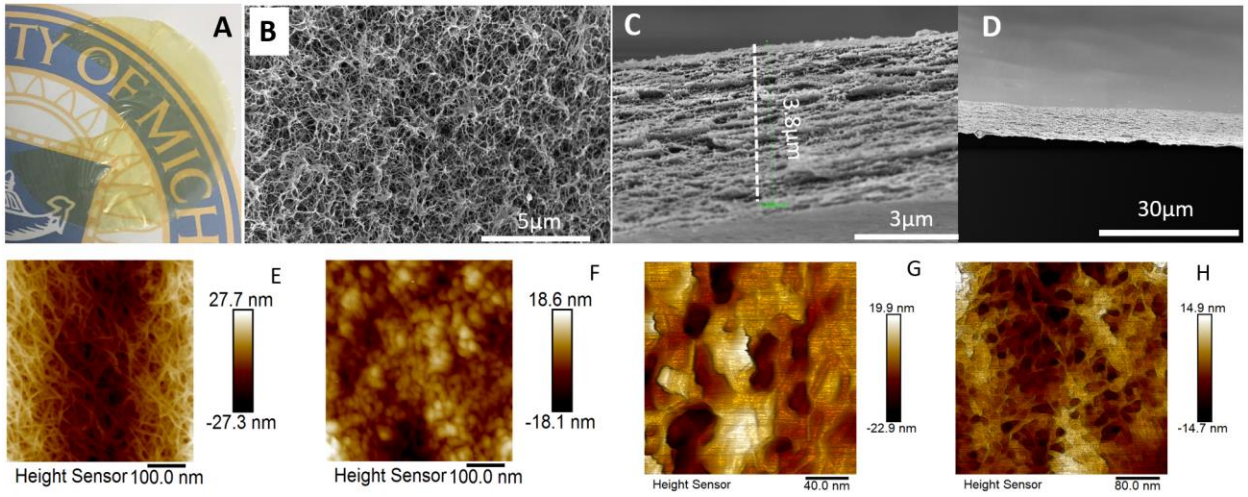

***Figure 4.2**: Characterization of ALPS (A) Optical Image of ALPS. (B-D) SEM Images of ALPS in different ANF-LiTFSI-PVA ratios. (E-F) AFM images of pure ANF vs ALPS. (F-G) AFM images of surface pores on ALPS.*

The pore size of the separator can be controlled by varying the amount of PVA used in the filtration process as increased PVA decreases pore size, indicating that the pores of ANF are partially filled with bead-like PVA chains **(Figure 4.2 E and F)**. The pore wall consisting of thin layers of PVA chains allows the narrow size of canonical nanopores with an average entrance size of ≈20 nm in ANF/PVA composite **(Figure 4.2 G and H)**. The smaller pores in the 3D network correlate with stronger obstruction of LiPS diffusion. ALPS′ smoothness indicates their uniform thickness of ~3.8 µm and structural homogeneity **(Figure 4.2 C and D)**. Moreover, ANF hinders crystallinity of PVA to contribute ionic conductivity **(Figure S 45)**. Atomic force microscopy images of ANF/PVA display a dense and uniform interconnecting network of thin nanoscale ANF, PVA polymer chains and integrated LiTFSI salt **(Figure 4.2 E and F)**. Inter and intra molecular H binding of ANF and PVA is shown around 3280/cm in FTIR spectra **(Figure S 46)**. Such morphology provides the structural prerequisites for combining diverse and opposing properties, including high ion conductance, stiffness, and efficient distribution of local strains as well as high

thermal stability **(Figure S 43-Figure S 44)**. Moreover, this unique combination also promotes electrolyte wetting of the separator for gel formation **(Figure S 47)**.

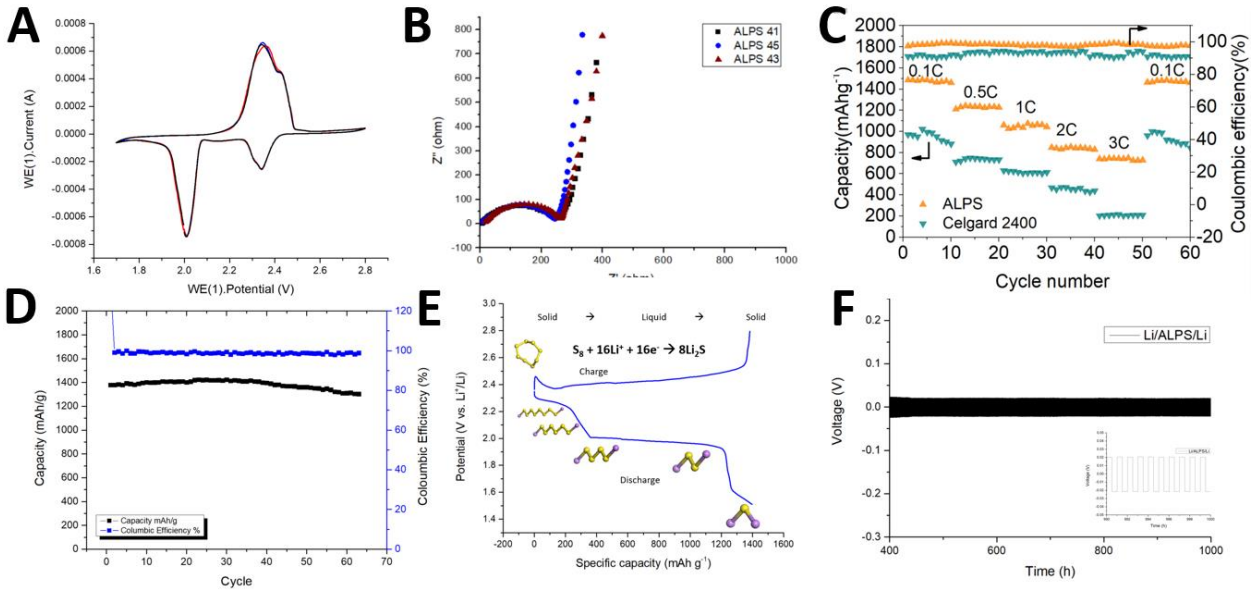

***Figure 4.3**: Electrochemical performance of the Li-S batteries with ALPS. (A) CV profiles with ALPS at a scan rate of 0.1mVs^{-1}; (B) Electrochemical impedance spectra of Li–S batteries. (C) Galvanostatic Charge Discharge Profiles at Various C-Rate (ranged from 0.1C to 3C with ALPS vs Celgard (D) Galvanostatic Charge Discharge Spectra at 0.2C; (E) Voltage Capacity Profile of ALPS (F) Stable cycling of Li//ALPS//Li cells.*

The cyclic voltammetry (CV) curves recorded at a scan rate of 0.1 mVs^{-1} **(Figure 4.3A)** show two sharp cathodic peaks and two continuous anodic peaks, in agreement with the discharge/charge voltage profiles. The Li-S cell exhibits almost overlapped CV curves for the initial three cycles, demonstrating the excellent reversibility of ALPS. The anodic peak which can be divided into two peaks at around 2.4 V is attributed to the conversion of lithium sulfides to polysulfides and lithium sulfur. The cathodic peak at around 2.0 V corresponds to the reduction of sulfur to higher order polysulfides (Li_2S_x, $4 \leq x \leq 8$), while the peak at approximately 2.3 V labeled as C is related to the reduction of higher-order polysulfides to lower-order polysulfides (such as Li_2S_4, Li_2S_3, Li_2S_2) and Li_2S.

Moreover, the ALPS cells having 5X salt (ALPS 45) possesses lower charge-transfer resistance **(Figure 4.3B)** than that of those having 1X (ALPS 41) and 3X (ALPS 43) salt, implying the improved electrochemical activity and fast Li/Li^+ redox kinetics of the ANF/PVA nanoarray structure.

Most importantly, even after prolonged cycling over 500 charge/discharge cycles at C/5, the cells using ALPS delivers reversible specific capacity above 1400 $mAhg^{-1}$ with 85% of their initial capacity retained, which corresponds to a small capacity decay of 0.03% per cycle. It is worth noting that the small fluctuations with cycling detected in the first 120 cycles could be attributed to the inhomogeneous distribution of polysulfides on the ALPS nanofiber network and the reactivation of lithium sulfides formed on the lithium anode owing to the lack of SEI protection during the initial charge process. The assembled ALPS cell can stably cycle with an average Coulombic efficiency of 99.98%. One can also notice that a competition between shuttle effect and capacity decay during charging could lead to a noticeable influence on the measurement, achieving Coulombic efficiency between 100% and 105% in the first several cycles.

The voltage profile of the cells using ALPS is shown in **Figure 4.3E**. Consistent with results from cyclic voltammetry, the discharge curve displays bi-stability corresponding to the conversion from long-chain polysulfides to short chain polysulfides (Li_2S_x, $4 \leq x \leq 8$) at around 2.0 V and the phase change from liquid Li_2S_4 to solid short-chain Li_2S_2 and Li_2S at around 2.3 V. The cells using ALPS show specific capacity of 190 $mAhg^{-1}$ between 2.3 and 2.0 V, confirming that reduction of Li_2S_8 to Li_2S_4 has high efficiency. Remarkably, the discharge capacity of the cells using ALPS was set as 1250 mAh/g at a current rate of C/2.

The cycling testing **(Figure 4.3C)** shows that the ALPS still helps improve the cycle stability of the battery. The average Coulombic efficiency of the cells using Celgard™ over 60

cycles was relatively low (~90%), which is caused by the local LiPS flux due to the much-decreased resistance across the conventional separator, creating "hot-spots" near the area of the pinhole for rough Li deposition on the lithium electrode. The ALPS improved the Coulombic efficiency significantly by 10% (~98%), which is likely due to the trapping of the LiPS by the separator with cartilage-like ANF/PVA nanofibrous composites that reduced the parasitic reactions within the coin cell components. The capacity can be recovered for both cells using ALPS and Celgard, respectively, and keeps almost steady in the subsequent 60 charge-discharge cycles in both cases, confirming good cyclability. **Figure 4.3C** also shows the excellent rate capability of the ALPS cell compared with the Celgard^{TM} counterparts, further demonstrating the robustness of ANF separators. The ALPS cells retain ~750 mAh g^{-1} even at the high rate of 3C.

Figure 4.4: *Prototypes Powered by Pouch Cells with ALPS. (A) Nail Penetration Test. (B) Health Monitoring Device (Apple Watch). (C) Robotic Prosthetic developed by Rouse Group (https://opensourceleg.com/). (D) 60 pouch cells covered hood of Nissan Leaf.*

As a proof of concept for the utilization of ALPS for structural energy storage needs, we fabricated pouch cells and conducted standard safety tests, including nail penetration test (**Figure 4.4A**) and then the cells into Apple watch (**Figure 4.4B**), robotic prosthetics (**Figure 4.4C**) and Nissan Leaf (**Figure 4.4D**). Pouch cells did not catch fire and did not even lose functionality after nail penetration due to the high mechanical properties and thermal stability of ALPS.

4.4 Conclusion

Inspired by extracellular matrix of kidney filtration system, glomerular basement membrane, 3D reconstruction of ANF composites along with tunable pore size cooperatively suppress dendrite formation and polysulfide shuttle while preventing any detrimental effect on efficient lithium-ion transport between electrodes. Ability to modify pore size and porosity along with high mechanical and thermal stability make quasi solid ALPS a safe alternative to current solid, liquid electrolytes by addressing challenges such as the risk of fire originating from liquid, flammable electrolyte leakage or rigidity and volume expansion.

4.5 Experimental Method

4.5.1 Preparation of the ANF and ALPS.

As previously reported, 1 g of Kevlar 69 (from Thread Exchange) and 1.5 g KOH were mixed in 500 mL of dimethyl sulfoxide (DMSO for two weeks at room temperature resulting in a dark red solution of ANF. Simultaneously, 2gr PVA was dissolved in DMSO at 90°C for 2 hours before mixing with 1M LiTFSI in DME:DOL (1:1). Chemicals were purchased from Sigma Aldrich without further purification.

4.5.2 Structural Characterization

The morphology of ALPS and Li dendrite were inspected with a scanning electron microscope (SEM, TFS Helios 650 Nanolab SEM/FIB), and Bruker Atomic Force Microscopy. Rigaku XRD and Thermo Fisher FTIR instruments are used to understand crystallinity and interaction between copolymers. Pore structure is analyzed by Leica STED Microscopy with the following method:

Labeling: 10ug/mL Abberior STAR635-SE and 1.49mM DST (disuccinimidyl tartrate) were dissolved in DMSO. The sample membrane was placed in this labeling solution overnight at room temperature. The ANF surfaces contain dense free secondary amines. The dye's succinimidyl ester reacts with these amine groups, but at a relatively slow rate. Performing this reaction in DMSO (rather than the more typical alkaline aqueous solution used when labeling primary amines) slows the rate of hydrolysis of the succinimidyl ester, allowing the dye to bond to the fiber. The competes with the STAR635 for amine groups to prevent saturation and reduce the chances for self-quenching of the dye.

Fluorescent Imaging: STED super-resolution fluorescence microscopy was performed on a Leica SP8, with 635nm fluorescence excitation and 775nm depletion wavelength. Scan size and pixel resolution were adjusted to achieve approximately 20nm/pixel resolution, and axial slices were taken with 200nm intervals. We found samples could be imaged up to a depth of approximately 10um before scattering became prohibitive. STED images were further deconvolved with Huygens software.

4.5.3 Mechanical Tests

The mechanical tests of the membranes were performed on a TA XT Plus Texture Analyzer (Stable Micro Systems Ltd.) instrument at room temperature, with the test of longitudinal direction carried out at a rate of 2mm min^{-1}. The film was cut into rectangular strips of 20 mm × 5 mm. Hardness was tested by Bruker Nanointendation. The thermal stability of membrane was analyzed by TA Instruments Discovery thermogravimetric analyzer (TGA) with a temperature ramp to 700 at 10 °C min−1 in nitrogen at a flow rate of 30 mL min^{-1} and differential scanning calorimetry (DSC) with a temperature ramp to 500 at 10 °C min^{-1} in nitrogen at a flow rate of 30 mL min^{-1}.

4.5.4 Electrochemical Performance Tests

Standard 2032-coin cells (MTI) were used to evaluate the electrochemical performance of the lithium sulfur batteries. The C/S cathode was fabricated by following a typical melt-diffusion strategy. The conductive carbon and sulfur powder are mixed with a mass ratio of 3:6 by milling and stirred at 155 °C for 10 hours to allow Sulfur transition in Carbon pores. The cathode slurry (sulfur/carbon and poly(vinylidene fluoride 9:1) was mixed in N-methylpyrrolidone (NMP) at 80℃ for 12 hours. The slurry is coated on Aluminum foil before drying at 60℃ in a vacuum oven for 24h. The resulting sulfur loading was about 1.2 mg cm^{-2}. The capacities were calculated based on the mass of sulfur in the cathode. 1M LiTFSI in DOL/DME (v/v = 1/1) was used during the fabrication of ALPS and electrolyte with the addition of $LiNO_3$. The cycle performance of assembled coin cells was tested in an Arbin battery cycler at various C-rates within a voltage range of 1.5-2.8 V. Pouch cells are made in a dry room. Both CV and EIS were performed on Metrohm Autolab (Autolab Potentiostat and Solartron 1260 frequency response analyzer). The CV was scanned between 1.7V and 2.8V at a speed of 0.1mV/s. The EIS was carried out from 100 kHz to 0.05 Hz with a potential amplitude of 20 mV. The resulting Nyquist plots were fitted to an equivalent circuit to find the R_b, and ionic conductivity is calculated by following the equation: $\sigma = L/R_bA$, where L is the thickness of the film, R_b is the bulk resistance, and A is the contact area of the membrane.

4.6 Supplementary Data

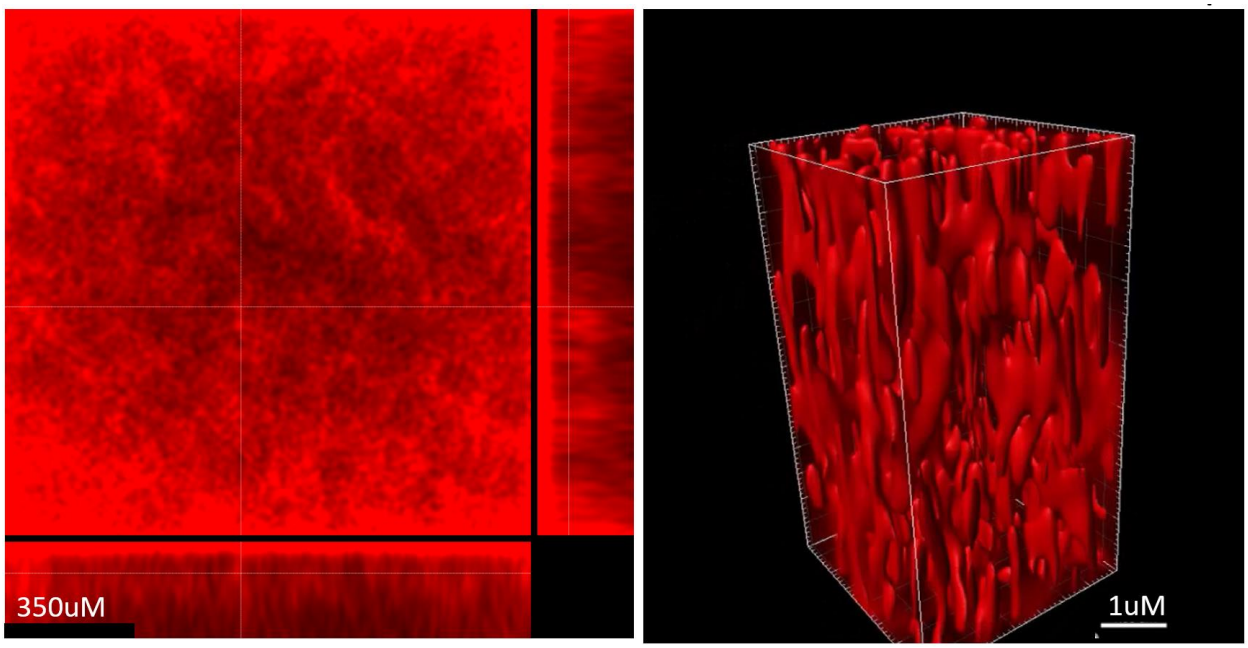

Figure S 40*: STED Image Reconstruction of ALPS 3D Structure*

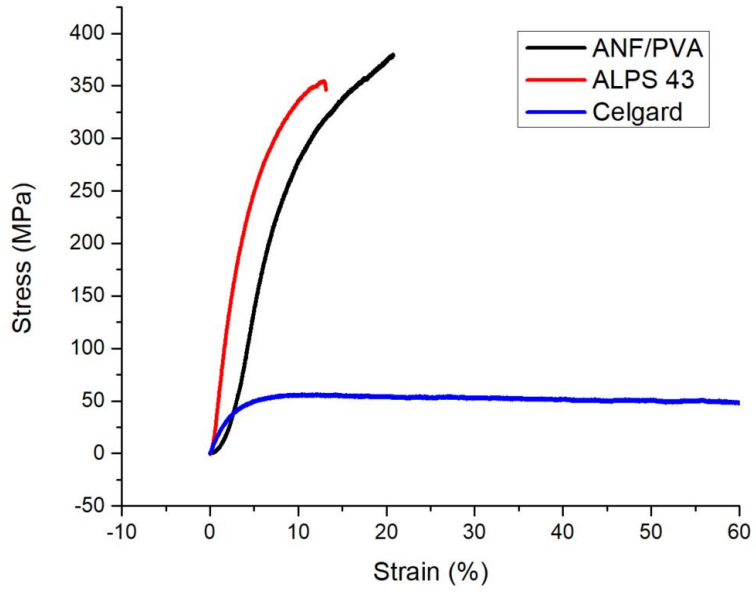

Figure S 41*: Stress-strain curves for ANF/PVA, ALPS43 and Celgard 2400.*

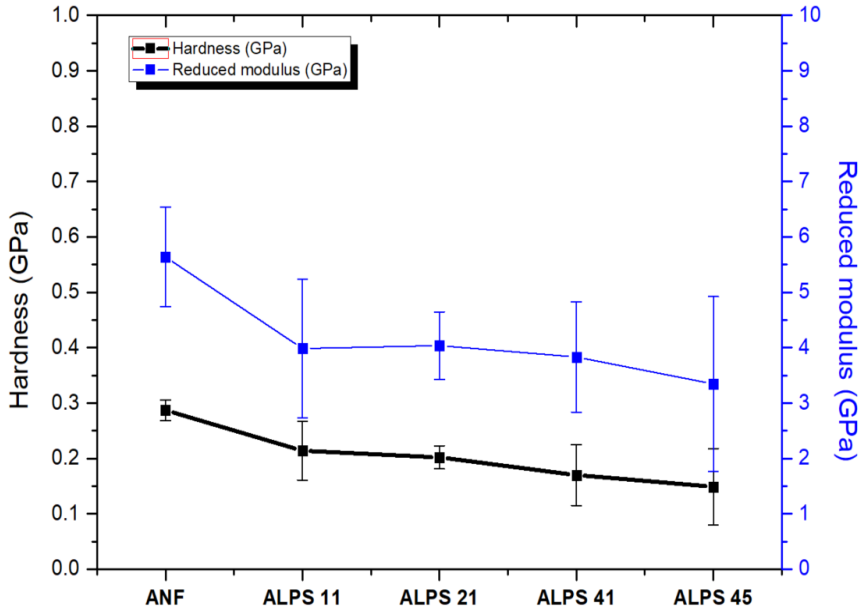

***Figure S 42**: Hardness and Reduced Modulus of ANF and ALPS with various PVA and LiTFSI ratios.*

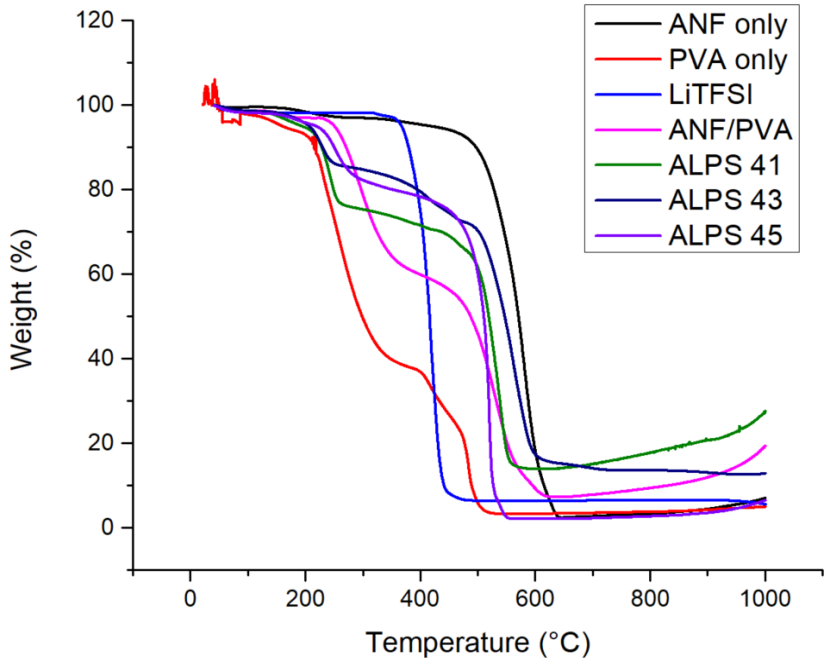

***Figure S 43**:Thermogravimetric analysis curves for ANF, PVA, ALPS and Celgard.*

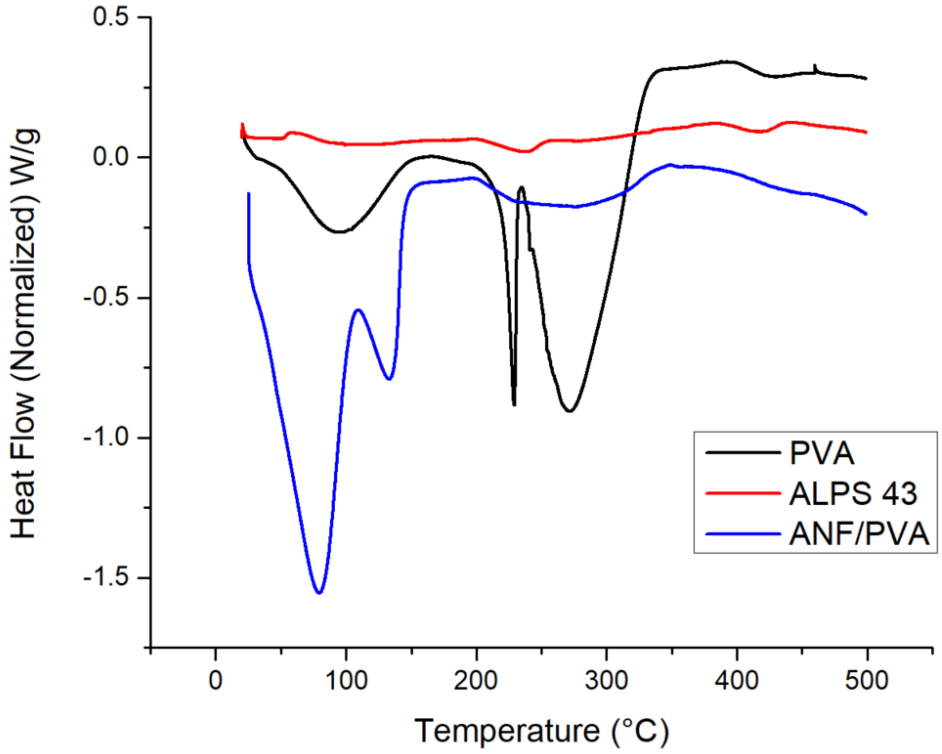

Figure S 44: *DSC curves comparison of PVA, ANF/PVA and ALPS. ALPS shows excellent thermal stability until 500°C.*

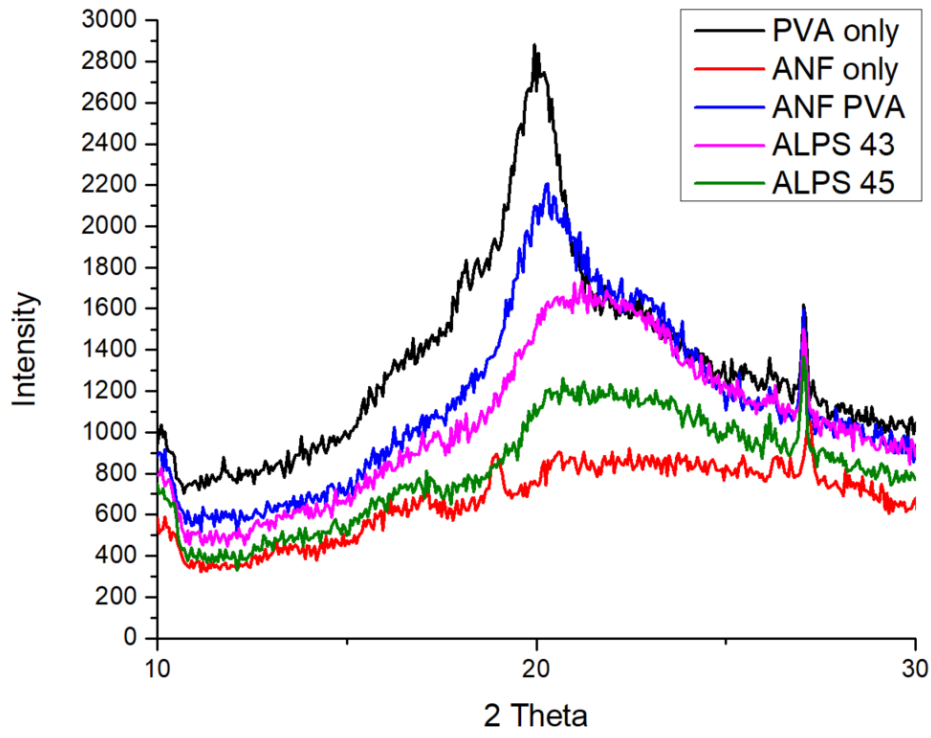

Figure S 45: *XRD Results of ANF, PVA, and ALPS. Crystallization of PVA was disrupted due to amphiphilicity of aramid surface and entanglement with ANF network and Li salt.*

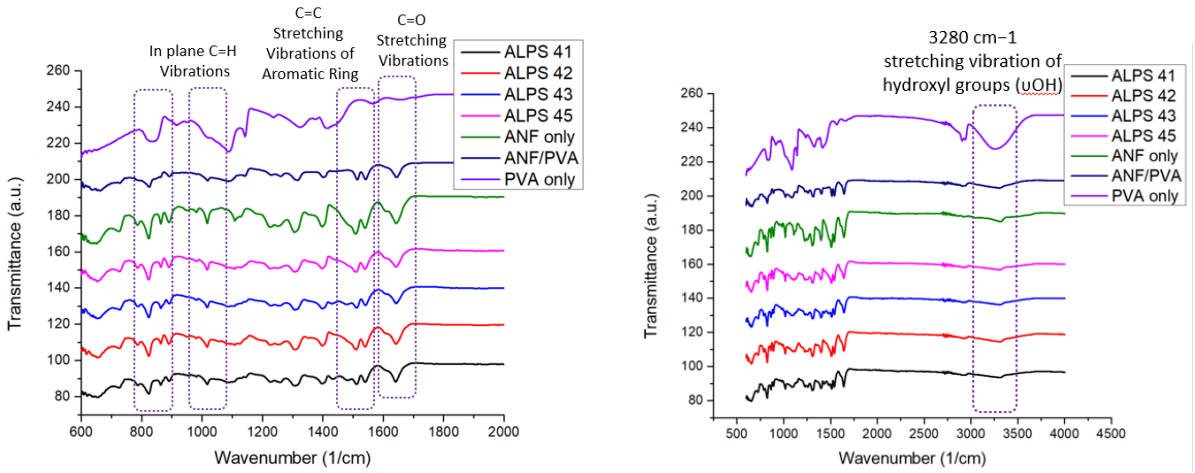

***Figure S 46**: FTIR Intermolecular and intramolecular H bonding interactions for PVA.*

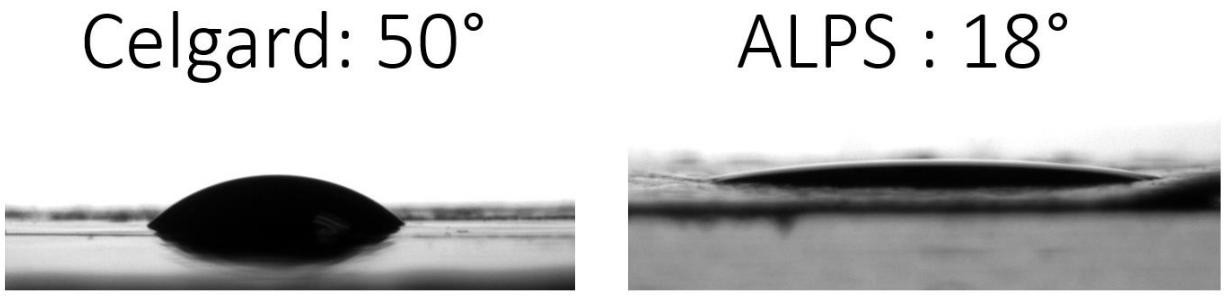

Figure S 47: *Contact Angle Test for Celgard and ALPS*

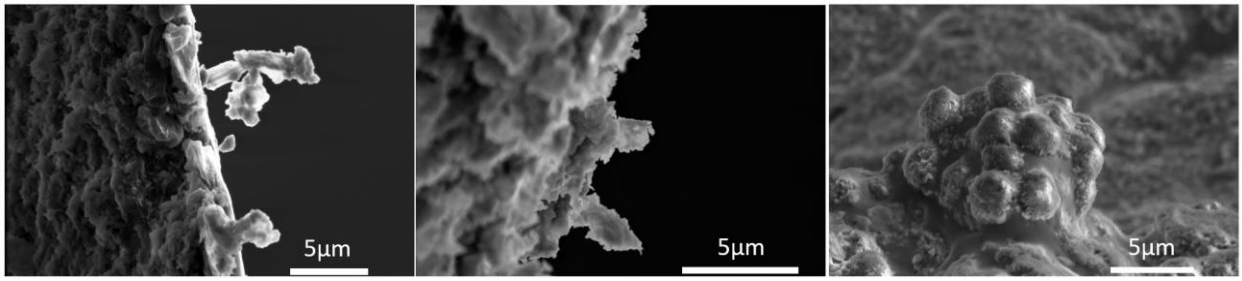

Figure S 48*: SEM Images of Lithium Dendrite*

Chapter 5
Conclusion

5.1 Summary and Overall Conclusion

In this dissertation, the potential use of bioinspired aramid nanocomposites for structural energy storage applications has been investigated. The aim was to combine high mechanical properties with high ion transport to enable safe, efficient structural batteries. Prototypes have been tested in various battery chemistries, including Zn-MnO_2 and Li-S and different structural energy storage applications from health monitoring devices, robotic prosthetics to EVs.

First, inspired by cartilage structure and function, we developed a novel solid electrolyte from ANF and PEO to address the poor cyclability of Zinc batteries originating from stiff zinc dendrites. High mechanical properties of ANF based PZB-931 successfully block dendrite formation and enable Coulombic efficiency of 96–100% after 50–100 charge–discharge cycles. We also integrated this battery into a UAV and successfully extended flight duration by ~20% depending on the original UAV battery capacity.

Mimicking ion channels in the cell membrane, we fabricated a nanoporous separator from ANF and PDDA LbL assembly to address dendrite formation and polysulfide shuttle in lithium sulfur batteries. 1nm of average pore size physically limits the passage of >2nm polysulfide species from cathode to the anode side and allows fast transport of Li-ion for efficient battery cycle. Negative surface charge density along with 1nm diameter physical barrier led +3500 cycles. Ion

flux in nanochannels is simulated in COMSOL for better visualization and understanding of underlying physics and chemistry.

Inspired by the natural filtration system, particularly basement membranes, we engineered an ion-selective gel membrane for lithium-sulfur batteries as a quasi-solid electrolyte from ANF and PVA. As pore size and porosity are central parameters in ion transport, engineering the 3D network of the membrane with desired properties is crucial. GT description assists in understanding the relationship between the 3D structure and material properties and guide us to fabricate desired architecture with required properties. Tuning pore size and porosity can modify ion transport rate and selectivity and enhance battery performance by minimizing parasitic reactions originating from undesired ion passage between electrodes. In addition, gel electrolyte enables structural utilization of lithium-sulfur batteries by addressing safety concerns such as the excess amount of flammable electrolyte. This also contributes to the battery cell's mechanical and thermal stability, increases performance at elevated temperatures, and provides safe functionality under extreme damage.

Overall, inspiring by nature and advancing by computational models (GT and COMSOL), engineering of multifunctional ANF nanocomposites can address common performance challenges and safety issues of zinc and lithium battery chemistries for realization of safe and efficient structural energy storage.

5.2 Future Work

The following future work is proposed to further reveal the uncovered potential of biomimetic ANF composites for addressing challenges in various energy storage platforms due to high mechanical and thermal stability.

5.2.1 Further Understanding the Relationship between 3D Network Structure and Properties by 3D Graph Theory

We are currently utilizing GT for the 2D analysis of nanofibers. To have a more realistic quantitative analysis, 3D GT needs to be further improved to help us understand the relationship between material 3D geometry and property.

5.2.2 Addressing Fast Charge Problem in Portable Electronics and Electric Vehicles

Environmental concerns, limited availability, rising cost, and increasing demand in the chemical industry necessitate reduced use of fossil fuels in transportation. Sustainable energy sources and efficient storage systems have been utilized to reduce the carbon footprint by switching to electric vehicles (EVs)[352]. However, limited range and long charging times hamper the widespread adoption of EVs compared to traditional gasoline-based cars. The urgent need for fast charging batteries, ideally charging to more than 80% in less than 15 minutes with greater than 500 cycles, requires a dedicated research effort.

Lithium-ion chemistries have recently attracted considerable attention for EV applications owing to their higher energy density and fast charging potentials. The high theoretical specific energy density (2600 Wh/kg) and high specific capacity (1675 mA/g), along with the natural abundance and environmental friendliness of lithium-sulfur (LiS) batteries, make them a great candidate for fast charging and safe driving EVs [156], [353]. However, the diffusion of lithium polysulfides (LPS, Li_2S_X, $4 \leq x \leq 8$) [157] from cathode to anode drastically reduces their cycle life, overall capacity, and Coulombic efficiency [158]–[161]. Additionally, LPS layers passivate both electrodes, leading to a significant increase in impedance and energy loss [162]. The non-uniform surface layer of anodes promotes plating and dendrite growth on the lithium surface, representing another challenge for Li-S batteries; dendrite growth is known to cause short-

circuiting and overheating a condition which is exacerbated with increasing charge rates. Thus, the lack of efficient, selectively permeable, and robust ion conductors (>10^{-3} S/cm) has been a significant shortcoming hampering the realization of fast and safe charging EVs.

Emerging ceramics-based solid-state electrolytes are considered the current benchmark for ion-conducting membranes; however, their brittleness and low interlayer contact lead to significant safety and performance issues., the sulfur cathode of Li-S batteries dissolution of lithium sulfide in organic liquid electrolytes during the electrochemical process also pose safety risks related to fast-charging energy storage. The high mechanical properties of ANF composites will also suppress Li dendrite formation, increasing battery stability and performance. We expect to reach current densities >10mA/cm^2 and areal capacities >10mAh/cm^2, thereby reducing EVs charging time by at least two times. The combined development of computational models and ANF materials with engineered ion channels will also open the door for optimization of ion-selective membranes for other types of batteries in the future too.

5.2.3 Utilization of ANF Ceramic Solid-State Electrolyte for Li Metal and NMC Batteries

The market for Li Metal and NMC batteries is growing due to their widespread use in EVs. To address the challenges of high ionic conductivity and mechanical and thermal stability, ceramic embedded ANF can be used as a solid-state electrolyte to address the dendrite formation problem of Li metal and the stability issue of Ni-rich NMC cathode chemistries. While ANF scaffold provides a flexible host, ceramic particles provide high ionic conductance, and this combination has a great potential to achieve the DOD's Battery 500 targets (i.e., 500Wh/kg energy density).

Bibliography

[1] F. Duffner, N. Kronemeyer, J. Tübke, J. Leker, M. Winter, and R. Schmuch, "Post-lithium-ion battery cell production and its compatibility with lithium-ion cell production infrastructure," *Nat. Energy*, vol. 6, no. 2, pp. 123–134, Feb. 2021, doi: 10.1038/s41560-020-00748-8.

[2] A. D. B. L. Ferreira, P. R. O. Nóvoa, and A. T. Marques, "Multifunctional Material Systems: A state-of-the-art review," *Compos. Struct.*, vol. 151, pp. 3–35, Sep. 2016, doi: 10.1016/j.compstruct.2016.01.028.

[3] C. González, J. J. Vilatela, J. M. Molina-Aldareguía, C. S. Lopes, and J. LLorca, "Structural composites for multifunctional applications: Current challenges and future trends," *Prog. Mater. Sci.*, vol. 89, pp. 194–251, Aug. 2017, doi: 10.1016/J.PMATSCI.2017.04.005.

[4] P. Ladpli, R. Nardari, F. Kopsaftopoulos, Y. Wang, and F.-K. Chang, "Design of Multifunctional Structural Batteries with Health Monitoring Capabilities," in *8th European Workshop on Structural Health Monitoring*, 2016, pp. 1–13.

[5] "Volvo Car Group makes conventional batteries a thing of the past," 2010. https://www.media.volvocars.com/global/en-gb/media/pressreleases/134235/volvo-car-group-makes-conventional-batteries-a-thing-of-the-past.

[6] L. E. Asp, S. Leijonmarck, and T. Carlson, "Realisation of Structural Battery Composite," *20th Int. Conf. Compos. Mater.*, no. July, pp. 19–24, 2015, doi: 10.13140/RG.2.1.2029.1922.

[7] M. Willgert, *Solid Polymer Lithium-Ion Conducting Electrolytes for Structural Batteries*, no. december. 2014.

[8] J. P. Thomas, "Multifunctional structure battery materials for enhanced performance in small unmanned air vehicles," 2003.

[9] W. K. Belvin, J. J. Watson, and S. N. Singhal, "Structural Concepts and Materials for Lunar Exploration Habitats," *Struct. Mater.*, no. September, pp. 1–15, 2006, doi: 10.2514/6.2006-7338.

[10] K. K. Sairajan, G. S. Aglietti, and K. M. Mani, "A review of multifunctional structure technology for aerospace applications," *Acta Astronautica*. 2016, doi: 10.1016/j.actaastro.2015.11.024.

[11] G. S. Aglietti, C. W. Schwingshackl, and S. C. Roberts, “Multifunctional structure technologies for satellite applications,” *Shock Vib. Dig.*, 2007, doi: 10.1177/0583102407077397.

[12] M. Armand, “Polymers with Ionic Conductivity,” *Advanced Materials*, vol. 2, no. 6–7. WILEY-VCH Verlag GmbH, pp. 278–286, Jun. 1990, doi: 10.1002/adma.19900020603.

[13] Y. Wang *et al.*, “Design principles for solid-state lithium superionic conductors,” *Nat. Mater.*, vol. 14, no. 10, pp. 1026–1031, Oct. 2015, doi: 10.1038/nmat4369.

[14] E. Jacques, M. H. Kjell, D. Zenkert, and G. Lindbergh, “The effect of lithium-intercalation on the mechanical properties of carbon fibres,” *Carbon N. Y.*, vol. 68, pp. 725–733, Mar. 2014, doi: 10.1016/j.carbon.2013.11.056.

[15] C. S. N. Shiau, C. Samaras, R. Hauffe, and J. J. Michalek, “Impact of battery weight and charging patterns on the economic and environmental benefits of plug-in hybrid vehicles,” *Energy Policy*, 2009, doi: 10.1016/j.enpol.2009.02.040.

[16] R. Steinegger, “Fuel Economy as Function of Weight and Distance,” *Zürcher Fachhochschule*, pp. 1–11, 2017.

[17] P. L. E. Asp and E. S. Greenhalgh, “Multifunctional composite materials for energy storage in structural load paths,” *Plast. Rubber Compos.*, 2013.

[18] L. E. Asp, M. Johansson, G. Lindbergh, J. Xu, and D. Zenkert, “Structural battery composites: a review,” *Funct. Compos. Struct.*, vol. 1, no. 4, p. 042001, Nov. 2019, doi: 10.1088/2631-6331/AB5571.

[19] L. E. Asp *et al.*, “A Structural Battery and its Multifunctional Performance,” *Adv. Energy Sustain. Res.*, vol. 2, no. 3, p. 2000093, Mar. 2021, doi: 10.1002/AESR.202000093.

[20] M. Yang *et al.*, “Dispersions of aramid nanofibers: A new nanoscale building block,” *ACS Nano*, vol. 5, no. 9, pp. 6945–6954, 2011, doi: 10.1021/nn2014003.

[21] A. M. W. Ellen M. Arruda, Keqin Cao, Carlos A. Pons Siepermann, Michael D. Thouless, Ryan M. Anderson, Nicholas A. Kotov, Ming Yang, “Synthesis and use of aramid nanofibers,” 2013.

[22] D. Tanner, J. a Fitzgerald, and B. R. Phillips, “The Kevlar Story -- an Advanced Materials Case Study,” *Angew. Chemie Int. Ed. English*, vol. 28, no. 5, pp. 649–654, 1989, doi: 10.1002/anie.198906491.

[23] H. G. Chae and S. Kumar, “Rigid-rod polymeric fibers,” *J. Appl. Polym. Sci.*, vol. 100, no. 1, pp. 791–802, 2006, doi: 10.1002/app.22680.

[24] F. Vollrath and D. P. Knight, “Liquid crystalline spinning of spider silk.,” *Nature*, vol. 410, no. 6828, pp. 541–8, 2001, doi: 10.1038/35069000.

[25] S.-O. Tung, S. Ho, M. Yang, R. Zhang, and N. A. Kotov, “A dendrite-suppressing composite ion conductor from aramid nanofibres.,” *Nat. Commun.*, vol. 6, no. 2015, p. 6152, 2015, doi: 10.1038/ncomms7152.

[26] G. Decher, “Fuzzy Nanoassemblies: Toward Layered Polymeric Multicomposites,” *Science (80-.).*, vol. 277, no. 5330, pp. 1232–1237, 1997, doi: 10.1126/science.277.5330.1232.

[27] B. S. Shim *et al.*, “Multiparameter structural optimization of single-walled carbon nanotube composites: Toward record strength, stiffness, and toughness,” *ACS Nano*, vol. 3, no. 7, pp. 1711–1722, 2009, doi: 10.1021/nn9002743.

[28] A. Patel *et al.*, “High Modulus, Thermally Stable, and Self-Extinguishing Aramid Nanofiber Separators,” *ACS Appl. Mater. Interfaces*, vol. 12, no. 23, pp. 25756–25766, Jun. 2020, doi: 10.1021/ACSAMI.0C03671.

[29] M. Wang *et al.*, “Biomimetic Solid-State Zn2+ Electrolyte for Corrugated Structural Batteries,” *ACS Nano*, 2019, doi: 10.1021/acsnano.8b05068.

[30] S. J. Eichhorn *et al.*, “Review: Current international research into cellulose nanofibres and nanocomposites,” *Journal of Materials Science*, vol. 45, no. 1. pp. 1–33, 2010, doi: 10.1007/s10853-009-3874-0.

[31] M. a. Hubbe, O. J. Rojas, L. a. Lucia, and M. Sain, “Cellulosic Nanocomposites: a Review,” *BioResources*, vol. 3, no. 3, pp. 929–980, 2008, doi: 10.15376/biores.3.3.929-980.

[32] S. J. Eichhorn, “Cellulose nanowhiskers: promising materials for advanced applications,” *Soft Matter*, vol. 7, no. 2, p. 303, 2011, doi: 10.1039/c0sm00142b.

[33] P. Podsiadlo, Z. Tang, B. S. Shim, and N. A. Kotov, “Counterintuitive effect of molecular strength and role of molecular rigidity on mechanical properties of layer-by-layer assembled nanocomposites,” *Nano Lett.*, vol. 7, no. 5, pp. 1224–1231, 2007, doi: 10.1021/nl0700649.

[34] E. D. Cranston *et al.*, “Determination of Young’s modulus for nanofibrillated cellulose multilayer thin films using buckling mechanics,” *Biomacromolecules*, vol. 12, no. 4, pp. 961–969, 2011, doi: 10.1021/bm101330w.

[35] P. Chen, Y. S. Yun, H. Bak, S. Y. Cho, and H.-J. Jin, “Multiwalled Carbon Nanotubes-Embedded Electrospun Bacterial Cellulose Nanofibers,” *Mol. Cryst. Liq. Cryst.*, vol. 519, no. 1, pp. 169–178, 2010, doi: 10.1080/15421401003613659.

[36] P. Lu and Y. Lo Hsieh, “Multiwalled carbon nanotube (MWCNT) reinforced cellulose fibers by electrospinning,” *ACS Appl. Mater. Interfaces*, vol. 2, no. 8, pp. 2413–2420, 2010, doi: 10.1021/am1004128.

[37] B. Yang, L. Wang, M. Zhang, W. Li, Q. Zhou, and L. Zhong, “Advanced separators based

on aramid nanofiber (ANF) membranes for lithium-ion batteries: a review of recent progress," *J. Mater. Chem. A*, vol. 9, no. 22, pp. 12923–12946, Jun. 2021, doi: 10.1039/D1TA03125B.

[38] C. K. Chan *et al.*, "High-performance lithium battery anodes using silicon nanowires," *Nat. Nanotechnol.*, vol. 3, no. 1, pp. 31–35, 2008, doi: DOI 10.1038/nnano.2007.411.

[39] J. M. Tarascon and M. Armand, "Issues and challenges facing rechargeable lithium batteries.," *Nature*, vol. 414, no. 6861, pp. 359–67, 2001, doi: 10.1038/35104644.

[40] S. Hu *et al.*, "Novel aramid nanofiber-coated polypropylene separators for lithium ion batteries," *J. Mater. Chem. A*, vol. 4, no. 9, pp. 3513–3526, Feb. 2016, doi: 10.1039/C5TA08694A.

[41] H. K. Gahunia and K. P. H. Pritzker, "Structure and function of articular cartilage," in *Articular Cartilage of the Knee: Health, Disease and Therapy*, Springer New York, 2020, pp. 3–70.

[42] C. Leclech, C. F. Natale, and A. I. Barakat, "The basement membrane as a structured surface – role in vascular health and disease," *J. Cell Sci.*, vol. 133, no. 18, Sep. 2021, doi: 10.1242/jcs.239889.

[43] L. Xu, X. Zhao, C. Xu, and N. A. Kotov, "Water-Rich Biomimetic Composites with Abiotic Self-Organizing Nanofiber Network," *Adv. Mater.*, 2017, doi: 10.1002/adma.201703343.

[44] D. A. Vecchio, S. H. Mahler, M. D. Hammig, and N. A. Kotov, "Structural Analysis of Nanoscale Network Materials Using Graph Theory," *ACS Nano*, vol. 11, p. 19, Jul. 2021, doi: 10.1021/ACSNANO.1C04711.

[45] M. Wang *et al.*, "Biomorphic structural batteries for robotics," *Sci. Robot.*, 2020, doi: 10.1126/SCIROBOTICS.ABA1912.

[46] Y. Khan, A. E. Ostfeld, C. M. Lochner, A. Pierre, and A. C. Arias, "Monitoring of Vital Signs with Flexible and Wearable Medical Devices," *Advanced Materials*, 2016.

[47] H. Zhang *et al.*, "Graph theoretical design of biomimetic aramid nanofiber composites as insulation coatings for implantable bioelectronics," *MRS Bull.*, Apr. 2021, doi: 10.1557/s43577-021-00071-x.

[48] M. Goldfarb, B. E. Lawson, and A. H. Shultz, "Realizing the Promise of Robotic Leg Prostheses," *Sci. Transl. Med.*, vol. 5, no. 210, pp. 210ps15-210ps15, Nov. 2013, doi: 10.1126/SCITRANSLMED.3007312.

[49] A. F. Azocar, L. M. Mooney, J.-F. Duval, A. M. Simon, L. J. Hargrove, and E. J. Rouse, "Design and clinical implementation of an open-source bionic leg," *Nat. Biomed. Eng. 2020 410*, vol. 4, no. 10, pp. 941–953, Oct. 2020, doi: 10.1038/s41551-020-00619-3.

[50] W. Sun *et al.*, “Zn/MnO2 Battery Chemistry With H+ and Zn2+ Coinsertion,” *J. Am. Chem. Soc.*, vol. 139, no. 29, pp. 9775–9778, Jul. 2017, doi: 10.1021/jacs.7b04471.

[51] Y. Li and H. Dai, “Recent advances in zinc–air batteries,” *Chem. Soc. Rev.*, vol. 43, no. 15, pp. 5257–5275, 2014, doi: 10.1039/C4CS00015C.

[52] X. Chen *et al.*, “Ultrathin Co3O4 layers with large contact area on carbon fibers as high-performance electrode for flexible zinc–air battery integrated with flexible display,” *Adv. Energy Mater.*, vol. 7, no. 18, pp. 1–11, 2017, doi: 10.1002/aenm.201700779.

[53] K. Kordesch, “Rechargwable alkaline manganese dioxide/zinc batteries,” *J. Power Sources*, vol. 51, pp. 61–78, 1994.

[54] B. Lee, H. R. Lee, H. Kim, K. Y. Chung, B. W. Cho, and S. H. Oh, “Elucidating the intercalation mechanism of zinc ions into α-MnO2 for rechargeable zinc batteries,” *Chem. Commun.*, vol. 51, no. 45, pp. 9265–9268, 2015, doi: 10.1039/C5CC02585K.

[55] B. Sajdl, K. Micka, and P. Krtil, “Study of the rechargeable manganese dioxide electrode,” *Electrochim. Acta*, vol. 40, no. 12, pp. 2005–2011, 1995, doi: 10.1016/0013-4686(94)E0163-T.

[56] K. Kordesch, J. Gsellmann, M. Peri, K. Tomaniwhger, and R. Chemelli, “The rechargeability of manganese dioxide in alkaline electrolyte,” *Electrochim. Acta*, no. 26, pp. 1495–1504, 1981.

[57] B. J. Hertzberg *et al.*, “Effect of Multiple Cation Electrolyte Mixtures on Rechargeable Zn-MnO2 Alkaline Battery,” *Chem. Mater.*, vol. 28, no. 13, pp. 4536–4545, 2016, doi: 10.1021/acs.chemmater.6b00232.

[58] Y. Shen and K. Kordesch, “Mechanism of capacity fade of Rechargeable Alkaline Manganese Dioxide Zinc cells,” *J. Power Sources*, vol. 87, no. 1, pp. 162–166, 2000, doi: 10.1016/S0378-7753(99)00476-0.

[59] F. R. Mclarnon and E. J. Cairns, “The secondary alkaline zinc electrode,” *J. Electrochem. Soc.*, vol. 138, no. 2, pp. 645–664, 1991, doi: 10.1149/1.2085653.

[60] K. E. K. Sun *et al.*, “Suppression of Dendrite Formation and Corrosion on Zinc Anode of Secondary Aqueous Batteries,” *ACS Appl. Mater. Interfaces*, vol. 9, no. 11, pp. 9681–9687, 2017, doi: 10.1021/acsami.6b16560.

[61] L. Cheng *et al.*, “Effect of surface microstructure on electrochemical performance of garnet solid electrolytes,” *ACS Appl. Mater. Interfaces*, vol. 7, no. 3, pp. 2073–2081, 2015, doi: 10.1021/am508111r.

[62] M. F. Lappert, P. P. Power, A. R. Sanger, and R. C. Srivastava, *Metal and Metalloid Amides: Syntheses, Structures, and Physical and Chemical Properties*. 1980.

[63] C. Xu, B. Li, H. Du, and F. Kang, “Energetic zinc ion chemistry: The rechargeable zinc

ion battery," *Angew. Chemie - Int. Ed.*, vol. 51, no. 4, pp. 933–935, 2012, doi: 10.1002/anie.201106307.

[64] H. Pan *et al.*, "Reversible aqueous zinc/manganese oxide energy storage from conversion reactions," *Nat. Energy*, vol. 1, no. 5, p. 16039, 2016, doi: 10.1038/nenergy.2016.39.

[65] D. Kundu, B. D. Adams, V. Duffort, S. H. Vajargah, and L. F. Nazar, "A high-capacity and long-life aqueous rechargeable zinc battery using a metal oxide intercalation cathode," *Nat. Energy*, vol. 1, no. 10, p. 16119, 2016, doi: 10.1038/nenergy.2016.119.

[66] N. Zhang *et al.*, "Cation-Deficient Spinel ZnMn2O4 Cathode in Zn(CF3SO3)2 Electrolyte for Rechargeable Aqueous Zn-Ion Battery," *J. Am. Chem. Soc.*, vol. 138, no. 39, pp. 12894–12901, 2016, doi: 10.1021/jacs.6b05958.

[67] S. D. Han *et al.*, "Origin of Electrochemical, Structural, and Transport Properties in Nonaqueous Zinc Electrolytes," *ACS Appl. Mater. Interfaces*, vol. 8, no. 5, pp. 3021–3031, 2016, doi: 10.1021/acsami.5b10024.

[68] X. Wang *et al.*, "An Aqueous Rechargeable Zn//Co3O4 Battery with High Energy Density and Good Cycling Behavior," *Adv. Mater.*, pp. 4904–4911, 2016, doi: 10.1002/adma.201505370.

[69] C. Yan *et al.*, "Stretchable silver-zinc batteries based on embedded nanowire elastic conductors," *Adv. Energy Mater.*, vol. 4, no. 5, pp. 1–6, 2014, doi: 10.1002/aenm.201301396.

[70] S. Higashi, S. W. Lee, J. S. Lee, K. Takechi, and Y. Cui, "Avoiding short circuits from zinc metal dendrites in anode by backside-plating configuration," *Nat. Commun.*, vol. 7, p. 11801, 2016, doi: 10.1038/ncomms11801.

[71] M. Valvo *et al.*, "Electrochemical elaboration of electrodes and electrolytes for 3D structured batteries," *J. Mater. Chem. A*, vol. 1, no. 32, p. 9281, Jul. 2013, doi: 10.1039/c3ta11921a.

[72] S. R. Kwon, J. Harris, T. Zhou, D. Loufakis, J. G. Boyd, and J. L. Lutkenhaus, "Mechanically Strong Graphene/Aramid Nanofiber Composite Electrodes for Structural Energy and Power," *ACS Nano*, vol. 11, no. 7, pp. 6682–6690, Jul. 2017, doi: 10.1021/acsnano.7b00790.

[73] J. F. Parker *et al.*, "Rechargeable nickel–3D zinc batteries: An energy-dense, safer alternative to lithium-ion," *Science (80-.).*, vol. 418, pp. 415–418, 2017.

[74] J. Liu *et al.*, "A flexible quasi-solid-state nickel–zinc battery with high energy and power densities based on 3D electrode design," *Adv. Mater.*, vol. 28, no. 39, pp. 8732–8739, 2016, doi: 10.1002/adma.201603038.

[75] R. C. Agrawal and G. P. Pandey, "Solid polymer electrolytes: materials designing and all-solid-state battery applications: an overview," *J. Phys. D. Appl. Phys.*, vol. 41, no. 22, p.

223001, 2008, doi: 10.1088/0022-3727/41/22/223001.

[76] H. Wu, D. Zhuo, D. Kong, and Y. Cui, “Improving battery safety by early detection of internal shorting with a bifunctional separator,” *Nat. Commun.*, vol. 5, p. 5193, 2014, doi: 10.1038/ncomms6193.

[77] G. Zheng, Y. Cui, E. Karabulut, L. Wågberg, H. Zhu, and L. Hu, “Nanostructured paper for flexible energy and electronic devices,” *MRS Bull.*, vol. 38, no. 4, pp. 320–325, 2013, doi: 10.1557/mrs.2013.59.

[78] M. Hamedi, E. Karabulut, A. Marais, A. Herland, G. Nyström, and L. Wågberg, “Nanocellulose Aerogels Functionalized by Rapid Layer-by-Layer Assembly for High Charge Storage and Beyond,” *Angew. Chemie Int. Ed.*, vol. 52, no. 46, pp. 12038–12042, Nov. 2013, doi: 10.1002/anie.201305137.

[79] J. Fu *et al.*, “A flexible solid-state electrolyte for wide-scale integration of rechargeable zinc–air batteries,” *Energy Environ. Sci.*, vol. 9, no. 2, pp. 663–670, 2016, doi: 10.1039/C5EE03404C.

[80] H. Li *et al.*, “An extremely safe and wearable solid-state zinc ion battery based on a hierarchical structured polymer electrolyte,” *Energy Environ. Sci.*, vol. 11, no. 4, pp. 941–951, Apr. 2018, doi: 10.1039/C7EE03232C.

[81] W. Liu *et al.*, “Enhancing ionic conductivity in composite polymer electrolytes with well-aligned ceramic nanowires,” *Nat. Energy*, vol. 2, no. 5, p. 17035, 2017, doi: 10.1038/nenergy.2017.35.

[82] F. Y. Cheng, J. Chen, X. L. Gou, and P. W. Shen, “High-Power Alkaline Zn-MnO2 Batteries Using γ-MnO2 Nanowires/Nanotubes and Electrolytic Zinc Powder,” *Adv. Mater.*, vol. 17, no. 22, pp. 2753–2756, Nov. 2005, doi: 10.1002/adma.200500663.

[83] K. T. Nam *et al.*, “Virus-enabled synthesis and assembly of nanowires for lithium ion battery electrodes.,” *Science*, vol. 312, no. 5775, pp. 885–8, May 2006, doi: 10.1126/science.1122716.

[84] P. Bhattacharya, M. Kota, D. H. Suh, K. C. Roh, and H. S. Park, “Biomimetic Spider-Web-Like Composites for Enhanced Rate Capability and Cycle Life of Lithium Ion Battery Anodes,” *Adv. Energy Mater.*, vol. 7, no. 17, Sep. 2017, doi: 10.1002/aenm.201700331.

[85] N. Chen *et al.*, “Biomimetic ant-nest ionogel electrolyte boosts the performance of dendrite-free lithium batteries,” *Energy Environ. Sci.*, vol. 10, no. 7, pp. 1660–1667, Jul. 2017, doi: 10.1039/C7EE00988G.

[86] C. Wang, H. Wu, Z. Chen, M. T. Mcdowell, Y. Cui, and Z. Bao, “Self-healing chemistry enables the stable operation of silicon microparticle anodes for high-energy lithium-ion batteries,” *Nat. Chem.*, vol. 5, no. 12, pp. 1042–1048, Dec. 2013, doi: 10.1038/nchem.1802.

[87] I. Kovalenko *et al.*, “A major constituent of brown algae for use in high-capacity Li-ion batteries.,” *Science (80-.).*, vol. 334, no. 6052, pp. 75–9, Oct. 2011, doi: 10.1126/science.1209150.

[88] J. Chen *et al.*, “One-pot synthesis of CdS nanocrystals hybridized with single-layer transition-metal dichalcogenide nanosheets for efficient photocatalytic hydrogen evolution,” *Angew. Chemie - Int. Ed.*, vol. 54, no. 4, pp. 1210–1214, 2015, doi: 10.1002/anie.201410172.

[89] S. on Tung, S. L. Fisher, N. A. Kotov, and L. T. Thompson, “Nanoporous aramid nanofibre separators for nonaqueous redox flow batteries,” *Nat. Commun.*, vol. 9, no. 1, p. 4193, 2018, doi: 10.1038/s41467-018-05752-x.

[90] X. L. Lu and V. C. Mow, “Biomechanics of articular cartilage and determination of material properties,” *Med. Sci. Sports Exerc.*, vol. 40, no. 2, pp. 193–199, 2008, doi: 10.1249/mss.0b013e31815cb1fc.

[91] F. T. Moutos, L. E. Freed, and F. Guilak, “A biomimetic three-dimensional woven composite scaffold for functional tissue engineering of cartilage.,” *Nat. Mater.*, vol. 6, no. 2, pp. 162–7, Feb. 2007, doi: 10.1038/nmat1822.

[92] R. Ma, D. Xiong, F. Miao, J. Zhang, and Y. Peng, “Novel PVP/PVA hydrogels for articular cartilage replacement,” *Mater. Sci. Eng. C*, vol. 29, no. 6, pp. 1979–1983, 2009, doi: 10.1016/j.msec.2009.03.010.

[93] Y. Meng *et al.*, “All-graphene core-sheath microfibers for all-solid-state, stretchable fibriform supercapacitors and wearable electronic textiles,” *Adv. Mater.*, vol. 25, no. 16, pp. 2326–2331, 2013, doi: 10.1002/adma.201300132.

[94] K. H. Choi, S. J. Cho, S. H. Kim, Y. H. Kwon, J. Y. Kim, and S. Y. Lee, “Thin, deformable, and safety-reinforced plastic crystal polymer electrolytes for high-performance flexible lithium-ion batteries,” *Adv. Funct. Mater.*, vol. 24, no. 1, pp. 44–52, 2014, doi: 10.1002/adfm.201301345.

[95] Z. S. Wu, Z. Liu, K. Parvez, X. Feng, and K. Müllen, “Ultrathin Printable Graphene Supercapacitors with AC Line-Filtering Performance,” *Adv. Mater.*, vol. 27, no. 24, pp. 3669–3675, 2015, doi: 10.1002/adma.201501208.

[96] N. Shirshova *et al.*, “Structural supercapacitor electrolytes based on bicontinuous ionic liquid–epoxy resin systems,” *J. Mater. Chem. A*, vol. 1, no. 48, p. 15300, Nov. 2013, doi: 10.1039/c3ta13163g.

[97] W. Johannisson *et al.*, “Multifunctional performance of a carbon fiber UD lamina electrode for structural batteries,” *Compos. Sci. Technol.*, vol. 168, pp. 81–87, Nov. 2018, doi: 10.1016/j.compscitech.2018.08.044.

[98] N. Ihrner, W. Johannisson, F. Sieland, D. Zenkert, and M. Johansson, “Structural lithium ion battery electrolytes via reaction induced phase-separation,” *J. Mater. Chem. A*, vol. 5,

no. 48, pp. 25652–25659, Dec. 2017, doi: 10.1039/c7ta04684g.

[99] G. M. Stone *et al.*, “Resolution of the Modulus versus Adhesion Dilemma in Solid Polymer Electrolytes for Rechargeable Lithium Metal Batteries,” *J. Electrochem. Soc.*, vol. 159, no. 3, pp. A222–A227, Jan. 2012, doi: 10.1149/2.030203jes.

[100] C. Monroe and J. Newman, “Dendrite Growth in Lithium/Polymer Systems A Propagation Model for Liquid Electrolytes under Galvanostatic Conditions,” *J. Electrochem. Soc.*, vol. 150, no. 10, pp. A1377–A1384, 2003, doi: 10.1149/1.1606686.

[101] G. Nyström, A. Marais, E. Karabulut, L. Wågberg, Y. Cui, and M. M. Hamedi, “Self-assembled three-dimensional and compressible interdigitated thin-film supercapacitors and batteries,” *Nat. Commun.*, vol. 6, p. 7259, May 2015, doi: 10.1038/ncomms8259.

[102] R. Pan *et al.*, “Thickness difference induced pore structure variations in cellulosic separators for lithium-ion batteries,” *Cellulose*, vol. 24, no. 7, pp. 2903–2911, Jul. 2017, doi: 10.1007/s10570-017-1312-z.

[103] E. Barannikova and M. Allen, “Solid-binding peptides as a biotemplate for Li-ion battery electrodes,” *Biophys. J.*, vol. 108, no. 2, p. 634a, Dec. 2017, doi: 10.1016/j.bpj.2014.11.3447.

[104] C. Guo, L. Zhou, and J. Lv, “Effects of expandable graphite and modified ammonium polyphosphate on the flame-retardant and mechanical properties of wood flour-polypropylene composites,” *Polym. Polym. Compos.*, vol. 21, no. 7, pp. 449–456, 2013, doi: 10.1002/app.

[105] M. Miyauchi *et al.*, “Conductive cable fibers with insulating surface prepared by coaxial electrospinning of multiwalled nanotubes and cellulose,” *Biomacromolecules*, vol. 11, no. 9, pp. 2440–2445, 2010, doi: 10.1021/bm1006129.

[106] F. Croce, G. B. Appetecchi, L. Persi, and B. Scrosati, “Nanocomposite polymer electrolytes for lithium batteries,” *Nature*, vol. 394, no. 6692, pp. 456–458, 1998, doi: 10.1038/28818.

[107] J. J. Moon *et al.*, “Interbilayer-crosslinked multilamellar vesicles as synthetic vaccines for potent humoral and cellular immune responses,” *Nat. Mater.*, vol. 10, no. 3, pp. 243–251, 2011, doi: 10.1038/nmat2960.

[108] X. Zhai, W. Wang, G. Zhang, and B. He, “Crystal pattern formation and transitions of PEO monolayers on solid substrates from nonequilibrium to near equilibrium,” *Macromolecules*, vol. 39, no. 1, pp. 324–329, 2006, doi: 10.1021/ma051624y.

[109] J. Jin, M. Song, and F. Pan, “A DSC study of effect of carbon nanotubes on crystallisation behaviour of poly(ethylene oxide),” *Thermochim. Acta*, vol. 456, no. 1, pp. 25–31, 2007, doi: 10.1016/j.tca.2007.02.003.

[110] C. M. Lochner, Y. Khan, A. Pierre, and A. C. (UC B. Arias, “All-organic optoelectronic

sensor for pulse oximetry.," *Nat. Commun.*, vol. 5, p. 5745, 2014, doi: 10.1038/ncomms6745.

[111] J. F. Parker *et al.*, "Rechargeable nickel-3D zinc batteries: An energy-dense, safer alternative to lithium-ion," *Science (80-.).*, vol. 356, no. 6336, pp. 415–418, 2017, doi: 10.1126/science.aak9991.

[112] P. Hiralal *et al.*, "Nanomaterial-enhanced all-solid flexible zinc-carbon batteries," *ACS Nano*, vol. 4, no. Copyright (C) 2011 American Chemical Society (ACS). All Rights Reserved., pp. 2730–2734, 2010, doi: 10.1021/nn901391q.

[113] K. (Kelvin) Fu *et al.*, "Flexible, solid-state, ion-conducting membrane with 3D garnet nanofiber networks for lithium batteries," *Proc. Natl. Acad. Sci.*, vol. 113, no. 26, pp. 7094–7099, 2016, doi: 10.1073/pnas.1600422113.

[114] I. Villaluenga *et al.*, "Compliant glass–polymer hybrid single ion-conducting electrolytes for lithium batteries," *Proc. Natl. Acad. Sci.*, vol. 113, no. 1, pp. 52–57, 2016, doi: 10.1073/pnas.1520394112.

[115] G. A. Nazri and G. Pistoia, *Lithium batteries: science and technology*. 2003.

[116] Y. Liu *et al.*, "Making Li-metal electrodes rechargeable by controlling the dendrite growth direction," *Nat. Energy*, vol. 2, no. June, p. 17083, 2017, doi: 10.1038/nenergy.2017.83.

[117] Y. Lu, M. Tikekar, R. Mohanty, K. Hendrickson, L. Ma, and L. A. Archer, "Stable cycling of lithium metal batteries using high transference number electrolytes," *Adv. Energy Mater.*, vol. 5, no. 9, p. 1402073, May 2015, doi: 10.1002/aenm.201402073.

[118] N. Shirshova *et al.*, "Structural composite supercapacitors," *Compos. Part A Appl. Sci. Manuf.*, vol. 46, pp. 96–107, Mar. 2013, doi: 10.1016/J.COMPOSITESA.2012.10.007.

[119] S. W. Lee *et al.*, "High-power lithium batteries from functionalized carbon-nanotube electrodes," *Nat. Nanotechnol.*, vol. 5, no. 7, pp. 531–537, 2010, doi: 10.1038/nnano.2010.116.

[120] A. A. Mamedov and N. A. Kotov, "Free-standing layer-by-layer assembled films of magnetite nanoparticles," *Langmuir*, vol. 16, no. 13, pp. 5530–5533, 2000, doi: 10.1021/la000560b.

[121] C. Jiang and V. V. Tsukruk, "Freestanding Nanostructures via Layer-by-Layer Assembly," *Adv. Mater.*, vol. 18, no. 7, pp. 829–840, Apr. 2006.

[122] M. H. Alfaruqi *et al.*, "Electrochemically induced structural transformation in a γ-MnO2 cathode of a high capacity Zinc-ion battery system," *Chem. Mater.*, vol. 27, no. 10, pp. 3609–3620, 2015, doi: 10.1021/cm504717p.

[123] Y. Yamada *et al.*, "Unusual stability of acetonitrile-based superconcentrated electrolytes for fast-charging lithium-ion batteries," *J. Am. Chem. Soc.*, vol. 136, pp. 5039–5046,

2014, doi: 10.1021/ja412807w.

[124] L. Suo, Y. S. Hu, H. Li, M. Armand, and L. Chen, “A new class of Solvent-in-Salt electrolyte for high-energy rechargeable metallic lithium batteries,” *Nat. Commun.*, vol. 4, p. 1481, 2013, doi: 10.1038/ncomms2513.

[125] W. Huang, R. Frech, and R. A. Wheeler, “Molecular structures and normal vibrations,” *J. Phys. Chem.*, no. 98, pp. 100–110, 1994.

[126] Å. Wendsjö, J. Lindgren, J. O. Thomas, and G. C. Farrington, “The effect of temperature and concentration on the local environment in the system M(CF3SO3)2PEOn for M=Ni, Zn and Pb,” *Solid State Ionics*, vol. 53–56, no. PART 2, pp. 1077–1082, 1992, doi: 10.1016/0167-2738(92)90293-X.

[127] A. M. Christie, S. J. Lilley, E. Staunton, and Y. G. Andreev, “Increaing conductivity of crystalline Polymer electrolytes,” *Nature*, vol. 433, no. January, pp. 50–53, 2005, doi: 10.1038/nature03190.1.

[128] F. Cheng, Y. Su, J. Liang, Z. Tao, and J. Chen, “MnO2-based nanostructures as catalysts for electrochemical oxygen reduction in alkaline media,” *Chem. Mater.*, vol. 22, no. 3, pp. 898–905, 2010, doi: 10.1021/cm901698s.

[129] M. H. Alfaruqi *et al.*, “Electrochemically Induced Structural Transformation in a γ-MnO_2 Cathode of a High Capacity Zinc-Ion Battery System,” *Chem. Mater.*, vol. 27, no. 10, pp. 3609–3620, 2015, doi: 10.1021/cm504717p.

[130] Y. Xu, Y. Zhang, Z. Guo, J. Ren, Y. Wang, and H. Peng, “Flexible, Stretchable, and Rechargeable Fiber-Shaped Zinc-Air Battery Based on Cross-Stacked Carbon Nanotube Sheets,” *Angew. Chemie - Int. Ed.*, vol. 54, no. 51, pp. 15390–15394, 2015, doi: 10.1002/anie.201508848.

[131] S. Y. Chew *et al.*, “Flexible free-standing carbon nanotube films for model lithium-ion batteries,” *Carbon N. Y.*, vol. 47, no. 13, pp. 2976–2983, 2009, doi: 10.1016/j.carbon.2009.06.045.

[132] R. Mukherjee, A. V. Thomas, A. Krishnamurthy, and N. Koratkar, “Photothermally reduced graphene as high-power anodes for lithium-ion Batteries,” *ACS Nano*, vol. 6, no. 9, pp. 7867–7878, 2012, doi: 10.1021/nn303145j.

[133] X. Jia *et al.*, “Direct growth of flexible LiMn2O4/CNT lithium-ion cathodes,” *Chem. Commun.*, vol. 47, no. 34, p. 9669, 2011, doi: 10.1039/c1cc13536h.

[134] N. Li, G. Zhou, R. Fang, H. Cheng, F. Li, and H. Cheng, “TiO2/graphene sandwich paper as an anisotropic electrode for high rate lithium ion batteries.,” *Nanoscale*, vol. 5, no. 17, pp. 3–6, 2013, doi: 10.1039/c3nr01349a.

[135] A. Yu, H. W. Park, A. Davies, D. C. Higgins, Z. Chen, and X. Xiao, “Free-standing layer-by-layer hybrid thin film of graphene-MnO2 nanotube as anode for lithium ion batteries,”

J. Phys. Chem. Lett., vol. 2, no. 15, pp. 1855–1860, 2011, doi: 10.1021/jz200836h.

[136] Y. Dai *et al.*, "Fabrication of self-binding noble metal/flexible graphene composite paper," *Carbon N. Y.*, vol. 50, no. 12, pp. 4648–4654, 2012, doi: 10.1016/j.carbon.2012.05.053.

[137] D. Wang *et al.*, "Ternary self-assembly of ordered metal oxide−graphene nanocomposites for electrochemical energy storage," *ACS Nano*, vol. 4, no. 3, pp. 1587–1595, 2010.

[138] J. W. Lee, S. Y. Lim, H. M. Jeong, T. H. Hwang, J. K. Kang, and J. W. Choi, "Extremely stable cycling of ultra-thin V2O5 nanowire–graphene electrodes for lithium rechargeable battery cathodes," *Energy Environ. Sci.*, vol. 5, no. 12, p. 9889, 2012, doi: 10.1039/c2ee22004k.

[139] S. Thieme *et al.*, "High capacity micro-mesoporous carbon-sulfur nanocomposite cathodes with enhanced cycling stability prepared by a solvent-free procedure," *J. Mater. Chem. A*, vol. 1, no. 32, pp. 9225–9234, 2013, doi: 10.1039/c3ta10641a.

[140] L. Hu, H. Wu, F. La Mantia, Y. Yang, and Y. Cui, "Thin, Flexible Secondary Li-Ion Paper Batteries," *ACS Nano*, vol. 4, no. 10, pp. 5843–5848, Oct. 2010, doi: 10.1021/nn1018158.

[141] R. Pan *et al.*, "Mesoporous Cladophora cellulose separators for lithium-ion batteries," *J. Power Sources*, vol. 321, pp. 185–192, 2016, doi: 10.1016/j.jpowsour.2016.04.115.

[142] S. Leijonmarck, A. Cornell, G. Lindbergh, and L. Wågberg, "Single-paper flexible Li-ion battery cells through a paper-making process based on nano-fibrillated cellulose," *J. Mater. Chem. A*, vol. 1, no. 15, p. 4671, 2013, doi: 10.1039/c3ta01532g.

[143] H. Li *et al.*, "Environmental Science An extremely safe and wearable solid-state zinc polymer electrolyte †," pp. 941–951, 2018, doi: 10.1039/c7ee03232c.

[144] N. Zhang *et al.*, "Rechargeable aqueous zinc-manganese dioxide batteries with high energy and power densities," *Nat. Commun.*, vol. 8, no. 1, pp. 1–9, 2017, doi: 10.1038/s41467-017-00467-x.

[145] P. Senguttuvan *et al.*, "A high power rechargeable nonaqueous multivalent Zn/V2O5 battery," *Adv. Energy Mater.*, vol. 6, no. 24, 2016, doi: 10.1002/aenm.201600826.

[146] P. He *et al.*, "Layered VS2 nanosheet-based aqueous Zn ion battery cathode," *Adv. Energy Mater.*, vol. 7, no. 11, pp. 2–6, 2017, doi: 10.1002/aenm.201601920.

[147] J. F. Snyder*, D. M. Baechle, and E.D.Wetzel., "Multifunctional Structural Composite Batteries for U . S . Army Applications," no. December, pp. 1–4, 2008.

[148] S. Ekstedt, M. Wysocki, and L. E. Asp, "Structural batteries made from fibre reinforced composites," *Plast. Rubber Compos.*, vol. 39, no. 3–5, pp. 148–150, 2010, doi: 10.1179/174328910X12647080902259.

[149] N. Ihrner and M. Johansson, “Improved performance of solid polymer electrolytes for structural batteries utilizing plasticizing co-solvents,” *J. Appl. Polym. Sci.*, vol. 134, no. 23, pp. 1–6, 2017, doi: 10.1002/app.44917.

[150] P. Liu, E. Sherman, and A. Jacobsen, “Design and fabrication of multifunctional structural batteries,” *J. Power Sources*, 2009, doi: 10.1016/j.jpowsour.2008.09.082.

[151] J. P. Thomas and M. A. Qidwai, “Mechanical design and performance of composite multifunctional materials,” *Acta Mater.*, vol. 52, no. 8, pp. 2155–2164, 2004, doi: 10.1016/j.actamat.2004.01.007.

[152] A. K. Singh *et al.*, “Design, manufacture and test of a novel structural battery based on sandwich construction,” *J. Sandw. Struct. Mater.*, vol. 17, no. 6, pp. 666–690, 2015, doi: 10.1177/1099636215591908.

[153] P. Ladpli *et al.*, “Multifunctional Energy Storage Composites - Electrochemical and mechanical cycling characterization,” *Batter. Congr. 2016*, no. May, 2016.

[154] P. Ladpli *et al.*, “Multifunctional Energy Storage Composites: Design, Fabrication, and Experimental Characterization,” *Vol. 2 ASME 2016 Energy Storage Forum*, no. July, p. V002T01A004, 2016, doi: 10.1115/ES2016-59416.

[155] F. M. Guillot, H. W. Beckham, and J. Leisen, “Hollow Piezoelectric Ceramic Fibers for Energy Harvesting Fabrics,” *J. Eng. Fiber. Fabr.*, vol. 8, no. 1, pp. 75–81, 2013.

[156] G. Zhou, E. Paek, G. S. Hwang, and A. Manthiram, “Long-life Li/polysulphide batteries with high sulphur loading enabled by lightweight three-dimensional nitrogen/sulphur-codoped graphene sponge,” *Nat. Commun.*, vol. 6, pp. 1–11, 2015, doi: 10.1038/ncomms8760.

[157] M. Vijayakumar *et al.*, “Molecular structure and stability of dissolved lithium polysulfide species,” *Phys. Chem. Chem. Phys.*, vol. 16, no. 22, pp. 10923–10932, 2014, doi: 10.1039/c4cp00889h.

[158] S. Bai, X. Liu, K. Zhu, S. Wu, and H. Zhou, “Metal-organic framework-based separator for lithium-sulfur batteries,” *Nat. Energy*, vol. 1, no. 7, 2016, doi: 10.1038/nenergy.2016.94.

[159] S.-E. Cheon, K.-S. Ko, J.-H. Cho, S.-W. Kim, E.-Y. Chin, and H.-T. Kim, “Rechargeable Lithium Sulfur Battery,” *J. Electrochem. Soc.*, vol. 150, no. 6, p. A796, 2003, doi: 10.1149/1.1571533.

[160] J. Conder, R. Bouchet, S. Trabesinger, C. Marino, L. Gubler, and C. Villevieille, “Direct observation of lithium polysulfides in lithium-sulfur batteries using operando X-ray diffraction,” *Nat. Energy*, vol. 2, no. May, pp. 1–7, 2017, doi: 10.1038/nenergy.2017.69.

[161] Y. V. Mikhaylik and J. R. Akridge, “Polysulfide Shuttle Study in the Li/S Battery System,” *J. Electrochem. Soc.*, vol. 151, no. 11, p. A1969, 2004, doi: 10.1149/1.1806394.

[162] A. Manthiram, Y. Fu, S. H. Chung, C. Zu, and Y. S. Su, “Rechargeable lithium-sulfur batteries,” *Chem. Rev.*, vol. 114, no. 23, pp. 11751–11787, 2014, doi: 10.1021/cr500062v.

[163] Q. Pang, D. Kundu, M. Cuisinier, and L. F. Nazar, “Surface-enhanced redox chemistry of polysulphides on a metallic and polar host for lithium-sulphur batteries,” *Nat. Commun.*, vol. 5, no. May, pp. 1–8, 2014, doi: 10.1038/ncomms5759.

[164] H. Yao *et al.*, “Improving lithium-sulphur batteries through spatial control of sulphur species deposition on a hybrid electrode surface,” *Nat. Commun.*, vol. 5, no. May, pp. 1–9, 2014, doi: 10.1038/ncomms4943.

[165] X. Ji, K. T. Lee, and L. F. Nazar, “A highly ordered nanostructured carbon-sulphur cathode for lithium-sulphur batteries,” *Nat. Mater.*, vol. 8, no. 6, pp. 500–506, 2009, doi: 10.1038/nmat2460.

[166] Z. Sun *et al.*, “Conductive porous vanadium nitride/graphene composite as chemical anchor of polysulfides for lithium-sulfur batteries,” *Nat. Commun.*, vol. 8, pp. 1–8, 2017, doi: 10.1038/ncomms14627.

[167] L. Yin, J. Wang, F. Lin, J. Yang, and Y. Nuli, “Polyacrylonitrile/graphene composite as a precursor to a sulfur-based cathode material for high-rate rechargeable Li-S batteries,” *Energy Environ. Sci.*, vol. 5, no. 5, pp. 6966–6972, 2012, doi: 10.1039/c2ee03495f.

[168] S. Chen *et al.*, “Nanostructured polyaniline-decorated Pt/C@PANI core-shell catalyst with enhanced durability and activity,” *J. Am. Chem. Soc.*, vol. 134, no. 32, pp. 13252–13255, 2012, doi: 10.1021/ja306501x.

[169] Z. W. Seh *et al.*, “Two-dimensional layered transition metal disulphides for effective encapsulation of high-capacity lithium sulphide cathodes,” *Nat. Commun.*, vol. 5, pp. 1–8, 2014, doi: 10.1038/ncomms6017.

[170] Z. W. Seh *et al.*, “Sulphur-TiO2 yolk-shell nanoarchitecture with internal void space for long-cycle lithium-sulphur batteries,” *Nat. Commun.*, vol. 4, 2013, doi: 10.1038/ncomms2327.

[171] X. Liang, A. Garsuch, and L. F. Nazar, “Sulfur cathodes based on conductive MXene nanosheets for high-performance lithium-sulfur batteries,” *Angew. Chemie - Int. Ed.*, vol. 54, no. 13, pp. 3907–3911, 2015, doi: 10.1002/anie.201410174.

[172] R. Demir-Cakan *et al.*, “Cathode composites for Li-S batteries via the use of oxygenated porous architectures,” *J. Am. Chem. Soc.*, vol. 133, no. 40, pp. 16154–16160, 2011, doi: 10.1021/ja2062659.

[173] J. Zheng *et al.*, “Lewis acid-base interactions between polysulfides and metal organic framework in lithium sulfur batteries,” *Nano Lett.*, vol. 14, no. 5, pp. 2345–2352, 2014, doi: 10.1021/nl404721h.

[174] Y. X. Yin, S. Xin, Y. G. Guo, and L. J. Wan, “Lithium-sulfur batteries: Electrochemistry,

materials, and prospects," *Angew. Chemie - Int. Ed.*, vol. 52, no. 50, pp. 13186–13200, 2013, doi: 10.1002/anie.201304762.

[175] K. Park *et al.*, "Trapping lithium polysulfides of a Li-S battery by forming lithium bonds in a polymer matrix," *Energy Environ. Sci.*, vol. 8, no. 8, pp. 2389–2395, 2015, doi: 10.1039/c5ee01809a.

[176] W. Zhou, Y. Yu, H. Chen, F. J. Disalvo, and H. D. Abruña, "Yolk-shell structure of polyaniline-coated sulfur for lithium-sulfur batteries," *JACS*, vol. 135, no. 44, pp. 16736–16743, 2013, doi: 10.1021/ja409508q.

[177] Y. Liu, G. Li, J. Fu, Z. Chen, and X. Peng, "Strings of porous carbon polyhedrons as self-standing cathode host for high-energy-density lithium-sulfur batteries," *Angew. Chem. Int. Ed.*, vol. 56, pp. 6176–6180, 2017, doi: 10.1002/anie.201700686.

[178] S. H. Chung and A. Manthiram, "Bifunctional separator with a light-weight carbon-coating for dynamically and statically stable lithium-sulfur batteries," *Adv. Funct. Mater.*, vol. 24, no. 33, pp. 5299–5306, 2014, doi: 10.1002/adfm.201400845.

[179] H. Yao *et al.*, "Improved lithium-sulfur batteries with a conductive coating on the separator to prevent the accumulation of inactive S-related species at the cathode-separator interface," *Energy Environ. Sci.*, vol. 7, no. 10, pp. 3381–3390, 2014, doi: 10.1039/c4ee01377h.

[180] X. Liang, C. Hart, Q. Pang, A. Garsuch, T. Weiss, and L. F. Nazar, "A highly efficient polysulfide mediator for lithium-sulfur batteries," *Nat. Commun.*, vol. 6, pp. 1–8, 2015, doi: 10.1038/ncomms6682.

[181] H. J. Peng *et al.*, "Janus separator of polypropylene-supported cellular graphene framework for sulfur cathodes with high utilization in lithium-sulfur batteries," *Adv. Sci.*, vol. 3, no. 1, pp. 1–11, 2015, doi: 10.1002/advs.201500268.

[182] S. H. Chung, P. Han, R. Singhal, V. Kalra, and A. Manthiram, "Electrochemically Stable Rechargeable Lithium-Sulfur Batteries with a Microporous Carbon Nanofiber Filter for Polysulfide," *Adv. Energy Mater.*, vol. 5, no. 18, pp. 1–12, 2015, doi: 10.1002/aenm.201500738.

[183] J. Q. Huang, Q. Zhang, and F. Wei, "Multi-functional separator/interlayer system for high-stable lithium-sulfur batteries: Progress and prospects," *Energy Storage Mater.*, vol. 1, pp. 127–145, 2015, doi: 10.1016/j.ensm.2015.09.008.

[184] Y. S. Su and A. Manthiram, "A new approach to improve cycle performance of rechargeable lithium-sulfur batteries by inserting a free-standing MWCNT interlayer," *Chem. Commun.*, vol. 48, no. 70, pp. 8817–8819, 2012, doi: 10.1039/c2cc33945e.

[185] I. Bauer, S. Thieme, J. Brückner, H. Althues, and S. Kaskel, "Reduced polysulfide shuttle in lithium-sulfur batteries using Nafion-based separators," *J. Power Sources*, vol. 251, pp. 417–422, 2014, doi: 10.1016/j.jpowsour.2013.11.090.

[186] M. Gu *et al.*, “Inhibiting the shuttle effect in lithium-sulfur batteries using a layer-by-layer assembled ion-permselective separator,” *RSC Adv.*, vol. 4, no. 87, pp. 46940–46946, 2014, doi: 10.1039/c4ra09718a.

[187] H. J. Peng *et al.*, “A Cooperative Interface for Highly Efficient Lithium–Sulfur Batteries,” *Adv. Mater.*, vol. 28, no. 43, pp. 9551–9558, 2016, doi: 10.1002/adma.201603401.

[188] Z. Zhang, Y. Lai, Z. Zhang, K. Zhang, and J. Li, “Al2O3-coated porous separator for enhanced electrochemical performance of lithium sulfur batteries,” *Electrochim. Acta*, vol. 129, pp. 55–61, 2014, doi: 10.1016/j.electacta.2014.02.077.

[189] W. Li *et al.*, “V2O5polysulfide anion barrier for long-lived Li-S batteries,” *Chem. Mater.*, vol. 26, no. 11, pp. 3404–3410, 2014, doi: 10.1021/cm500575q.

[190] Q. Xu, G. C. Hu, H. L. Bi, and H. F. Xiang, “A trilayer carbon nanotube/Al2O3/polypropylene separator for lithium-sulfur batteries,” *Ionics (Kiel).*, vol. 21, no. 4, pp. 981–986, 2015, doi: 10.1007/s11581-014-1263-4.

[191] Y. S. Oh *et al.*, “Janus-Faced, Dual-Conductive/Chemically Active Battery Separator Membranes,” *Adv. Funct. Mater.*, vol. 26, no. 39, pp. 7074–7083, 2016, doi: 10.1002/adfm.201602734.

[192] T. Lei *et al.*, “A nonflammable and thermotolerant separator suppresses pPolysulfide dissolution for safe and long-cycle lithium-sulfur batteries,” *Adv. Energy Mater.*, p. 1802441, 2018, doi: 10.1002/aenm.201802441.

[193] M. Ryou, D. J. Lee, J. Lee, Y. M. Lee, and J. Park, “Excellent Cycle Life of Lithium-Metal Anodes in Lithium-Ion Batteries with Mussel-Inspired Polydopamine-Coated Separators,” *Adv. Energy Mater.*, vol. 2, pp. 645–650, 2012, doi: 10.1002/aenm.201100687.

[194] R. Cao, W. Xu, D. Lv, J. Xiao, and J. Zhang, “Anodes for Rechargeable Lithium-Sulfur Batteries,” *Adv. Energy Mater.*, vol. 5, p. 1402273, 2015, doi: 10.1002/aenm.201402273.

[195] C. Monroe and J. Newman, “The Impact of Elastic Deformation on Deposition Kinetics at Lithium/Polymer Interfaces,” *J. Electrochem. Soc.*, vol. 152, no. 2, p. A396, 2005, doi: 10.1149/1.1850854.

[196] W. Wang, R. Christensen, B. Curtis, S. W. Martin, and J. Kieffer, “A new model linking elastic properties and ionic conductivity of mixed network former glasses,” *Phys. Chem. Chem. Phys.*, vol. 20, no. 3, pp. 1629–1641, Jan. 2018, doi: 10.1039/C7CP04534D.

[197] A. Maroudas and H. Evans, “A Study of Ionic Equilibria in Cartilage,” *Connect. Tissue Res.*, vol. 1, no. 1, pp. 69–77, Jan. 1972, doi: 10.3109/03008207209152058.

[198] E. M. H. Obeid, M. A. Adams, and J. H. Newman, “Mechanical properties of articular cartilage in knees with unicompartmental osteoarthritis,” *J. Bone Jt. Surg.*, vol. 76-B, no. 2, p. 315, 1994.

[199] C. Jiang, S. Markutsya, Y. Pikus, and V. V Tsukruk, “Freely suspended nanocomposite membranes as highly sensitive sensors.,” *Nat. Mater.*, vol. 3, no. 10, pp. 721–8, Oct. 2004, doi: 10.1038/nmat1212.

[200] J. Seo *et al.*, “Tunable Layer-by-Layer Polyelectrolyte Platforms for Comparative Cell Assays,” 2009.

[201] K. Ariga, J. P. Hill, and Q. Ji, “Layer-by-layer assembly as a versatile bottom-up nanofabrication technique for exploratory research and realistic application,” *Phys. Chem. Chem. Phys.*, vol. 9, no. 19, p. 2319, May 2007, doi: 10.1039/b700410a.

[202] G. Decher and J. B. Schlenoff, *Multilayer Thin Films: Sequential Assembly of Nanocomposite Materials: Second Edition*, vol. 1–2. John Wiley & Sons, 2012.

[203] N. A. Kotov, I. Dékány, and J. H. Fendler, “Ultrathin graphite oxide-polyelectrolyte composites prepared by self-assembly: Transition between conductive and non-conductive states,” *Adv. Mater.*, vol. 8, no. 8, pp. 637–641, Aug. 1996, doi: 10.1002/adma.19960080806.

[204] Y. Lvov, S. Yamada, and T. Kunitake, “Non-linear optical effects in layer-by-layer alternate films of polycations and an azobenzene-containing polyanion,” *Thin Solid Films*, vol. 300, no. 1–2, pp. 107–112, May 1997, doi: 10.1016/S0040-6090(96)09494-1.

[205] K. Ariga, A. Vinu, Y. Yamauchi, Q. Ji, and J. P. Hill, “Nanoarchitectonics for Mesoporous Materials,” *Bull. Chem. Soc. Jpn.*, vol. 85, no. 1, pp. 1–32, Jan. 2012, doi: 10.1246/bcsj.20110162.

[206] C. Jiang, S. Markutsya, and V. V. Tsukruk, “Compliant, robust, and truly nanoscale free-standing multilayer films fabricated using spin-assisted layer-by-layer assembly,” *Adv. Mater.*, vol. 16, no. 2, pp. 157–161, 2004, doi: 10.1002/adma.200306010.

[207] J. Luo, M. Zhang, B. Yang, G. Liu, and S. Song, “Fabrication and characterization of differentiated aramid nanofibers and transparent films,” *Appl. Nanosci.*, vol. 9, no. 5, pp. 631–645, 2019, doi: 10.1007/s13204-018-0722-z.

[208] T. A. Pascal, C. D. Pemmaraju, and D. Prendergast, “X-ray spectroscopy as a probe for lithium polysulfide radicals,” *Phys. Chem. Chem. Phys.*, vol. 17, no. 12, pp. 7743–7753, 2015, doi: 10.1039/c4cp05316h.

[209] E. P. Kamphaus and P. B. Balbuena, “Long-Chain Polysulfide Retention at the Cathode of Li-S Batteries,” *J. Phys. Chem. C*, vol. 120, no. 8, pp. 4296–4305, 2016, doi: 10.1021/acs.jpcc.5b12538.

[210] V. Murugesan *et al.*, “Elucidating the Solvation Structure and Dynamics of Lithium Polysulfides Resulting from Competitive Salt and Solvent Interactions,” *Chem. Mater.*, vol. 29, no. 8, pp. 3375–3379, 2017, doi: 10.1021/acs.chemmater.7b00068.

[211] C. Li, A. L. Ward, S. E. Doris, T. A. Pascal, D. Prendergast, and B. A. Helms,

"Polysulfide-Blocking Microporous Polymer Membrane Tailored for Hybrid Li-Sulfur Flow Batteries," *Nano Lett.*, vol. 15, pp. 5724–5729, 2015, doi: 10.1021/acs.nanolett.5b02078.

[212] R. Khurana, J. L. Schaefer, L. A. Archer, and G. W. Coates, "Suppression of lithium dendrite growth using cross-linked polyethylene/poly(ethylene oxide) electrolytes: A new approach for practical lithium-metal polymer batteries," *J. Am. Chem. Soc.*, vol. 136, no. 20, pp. 7395–7402, 2014, doi: 10.1021/ja502133j.

[213] D. S. Koktysh *et al.*, "Biomaterials by design: Layer-by-layer assembled ion-selective and biocompatible films of TiO2 nanoshells for neurochemical monitoring," *Adv. Funct. Mater.*, vol. 12, no. 4, pp. 255–265, 2002.

[214] L. Krasemann and B. Tieke, "Selective Ion Transport across Self-Assembled Alternating Multilayers of Cationic and Anionic Polyelectrolytes," *Langmuir*, no. 15, pp. 287–290, 2000, doi: 10.1021/la991240z.

[215] J. J. Harris, J. L. Stair, and M. L. Bruening, "Layered Polyelectrolyte Films as Selective , Ultrathin Barriers for Anion Transport," *Chem. Mater.*, no. 22, pp. 1941–1946, 2000, doi: 10.1021/cm0001004.

[216] S. W. Kowalczyk, T. R. Blosser, and C. Dekker, "Biomimetic nanopores: Learning from and about nature," *Trends Biotechnol.*, vol. 29, no. 12, pp. 607–614, 2011, doi: 10.1016/j.tibtech.2011.07.006.

[217] M. R. Gouaux E and Gouaux E, Mackinnon R, "Principles of selective ion transport in channels and pumps," *Science (80-.).*, vol. 310, no. 5753, pp. 1461–5, 2005, doi: 10.1126/science.1113666.

[218] J.-Q. Huang *et al.*, "Permselective Graphene Oxide Membrane for Highly Stable and Anti-Self-Dischage Lithium-Sulfur Batteries," *ACS Nano*, vol. 9, no. 3, pp. 3002–3011, 2015, doi: 10.1021/nn507178a.

[219] M. Shaibani *et al.*, "Suppressed Polysulfide Crossover in Li-S Batteries through a High-Flux Graphene Oxide Membrane Supported on a Sulfur Cathode," *ACS Nano*, vol. 10, no. 8, pp. 7768–7779, 2016, doi: 10.1021/acsnano.6b03285.

[220] X. Tao *et al.*, "Balancing surface adsorption and diffusion of lithium-polysulfides on nonconductive oxides for lithium-sulfur battery design," *Nat. Commun.*, vol. 7, pp. 1–9, 2016, doi: 10.1038/ncomms11203.

[221] S. R. Das, S. B. Majumder, and R. S. Katiyar, "Kinetic analysis of the Li+ ion intercalation behavior of solution derived nano-crystalline lithium manganate thin films," *J. Power Sources*, vol. 139, no. 1–2, pp. 261–268, 2005, doi: 10.1016/j.jpowsour.2004.06.056.

[222] J. Wang, F. Lin, H. Jia, J. Yang, C. W. Monroe, and Y. Nuli, "Towards a safe lithium-sulfur battery with a flame-inhibiting electrolyte and a sulfur-based composite cathode,"

Angew. Chemie - Int. Ed., vol. 53, no. 38, pp. 10099–10104, 2014, doi: 10.1002/anie.201405157.

[223] Z. A. Ghazi *et al.*, "MoS2/Celgard Separator as Efficient Polysulfide Barrier for Long-Life Lithium–Sulfur Batteries," *Adv. Mater.*, vol. 29, no. 21, pp. 1–6, 2017, doi: 10.1002/adma.201606817.

[224] L. Qie and A. Manthiram, "A facile layer-by-layer approach for high-areal-capacity sulfur cathodes," *Adv. Mater.*, p. 201405689, 2015, doi: 10.1002/adma.201405689.

[225] R. Song, R. Fang, L. Wen, Y. Shi, S. Wang, and F. Li, "A trilayer separator with dual function for high performance lithium-sulfur batteries," *J. Power Sources*, vol. 301, pp. 179–186, 2016, doi: 10.1016/j.jpowsour.2015.10.007.

[226] X. Gu *et al.*, "A porous nitrogen and phosphorous dual doped graphene blocking layer for high performance Li–S batteries," *J. Mater. Chem. A*, vol. 3, no. 32, pp. 16670–16678, 2015, doi: 10.1039/C5TA04255K.

[227] J. Sun *et al.*, "Entrapment of Polysulfides by a Black-Phosphorus-Modified Separator for Lithium–Sulfur Batteries," *Adv. Mater.*, vol. 28, no. 44, pp. 9797–9803, 2016, doi: 10.1002/adma.201602172.

[228] X. Gu *et al.*, "Microporous bamboo biochar for lithium − sulfur batteries," *Nano Res.*, vol. 8, no. 1, pp. 129–139, 2015, doi: 10.1007/s12274-014-0601-1.

[229] C. H. Chang, S. H. Chung, and A. Manthiram, "Effective Stabilization of a High-Loading Sulfur Cathode and a Lithium-Metal Anode in Li-S Batteries Utilizing SWCNT-Modulated Separators," *Small*, vol. 12, no. 2, pp. 174–179, 2016, doi: 10.1002/smll.201502505.

[230] C. Y. Fan *et al.*, "The Effective Design of a Polysulfide-Trapped Separator at the Molecular Level for High Energy Density Li-S Batteries," *ACS Appl. Mater. Interfaces*, vol. 8, no. 25, pp. 16108–16115, 2016, doi: 10.1021/acsami.6b04578.

[231] M. Liu *et al.*, "Suppressing Self-Discharge and Shuttle Effect of Lithium–Sulfur Batteries with V2O5-Decorated Carbon Nanofiber Interlayer," *Small*, vol. 13, no. 12, pp. 1–7, 2017, doi: 10.1002/smll.201602539.

[232] Y. Xiang *et al.*, "Interfacing soluble polysulfides with a SnO2functionalized separator: An efficient approach for improving performance of Li-S battery," *J. Memb. Sci.*, vol. 563, no. June, pp. 380–387, 2018, doi: 10.1016/j.memsci.2018.06.004.

[233] X. Liang, Y. Rangom, C. Y. Kwok, Q. Pang, and L. F. Nazar, "Interwoven MXene Nanosheet/Carbon-Nanotube Composites as Li–S Cathode Hosts," *Adv. Mater.*, vol. 29, no. 3, pp. 1–7, 2017, doi: 10.1002/adma.201603040.

[234] Z. Zhou, B. Chen, T. Fang, Y. Li, Z. Zhou, and Q. Wang, "A multifunctional separator enables safe and durable lithium/magnesium-sulfur batteries under elevated temperature,"

Adv. Energy Mater., vol. 10, p. 1902023, 2020, doi: 10.1002/aenm.201902023.

[235] J. Sun *et al.*, "Towards a reliable Li-metal-free LiNO3-free Li-ion polysulphide full cell: Via parallel interface engineering," *Energy Environ. Sci.*, vol. 11, no. 9, pp. 2509–2520, 2018, doi: 10.1039/c8ee00937f.

[236] J. Wang, M. Zhang, J. Zhai, and L. Jiang, "Theoretical simulation of the ion current rectification (ICR) in nano-pores based on the Poisson-Nernst-Planck (PNP) model," *Phys. Chem. Chem. Phys.*, vol. 16, no. 1, pp. 23–32, 2014, doi: 10.1039/c3cp51712h.

[237] O. Axelssonc, X. He, and M. Neytcheva, "Numerical solution of the time-dependent navier-stokes equation for variable density-variable viscosity. Part I," *Math. Model. Anal.*, vol. 20, no. 2, pp. 232–260, 2015, doi: 10.3846/13926292.2015.1021395.

[238] J. Cervera, B. Schiedt, and P. Ramírez, "A poisson/nernst-planck model for ionic transport through synthetic conical nanopores," *Europhys. Lett.*, vol. 71, no. 1, pp. 35–41, 2005, doi: 10.1209/epl/i2005-10054-x.

[239] D. Gillespie, W. Nonner, and R. S. Eisenberg, "Coupling poisson-nernst-planck and density functional theory to calculate ion flux," *J. Phys. Condens. Matter*, vol. 14, no. 46, pp. 12129–12145, 2002, doi: 10.1088/0953-8984/14/46/317.

[240] S. Kalnaus, A. S. Sabau, W. E. Tenhaeff, N. J. Dudney, and C. Daniel, "Design of composite polymer electrolytes for Li ion batteries based on mechanical stability criteria," *J. Power Sources*, vol. 201, pp. 280–287, 2012, doi: https://doi.org/10.1016/j.jpowsour.2011.11.020.

[241] X. Zhang *et al.*, "Rethinking How External Pressure Can Suppress Dendrites in Lithium Metal Batteries," *J. Electrochem. Soc.*, vol. 166, no. 15, pp. A3639–A3652, 2019, doi: 10.1149/2.0701914jes.

[242] P. Bai *et al.*, "Interactions between Lithium Growths and Nanoporous Ceramic Separators," *Joule*, vol. 2, no. 11, pp. 2434–2449, 2018, doi: https://doi.org/10.1016/j.joule.2018.08.018.

[243] S. Choudhury, D. Vu, A. Warren, M. D. Tikekar, Z. Tu, and L. A. Archer, "Confining electrodeposition of metals in structured electrolytes," *Proc. Natl. Acad. Sci.*, vol. 115, no. 26, pp. 6620 LP – 6625, Jun. 2018, doi: 10.1073/pnas.1803385115.

[244] E. Khoo, H. Zhao, and M. Z. Bazant, "Linear Stability Analysis of Transient Electrodeposition in Charged Porous Media: Suppression of Dendritic Growth by Surface Conduction," *J. Electrochem. Soc.*, vol. 166, no. 10, pp. A2280–A2299, 2019, doi: 10.1149/2.1521910jes.

[245] S. Stalin, S. Choudhury, K. Zhang, and L. A. Archer, "Multifunctional Cross-Linked Polymeric Membranes for Safe, High-Performance Lithium Batteries," *Chem. Mater.*, vol. 30, no. 6, pp. 2058–2066, Mar. 2018, doi: 10.1021/acs.chemmater.7b05353.

[246] “https://amesweb.info/Materials/Poissons_Ratio_of_Polymers.aspx.” .

[247] K. Nakamura, M. Wada, S. Kuga, and T. Okano, “Poisson’s ratio of cellulose Iβ and cellulose II,” *J. Polym. Sci. Part B Polym. Phys.*, vol. 42, no. 7, pp. 1206–1211, Apr. 2004, doi: https://doi.org/10.1002/polb.10771.

[248] F. Hao, W. Wang, and P. P. Mukherjee, “Mechano-Electrochemical Interaction in Solid-State Lithium Batteries,” *J. Electrochem. Soc.*, vol. 167, no. 8, p. 80513, 2020, doi: 10.1149/1945-7111/ab8a98.

[249] C. Picart *et al.*, “Molecular basis for the explanation of the exponential growth of polyelectrolyte multilayers.,” *Proc. Natl. Acad. Sci. U. S. A.*, vol. 99, no. 20, pp. 12531–5, Oct. 2002, doi: 10.1073/pnas.202486099.

[250] C. Porcel, P. Lavalle, G. Decher, B. Senger, J.-C. Voegel, and P. Schaaf, “Influence of the polyelectrolyte molecular weight on exponentially growing multilayer films in the linear regime.,” *Langmuir*, vol. 23, no. 4, pp. 1898–904, Feb. 2007, doi: 10.1021/la062728k.

[251] J. Zhu, D. Watts, and N. A. Kotov, “Gelation-Assisted Layer-by-Layer Deposition of High Performance Nanocomposites,” *Zeitschrift für Phys. Chemie*, vol. 232, no. 9–11, pp. 1383–1398, Aug. 2018, doi: 10.1515/zpch-2018-1169.

[252] X. Hao *et al.*, “Ultrastrong Polyoxyzole Nanofiber Membranes for Dendrite-Proof and Heat-Resistant Battery Separators,” *Nano Lett.*, vol. 16, no. 5, pp. 2981–2987, 2016, doi: 10.1021/acs.nanolett.5b05133.

[253] J. Zhang *et al.*, “Renewable and superior thermal-resistant cellulose-based composite nonwoven as lithium-ion battery separator,” *ACS Appl. Mater. Interfaces*, vol. 5, no. 1, pp. 128–134, 2013, doi: 10.1021/am302290n.

[254] Q. Xu *et al.*, “Cellulose/Polysulfonamide Composite Membrane as a High Performance Lithium-Ion Battery Separator,” *ACS Sustain. Chem. Eng.*, vol. 2, no. 2, pp. 194–199, Feb. 2014, doi: 10.1021/sc400370h.

[255] J. Song *et al.*, “Co-polyimide-coated polyethylene separators for enhanced thermal stability of lithium ion batteries,” *Electrochim. Acta*, vol. 85, pp. 524–530, 2012, doi: 10.1016/j.electacta.2012.06.078.

[256] Y. Zhai *et al.*, “Sandwich-structured PVdF/PMIA/PVdF nanofibrous separators with robust mechanical strength and thermal stability for lithium ion batteries,” *J. Mater. Chem. A*, vol. 2, no. 35, p. 14511, 2014, doi: 10.1039/C4TA02151G.

[257] Y. Ansari *et al.*, “Low-cost, dendrite-blocking polymer-Sb2O3 separators for lithium and sodium batteries,” *J. Electrochem. Soc.*, vol. 161, no. 10, pp. A1655–A1661, 2014, doi: 10.1149/2.0631410jes.

[258] G. L. Ji, B. K. Zhu, Z. Y. Cui, C. F. Zhang, and Y. Y. Xu, “PVDF porous matrix with controlled microstructure prepared by TIPS process as polymer electrolyte for lithium ion

battery," *Polymer (Guildf).*, vol. 48, no. 21, pp. 6415–6425, 2007, doi: 10.1016/j.polymer.2007.08.049.

[259] C. J. Leo, G. V. Subba Rao, and B. V. R. Chowdari, "Studies on plasticized PEO-lithium triflate-ceramic filler composite electrolyte system," *Solid State Ionics*, vol. 148, no. 1–2, pp. 159–171, 2002, doi: 10.1016/S0167-2738(02)00107-8.

[260] Q. Pan, D. M. Smith, H. Qi, S. Wang, and C. Y. Li, "Hybrid Electrolytes with Controlled Network Structures for Lithium Metal Batteries," *Adv. Mater.*, vol. 27, no. 39, pp. 5995–6001, 2015, doi: 10.1002/adma.201502059.

[261] F. Gayet *et al.*, "Unique combination of mechanical strength, thermal stability, and high ion conduction in PMMA - Silica nanocomposites containing high loadings of ionic liquid," *Chem. Mater.*, vol. 21, no. 23, pp. 5575–5577, 2009, doi: 10.1021/cm9027918.

[262] M. Patel, K. G. Chandrappa, and A. J. Bhattacharyya, "Increasing ionic conductivity and mechanical strength of a plastic electrolyte by inclusion of a polymer," *Electrochim. Acta*, vol. 54, no. 2, pp. 209–215, 2008, doi: 10.1016/j.electacta.2008.08.010.

[263] Q. Lu *et al.*, "Dendrite-free, high-rate, long-life lithium metal batteries with a 3D cross-linked network polymer electrolyte," *Adv. Mater.*, vol. 29, p. 1604460, 2017, doi: 10.1002/adma.201604460.

[264] J. Hao, G. Lei, Z. Li, L. Wu, Q. Xiao, and L. Wang, "A novel polyethylene terephthalate nonwoven separator based on electrospinning technique for lithium ion battery," *J. Memb. Sci.*, vol. 428, pp. 11–16, 2013, doi: 10.1016/j.memsci.2012.09.058.

[265] M. Yanilmaz, M. Dirican, and X. Zhang, "Evaluation of electrospun SiO2/nylon 6,6 nanofiber membranes as a thermally-stable separator for lithium-ion batteries," *Electrochim. Acta*, vol. 133, pp. 501–508, 2014, doi: 10.1016/j.electacta.2014.04.109.

[266] F. Li *et al.*, "A graphene-pure-sulfur sandwich structure for ultrafast, long-life lithium-sulfur batteries," *Adv. Mater.*, vol. 26, no. 4, pp. 625–631, 2014, doi: 10.1002/adma.201302877.

[267] S. H. Chung and A. Manthiram, "High-performance Li-S batteries with an ultra-lightweight MWCNT-coated separator," *J. Phys. Chem. Lett.*, vol. 5, no. 11, pp. 1978–1983, 2014, doi: 10.1021/jz5006913.

[268] L. Luo, S. H. Chung, and A. Manthiram, "A trifunctional multi-walled carbon nanotubes/polyethylene glycol (MWCNT/PEG)-coated separator through a layer-by-layer coating strategy for high-energy Li-S batteries," *J. Mater. Chem. A*, vol. 4, no. 43, pp. 16805–16811, 2016, doi: 10.1039/c6ta07709a.

[269] S. H. Chung and A. Manthiram, "A polyethylene glycol-supported microporous carbon coating as a polysulfide trap for utilizing pure sulfur cathodes in lithium-sulfur batteries," *Adv. Mater.*, vol. 26, no. 43, pp. 7352–7357, 2014, doi: 10.1002/adma.201402893.

[270] Y. S. Su and A. Manthiram, “Lithium-sulphur batteries with a microporous carbon paper as a bifunctional interlayer,” *Nat. Commun.*, vol. 3, p. 1166, 2012, doi: 10.1038/ncomms2163.

[271] H. Yao *et al.*, “Improved lithium–sulfur batteries with a conductive coating on the separator to prevent the accumulation of inactive S-related species at the cathode–separator interface,” *Energy Environ. Sci.*, vol. 7, no. 10, pp. 3381–3390, 2014, doi: 10.1039/C4EE01377H.

[272] F. Pei *et al.*, “A Two-dimensional porous carbon-modified separator for high-energy-density Li-S batteries,” *Joule*, vol. 2, no. 2, pp. 323–336, 2018, doi: 10.1016/j.joule.2017.12.003.

[273] X. Zhou, Q. Liao, J. Tang, T. Bai, F. Chen, and J. Yang, “A high-level N-doped porous carbon nanowire modified separator for long-life lithium-sulfur batteries,” *J. Electroanal. Chem.*, vol. 768, pp. 55–61, 2016, doi: 10.1016/j.jelechem.2016.02.037.

[274] G. Chen *et al.*, “A multifunctional separator modified with cobalt and nitrogen co-doped porous carbon nanofibers for Li–S batteries,” *J. Memb. Sci.*, vol. 548, no. October 2017, pp. 247–253, 2018, doi: 10.1016/j.memsci.2017.11.026.

[275] Z. Xiao *et al.*, “A lightweight TiO<inf>2</inf>/Graphene interlayer, applied as a highly effective polysulfide absorbent for fast, long-life lithium-sulfur batteries,” *Adv. Mater.*, vol. 27, no. 18, pp. 2891–2898, 2015, doi: 10.1002/adma.201405637.

[276] G. Xu *et al.*, “Absorption mechanism of carbon-nanotube paper-titanium dioxide as a multifunctional barrier material for lithium-sulfur batteries,” *Nano Res.*, vol. 8, no. 9, pp. 3066–3074, 2015, doi: 10.1007/s12274-015-0812-0.

[277] G. Xu *et al.*, “A thin multifunctional coating on a separator improves the cyclability and safety of lithium sulfur batteries,” *Chem. Sci.*, vol. 8, no. 9, pp. 6619–6625, 2017, doi: 10.1039/c7sc01961k.

[278] T. Zhou *et al.*, “Twinborn TiO2-TiN heterostructures enabling smooth trapping-diffusion-conversion of polysulfides towards ultralong life lithium-sulfur batteries,” *Energy Environ. Sci.*, vol. 10, no. 7, pp. 1694–1703, 2017, doi: 10.1039/c7ee01430a.

[279] B. Qi *et al.*, “Mesoporous TiN microspheres as an efficient polysulfide barrier for lithium–sulfur batteries,” *J. Mater. Chem. A*, 2018, doi: 10.1039/C8TA04920C.

[280] S. Kim *et al.*, “Simultaneous suppression of shuttle effect and lithium dendrite growth by lightweight bifunctional separator for Li-S batteries,” *ACS Appled Energy Mater.*, vol. 3, pp. 2643–2652, 2020, doi: 10.1021/acsaem.9b02350.

[281] Y. He, S. Wu, Q. Li, and H. Zhou, “Designing a multifunctional separator for high-performance Li-S batteries at elevated temperature,” *Small*, p. 1904332, 2019, doi: 10.1002/smll.201904332.

[282] E. Science, “Vertical Co9S8 hollow nanowall arrays grown on Celgard separator as a multifunctional polysulfide barrier for high- performance Li-S batteries,” 2018, doi: 10.1039/x0xx00000x.

[283] Y. Zhao *et al.*, “Dense coating of Li4Ti5O12and graphene mixture on the separator to produce long cycle life of lithium-sulfur battery,” *Nano Energy*, vol. 30, no. September, pp. 1–8, 2016, doi: 10.1016/j.nanoen.2016.09.030.

[284] S. A. Abbas *et al.*, “Bifunctional separator as a polysulfide mediator for highly stable Li-S batteries,” *J. Mater. Chem. A*, vol. 4, no. 24, pp. 9661–9669, 2016, doi: 10.1039/c6ta02272c.

[285] L. Yan *et al.*, “Enhanced performance of lithium-sulfur batteries with an ultrathin and lightweight MoS2/carbon nanotube interlayer,” *J. Power Sources*, vol. 389, no. December 2017, pp. 169–177, 2018, doi: 10.1016/j.jpowsour.2018.04.015.

[286] M. Li *et al.*, “Metal-Organic Framework-Based Separators for Enhancing Li-S Battery Stability: Mechanism of Mitigating Polysulfide Diffusion,” *ACS Energy Lett.*, vol. 2, no. 10, pp. 2362–2367, 2017, doi: 10.1021/acsenergylett.7b00692.

[287] S. Suriyakumar, A. M. Stephan, N. Angulakshmi, M. H. Hassan, and M. H. Alkordi, “Metal–organic framework@SiO_2 as permselective separator for lithium–sulfur batteries,” *J. Mater. Chem. A*, 2018, doi: 10.1039/C8TA02259C.

[288] X. Hong *et al.*, “Cerium based metal-organic frameworks as an efficient separator coating catalyzing the conversion of polysulfi des for high performance lithium-sulfur batteries,” *ACS Nano*, vol. 13, pp. 1923–1931, 2019, doi: 10.1021/acsnano.8b08155.

[289] Y. Zang, F. Pei, J. Huang, Z. Fu, G. Xu, and X. Fang, “Large-Area Preparation of Crack-Free Crystalline Microporous Conductive Membrane to Upgrade High Energy Lithium – Sulfur Batteries,” *Adv. Energy Mater.*, vol. 8, p. 1802052, 2018, doi: 10.1002/aenm.201802052.

[290] W. Kong *et al.*, “Ultrathin MnO2/Graphene Oxide/Carbon Nanotube Interlayer as Efficient Polysulfide-Trapping Shield for High-Performance Li–S Batteries,” *Adv. Funct. Mater.*, vol. 27, no. 18, 2017, doi: 10.1002/adfm.201606663.

[291] L. Wang, J. Liu, S. Haller, Y. Wang, and Y. Xia, “A scalable hybrid separator for a high performance lithium–sulfur battery,” *Chem. Commun.*, vol. 51, no. 32, pp. 6996–6999, 2015, doi: 10.1039/C5CC00444F.

[292] Z. Wang *et al.*, “Constructing metal-free and cost-effective multifunctional separator for high-performance lithium-sulfur batteries,” *Nano Energy*, vol. 59, pp. 390–398, 2019, doi: 10.1016/j.nanoen.2019.02.029.

[293] J.-Q. Huang, Q. Zhang, H.-J. Peng, X.-Y. Liu, W.-Z. Qian, and F. Wei, “Ionic shield for polysulfides towards highly-stable lithium–sulfur batteries,” *Energy Environ. Sci.*, vol. 7, no. 1, pp. 347–353, 2014, doi: 10.1039/C3EE42223B.

[294] T. Z. Zhuang *et al.*, “Rational Integration of Polypropylene/Graphene Oxide/Nafion as Ternary-Layered Separator to Retard the Shuttle of Polysulfides for Lithium-Sulfur Batteries,” *Small*, vol. 12, no. 3, pp. 381–389, 2016, doi: 10.1002/smll.201503133.

[295] C. Sun, Y. Song, Y. Yan, J. Yuan, Z. Huang, and L. Fang, “Integrating flexible PMIA separator and electrode for dealing with multi-aspect issues in Li-S batteries,” *Electrochim. Acta*, vol. 359, p. 136987, 2020, doi: 10.1016/j.electacta.2020.136987.

[296] N. Deng *et al.*, “Designing of a phosphorus, nitrogen, and sulfur three-flame retardant applied in a gel poly-m- phenyleneisophthalamide nanofiber membrane for advanced safety lithium- sulfur batteries,” *ACS Appl. Mater. interfaces*, vol. 11, pp. 36705–36716, 2019, doi: 10.1021/acsami.9b12395.

[297] Y. Wang, Z. Zhang, L. Dong, and Y. Jin, “Reduced shuttle effect by dual synergism of lithium – sulfur batteries with polydopamine-modified polyimide separators,” *J. Memb. Sci.*, vol. 595, p. 117581, 2020, doi: 10.1016/j.memsci.2019.117581.

[298] S. Song, L. Shi, S. Lu, and Y. Pang, “Author ’ s Accepted Manuscript A new polysulfide blocker - Poly (acrylic acid) modified separator for improved performance of lithium-sulfur battery,” *J. Memb. Sci.*, vol. 563, no. March, pp. 277–283, 2018, doi: 10.1016/j.memsci.2018.05.050.

[299] Y. Li *et al.*, “Glass fiber separator coated by porous carbon nanofiber derived from immiscible PAN/PMMA for high-performance lithium-sulfur batteries,” *J. Memb. Sci.*, vol. 552, no. February, pp. 31–42, 2018, doi: 10.1016/j.memsci.2018.01.062.

[300] G. Li *et al.*, “Polysulfide Regulation by the Zwitterionic Barrier toward Durable Lithium-Sulfur Batteries,” *JACS*, vol. 142, pp. 3583–3592, 2020, doi: 10.1021/jacs.9b13303.

[301] J. K. Huang *et al.*, “Functional Two-Dimensional Coordination Polymeric Layer as a Charge Barrier in Li-S Batteries,” *ACS Nano*, vol. 12, no. 1, pp. 836–843, 2018, doi: 10.1021/acsnano.7b08223.

[302] J. Wu, H. Zeng, X. Li, X. Xiang, Y. Liao, and Z. Xue, “Ultralight layer-by-layer self-assembled MoS2-polymer modified separator for simultaneously trapping polysulfides and suppressing lithium dendrites,” *Adv. Energy Mater.*, vol. 8, p. 1802430, 2018, doi: 10.1002/aenm.201802430.

[303] S. Li, J. He, and Y. Chen, “Vertical Co9S8 hollow nanowall arrays grown on a Celgard separator as a multifunctional polysulfide,” *Energy Environ. Sci.*, vol. 11, pp. 2560–2568, 2018, doi: 10.1039/c8ee00893k.

[304] Y. Zhang and H. Wu, “Interwoven V2O5 nanowire/graphene nanoscroll hybrid assembled as efficient polysulfide-trapping-conversion interlayer for long-life lithium–sulfur batteries,” *J. Mater. Chem. A*, vol. 6, pp. 19358–19370, 2018, doi: 10.1039/c8ta06610h.

[305] C. Song *et al.*, “3D catalytic MOF-based nanocomposite as separator coatings for high-performance Li-S battery,” *Chem. Eng. J.*, vol. 381, p. 122701, 2020, doi:

10.1016/j.cej.2019.122701.

[306] C. Fan *et al.*, “The effective design of a polysulfide-trapped separator at the molecular level for high energy density Li-S batteries,” *ACS Appl. Mater. Interfaces*, vol. 8, pp. 16108–16115, 2016, doi: 10.1021/acsami.6b04578.

[307] C. Zhou *et al.*, “A robust electrospun separator modi fi ed with in situ grown metal-organic frameworks for lithium-sulfur batteries,” *Chem. Eng. J.*, vol. 395, p. 124979, 2020, doi: 10.1016/j.cej.2020.124979.

[308] S. Lee and S. Lee, “Nanomat Li–S batteries based on all-fibrous cathode/separator assemblies and reinforced Li metal anodes: towards ultrahigh energy density and flexibility,” *Energy Environ. Sci.*, vol. 12, pp. 177–186, 2019, doi: 10.1039/c8ee01879k.

[309] J. Wang *et al.*, “Suppressing the shuttle effect and dendrite growth in lithium -sulfur batteries,” *ACS Nano*, vol. 14, pp. 9819–9831, 2020, doi: 10.1021/acsnano.0c02241.

[310] Y. He *et al.*, “Simultaneously inhibiting lithium dendrites growth and polysulfides shuttle by a flexible MOF-based membrane in Li-S Batteries,” *Adv. Energy Mater.*, vol. 8, p. 1802130, 2018, doi: 10.1002/aenm.201802130.

[311] Z. Zhou, T. Zhao, X. Lu, H. Cao, X. Zha, and Z. Zhou, “Functionalized polyimide separators enable high performance lithium sulfur batteries at elevated temperature,” *J. Power Sources*, vol. 396, no. March, pp. 542–550, 2018, doi: 10.1016/j.jpowsour.2018.06.040.

[312] H. Kim, J. T. Lee, and G. Yushin, “High temperature stabilization of lithium e sulfur cells with carbon nanotube current collector,” *J. Power Sources*, vol. 226, pp. 256–265, 2013, doi: 10.1016/j.jpowsour.2012.10.028.

[313] D. R. Deng *et al.*, “Enhanced adsorptions to polysulfides on graphene-supported BN nanosheets with excellent Li-S battery performance in a wide temperature range,” *ACS Nano*, vol. 12, pp. 11120–11129, 2018, doi: 10.1021/acsnano.8b05534.

[314] H. Yang *et al.*, “An intrinsic flame-retardant organic electrolyte for safe lithium-sulfur batteries,” *Angew. Chemie Int. Ed.*, vol. 131, pp. 801–805, 2019, doi: 10.1002/ange.201811291.

[315] J. Huang, X. Liu, and Q. Zhang, “Entrapment of sulfur in hierarchical porous graphene for lithium-sulfur batteries with high rate performance from -40 to 60C,” *Nano Energy*, vol. 2, no. 2, pp. 314–321, 2013, doi: 10.1016/j.nanoen.2012.10.003.

[316] X. Li *et al.*, “Safe and durable high-temperature lithium-sulfur batteries via molecular layer deposited coating,” *Nano Lett.*, vol. 16, pp. 3545–3549, 2016, doi: 10.1021/acs.nanolett.6b00577.

[317] T. Chen *et al.*, “Self-templated formation of interlaced carbon nanotubes threaded hollow Co3S4 nanoboxes for high-rate and heat-resistant lithium-sulfur batteries,” *JACS*, vol.

139, pp. 12710–12715, 2017, doi: 10.1021/jacs.7b06973.

[318] J. Wang, W. Qin, X. Zhu, and Y. Teng, “Covalent organic frameworks (COF)/CNT nanocomposite for high performance and wide operating temperature lithium-sulfur batteries,” *Energy*, p. doi.org/10.1016/j.energy.2020.117372, 2020, doi: 10.1016/j.energy.2020.117372.

[319] M. L. Gordin *et al.*, “Bis(2,2,2-trifluoroethyl) ether as an electrolyte co-solvent for mitigating self-discharge in lithium-sulfur batteries,” *ACS Appl. Mater. Interface*, vol. 6, pp. 8006–8010, 2014.

[320] M. Rolf, P. Adelhelm, H. Sommer, H. Schneider, K. Leitner, and J. Janek, “Systematical electrochemical study on the parasitic shuttle-effect in lithium-sulfur-cells at different temperatures and different rates,” *J. Power Sources*, vol. 259, pp. 289–299, 2014, doi: 10.1016/j.jpowsour.2014.02.075.

[321] Q. Pang, X. Liang, C. Y. Kwok, and L. F. Nazar, “Review—The Importance of Chemical Interactions between Sulfur Host Materials and Lithium Polysulfides for Advanced Lithium-Sulfur Batteries,” *J. Electrochem. Soc.*, vol. 162, no. 14, pp. A2567–A2576, 2015, doi: 10.1149/2.0171514jes.

[322] Z. Li *et al.*, “A highly ordered Meso@microporous carbon-supported Sulfur@smaller sulfur core-shell structured cathode for Li-s batteries,” *ACS Nano*, vol. 8, no. 9, pp. 9295–9303, 2014, doi: 10.1021/nn503220h.

[323] G. He, S. Evers, X. Liang, M. Cuisinier, A. Garsuch, and L. F. Nazar, “Tailoring porosity in carbon nanospheres for lithium-sulfur battery cathodes,” *ACS Nano*, vol. 7, no. 12, pp. 10920–10930, 2013, doi: 10.1021/nn404439r.

[324] F. Böttger-Hiller *et al.*, “Twin polymerization at spherical hard templates: An approach to size-adjustable carbon hollow spheres with micro- or mesoporous shells,” *Angew. Chemie - Int. Ed.*, vol. 52, no. 23, pp. 6088–6091, 2013, doi: 10.1002/anie.201209849.

[325] J. Schuster *et al.*, “Spherical ordered mesoporous carbon nanoparticles with high porosity for lithium-sulfur batteries,” *Angew. Chemie - Int. Ed.*, vol. 51, no. 15, pp. 3591–3595, 2012, doi: 10.1002/anie.201107817.

[326] N. Jayaprakash, J. Shen, S. S. Moganty, A. Corona, and L. A. Archer, “Porous hollow carbon@sulfur composites for high-power lithium-sulfur batteries,” *Angew. Chemie - Int. Ed.*, vol. 50, no. 26, pp. 5904–5908, 2011, doi: 10.1002/anie.201100637.

[327] L. Sun *et al.*, “Sulfur nanocrystals confined in carbon nanotube network as a binder-free electrode for high-performance lithium sulfur batteries,” *Nano Lett.*, vol. 14, no. 7, pp. 4044–4049, 2014, doi: 10.1021/nl501486n.

[328] G. Zheng, Y. Yang, J. J. Cha, S. S. Hong, and Y. Cui, “Hollow carbon nanofiber-encapsulated sulfur cathodes for high specific capacity rechargeable lithium batteries,” *Nano Lett.*, vol. 11, no. 10, pp. 4462–4467, 2011, doi: 10.1021/nl2027684.

[329] R. Elazari, G. Salitra, A. Garsuch, A. Panchenko, and D. Aurbach, “Sulfur-impregnated activated carbon fiber cloth as a binder-free cathode for rechargeable Li-S batteries,” *Adv. Mater.*, vol. 23, no. 47, pp. 5641–5644, 2011, doi: 10.1002/adma.201103274.

[330] S. Xin *et al.*, “Smaller sulfur molecules promise better lithium’sulfur batteries,” *J. Am. Chem. Soc.*, vol. 134, no. 45, pp. 18510–18513, 2012, doi: 10.1021/ja308170k.

[331] S. Evers and L. F. Nazar, “Graphene-enveloped sulfur in a one pot reaction: A cathode with good coulombic efficiency and high practical sulfur content,” *Chem. Commun.*, vol. 48, no. 9, pp. 1233–1235, 2012, doi: 10.1039/c2cc16726c.

[332] H. Wang *et al.*, “Graphene-wrapped sulfur particles as a rechargeable lithium-sulfur battery cathode material with high capacity and cycling stability,” *Nano Lett.*, vol. 11, no. 7, pp. 2644–2647, 2011, doi: 10.1021/nl200658a.

[333] Y. Yang *et al.*, “Improving the performance of lithium-sulfur batteries by conductive polymer coating,” *ACS Nano*, vol. 5, no. 11, pp. 9187–9193, 2011, doi: 10.1021/nn203436j.

[334] J. Xu, T. Lawson, H. Fan, D. Su, and G. Wang, “Updated Metal Compounds (MOFs, □S, □OH, □N, □C) Used as Cathode Materials for Lithium–Sulfur Batteries,” *Adv. Energy Mater.*, vol. 8, no. 10, pp. 1–23, 2018, doi: 10.1002/aenm.201702607.

[335] W. Hua *et al.*, “Polysulfide-Scission Reagents for the Suppression of the Shuttle Effect in Lithium-Sulfur Batteries,” *ACS Nano*, vol. 11, no. 2, pp. 2209–2218, 2017, doi: 10.1021/acsnano.6b08627.

[336] T. Zhao *et al.*, “Advanced Lithium–Sulfur Batteries Enabled by a Bio-Inspired Polysulfide Adsorptive Brush,” *Adv. Funct. Mater.*, vol. 26, no. 46, pp. 8418–8426, 2016, doi: 10.1002/adfm.201604069.

[337] T. Zhou *et al.*, “Twinborn TiO2-TiN heterostructures enabling smooth trapping-diffusion-conversion of polysulfides towards ultralong life lithium-sulfur batteries,” *Energy Environ. Sci.*, vol. 10, no. 7, pp. 1694–1703, 2017, doi: 10.1039/c7ee01430a.

[338] J. H. Kim *et al.*, “Polysulfide-Breathing/Dual-Conductive, Heterolayered Battery Separator Membranes Based on 0D/1D Mingled Nanomaterial Composite Mats,” *Nano Lett.*, vol. 17, no. 4, pp. 2220–2228, 2017, doi: 10.1021/acs.nanolett.6b04830.

[339] Z. W. Seh, Q. Zhang, W. Li, G. Zheng, H. Yao, and Y. Cui, “Stable cycling of lithium sulfide cathodes through strong affinity with a bifunctional binder,” *Chem. Sci.*, vol. 4, no. 9, pp. 3673–3677, 2013, doi: 10.1039/c3sc51476e.

[340] M. Liu, F. Ye, W. Li, H. Li, and Y. Zhang, “Chemical routes toward long-lasting lithium/sulfur cells,” *Nano Res.*, vol. 9, no. 1, pp. 94–116, 2016, doi: 10.1007/s12274-016-1027-8.

[341] Y. He, Z. Chang, S. Wu, and H. Zhou, “Effective strategies for long-cycle life lithium-

sulfur batteries," *J. Mater. Chem. A*, vol. 6, no. 15, pp. 6155–6182, 2018, doi: 10.1039/c8ta01115j.

[342] J. Q. Huang, Q. Zhang, H. J. Peng, X. Y. Liu, W. Z. Qian, and F. Wei, "Ionic shield for polysulfides towards highly-stable lithium-sulfur batteries," *Energy Environ. Sci.*, vol. 7, no. 1, pp. 347–353, 2014, doi: 10.1039/c3ee42223b.

[343] S. Bai, X. Liu, K. Zhu, S. Wu, and H. Zhou, "Metal-organic framework-based separator for lithium-sulfur batteries," *Nat. Energy*, vol. 1, no. 7, 2016, doi: 10.1038/nenergy.2016.94.

[344] J. Zhou *et al.*, "Rational design of a metal-organic framework host for sulfur storage in fast, long-cycle Li-S batteries," *Energy Environ. Sci.*, vol. 7, no. 8, pp. 2715–2724, 2014, doi: 10.1039/c4ee01382d.

[345] A. I. Gopalan *et al.*, "Development of electrospun PVdF-PAN membrane-based polymer electrolytes for lithium batteries," *J. Memb. Sci.*, vol. 325, no. 2, pp. 683–690, 2008, doi: 10.1016/j.memsci.2008.08.047.

[346] S. H. Kim, K. H. Choi, S. J. Cho, E. H. Kil, and S. Y. Lee, "Mechanically compliant and lithium dendrite growth-suppressing composite polymer electrolytes for flexible lithium-ion batteries," *J. Mater. Chem. A*, vol. 1, no. 16, pp. 4949–4955, 2013, doi: 10.1039/c3ta10612h.

[347] C. H. Tsao, Y. H. Hsiao, C. H. Hsu, and P. L. Kuo, "Stable Lithium Deposition Generated from Ceramic-Cross-Linked Gel Polymer Electrolytes for Lithium Anode," *ACS Appl. Mater. Interfaces*, vol. 8, no. 24, pp. 15216–15224, 2016, doi: 10.1021/acsami.6b02345.

[348] J. H. Miner, "The glomerular basement membrane," *Experimental Cell Research*, vol. 318, no. 9. Academic Press Inc., pp. 973–978, May 15, 2012, doi: 10.1016/j.yexcr.2012.02.031.

[349] L. Xu, X. Zhao, C. Xu, and N. A. Kotov, "Water-Rich Biomimetic Composites with Abiotic Self-Organizing Nanofiber Network," *Adv. Mater.*, vol. 30, no. 1, 2018, doi: 10.1002/adma.201703343.

[350] S. R. Pullela, C. Andres, W. Chen, C. Xu, L. Wang, and N. A. Kotov, "Permselectivity replication of artificial glomerular basement membranes in nanoporous collagen multilayers," *J. Phys. Chem. Lett.*, vol. 2, no. 16, pp. 2067–2072, 2011, doi: 10.1021/jz200880c.

[351] G. R. Bolton, W. M. Deen, and B. S. Daniels, "Assessment of the charge selectivity of glomerular basement membrane using Ficoll sulfate," *Am. J. Physiol. Physiol.*, vol. 274, no. 5, pp. F889–F896, 1998, doi: 10.1152/ajprenal.1998.274.5.F889.

[352] S. Ahmed *et al.*, "Enabling fast charging – A battery technology gap assessment," *J. Power Sources*, vol. 367, pp. 250–262, Nov. 2017, doi: 10.1016/j.jpowsour.2017.06.055.

[353] W. Chen *et al.*, “Designing Safe Electrolyte Systems for a High-Stability Lithium–Sulfur Battery,” *Advanced Energy Materials*. 2018, doi: 10.1002/aenm.201702348.